Reconstruction of High Energy Scattering Events in the HERMES Experiment

Ph.D. Thesis submitted to the Science Faculties of the
Friedrich–Alexander–Universität Erlangen–Nürnberg

by

Wolfgang Wander

Mannheim

Approved as Dissertation by the Science Faculties of the University of Erlangen-Nürnberg

Date of the Oral Exam:	30. April 1996
Chair of the Examining Committee:	Prof. Dr. D. Kölzow
First Referee:	Prof. Dr. K. Rith
Second Referee:	Prof. Dr. G. Anton

Translation from the German original by Marianne Averesch, M.A. and Ralf Kaiser, Ph.D., June 1997.

Contents

Chapter 1

Introduction

The spin of the nucleon is once again at the center of attention. After the discovery of quarks it was initially thought that the spin of baryons, in keeping with their SU(6) wave function, were composed in an additive fashion of spin-$\frac{1}{2}$ constituent quarks. However, since the measurements of the European Muon Collaboration (EMC) in 1987 [EMC89], whose results showed contributions of the quark spins to the nucleon spin to be compatible with zero, new explanations must be sought.

Quantum chromodynamics provides the following ansatz for the expectation value $\langle S_z \rangle_{\mathrm{Nucleon}}$ of the nucleon spin:

$$\langle S_z \rangle_{\mathrm{Nucleon}} = \frac{1}{2} = \frac{1}{2} \sum_f \Delta q_f + \Delta G + L_z \quad , \tag{1.1}$$

with $\frac{1}{2} \sum_f \Delta q_f$, the spin sum over all quarks, including valence and sea quarks, ΔG, the gluon spin contribution and L_z, the contributions from orbital angular momenta of the constituents of the nucleon.

QCD can also predict the contributions of each quark variety (Δu, Δd, Δs), more precisely, combinations of these (see chapter 2.3). However, these must still find experimental verification. First measurements at CERN and SLAC seem to validate the fundamental tenets of QCD, such as the Bjørken sum rule, in the measured kinematic region.

On the one hand, as a new experiment HERMES will verify these results. On the other hand, in using its orientation towards semi-inclusive measurements HERMES can determine the contributions in equation (1.1) in as yet unreached precision.

The expected large data volume, as well as its competition with the other experiments at CERN and SLAC, bring with it great expectations as to the functionality and speed of the analysis software. A significant and time critical aspect of the analysis is the reconstruction of the scattered particles in the HERMES detector. This will comprise the main emphasis of this thesis. In the appendix, the particulars of the data bank and process control module DAD may be found. The latter being used, among other things, for the detector control in the HERMES experiment.

Chapter 2

Aspects of HERMES Physics

2.1 Deep Inelastic Scattering

Contrary to elastic scattering, where the kinetic energy of the scattered particles is conserved, in inelastic scattering part of the initial energy is transferred to the production of new particles or the fission of the initial particles.

In the lowest order of QED the scattering process of positrons off nucleons can be pictured as in figure 2.1.

The kinematics are described by the four-momenta of the lepton $\boldsymbol{k}$ and $\boldsymbol{k'}$ before and after the scattering process. The four-momentum of the nucleon $\boldsymbol{P}$ is transformed into the total momentum of the fission products $\boldsymbol{P'}$ by the momentum transfer of the virtual photon $\boldsymbol{q} = \boldsymbol{k} - \boldsymbol{k'}$.

Several Lorentz-invariant quantities that will be used in the following can be defined from these parameters:

The negative square of the momentum transfer of the virtual photon $\boldsymbol{q}$ can be given in the laboratory frame as

$$Q^2 = -\boldsymbol{q}^2 = -(\boldsymbol{k} - \boldsymbol{k'})^2 \stackrel{\text{lab}}{=} 4EE' \sin^2 \frac{\theta}{2} \tag{2.1}$$

where E and E' are the lepton energy before and after the scattering and θ is the scattering angle in the laboratory system (see fig. 2.2).

The energy loss of the scattered lepton in the laboratory frame can be expressed through the momenta $\boldsymbol{P}$ and $\boldsymbol{q}$ and the mass of the nucleon M:

$$\nu = \frac{\boldsymbol{P} \cdot \boldsymbol{q}}{M} \stackrel{\text{lab}}{=} E - E'. \tag{2.2}$$

The center of mass energy s is defined as

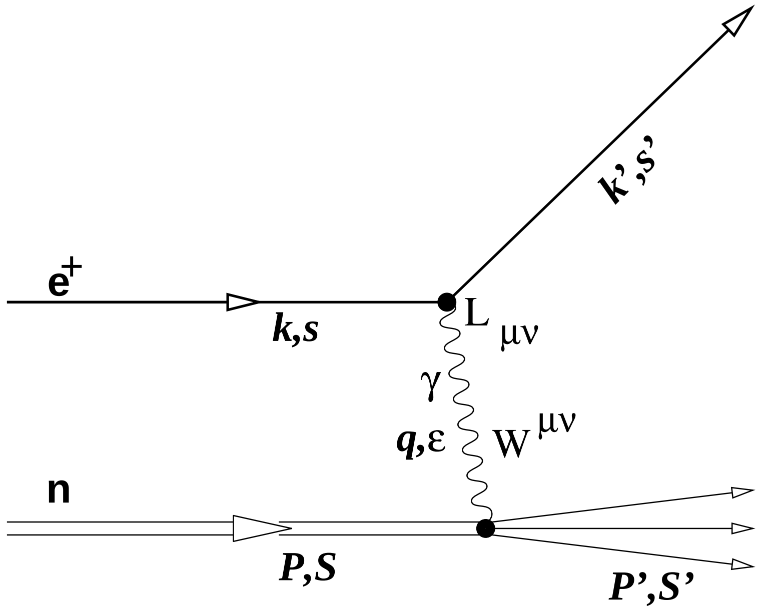

Figure 2.1: Deep inelastic scattering of a positron off a nucleon by exchange of a single photon. The positron transfers part of its momentum to the nucleon through the virtual photon. A constituent of the nucleon is knocked out and fragments into new particles.

$$s^2 = (\boldsymbol{k} + \boldsymbol{P})^2 \tag{2.3}$$

and the invariant mass W is

$$W^2 = \boldsymbol{P'}^2 \stackrel{\text{lab}}{=} M^2 + 2M\nu - Q^2, \tag{2.4}$$

where the lepton rest mass m is neglected.

The following scaling variables are used to describe the kinematic:

A measure of the inelasticity of the process is given by

$$x_{\text{bj}} = \frac{Q^2}{2\boldsymbol{Pq}} \stackrel{\text{lab}}{=} \frac{Q^2}{2M\nu} \tag{2.5}$$

which lies in the interval $0 < x_{\text{bj}} < 1$. A scattering process with $x_{\text{bj}} = 1$ corresponds to elastic scattering: The invariant mass of the scattering process is identical to the nucleon mass and from (2.4) follows $x_{\text{bj}} = 1$.

The energy transfer from the lepton to the nucleon in the laboratory frame can be expressed in a Lorentz-invariant way as

$$y = \frac{\boldsymbol{P}\cdot\boldsymbol{q}}{\boldsymbol{P}\cdot\boldsymbol{k}} \overset{\text{lab}}{=} \frac{\nu}{E}. \tag{2.6}$$

The scattering on polarized targets is described by the angles α, ϕ and the scattering angle θ. α is here the polarization angle of the target relative to the longitudinally polarized positron beam. The angle ϕ is the inclination of the scattering plane defined by the vectors $\boldsymbol{k}$ and $\boldsymbol{k'}$ relative to the polarization plane defined by the beam direction and the target polarization. The direction of the beam polarization is chosen to be parallel or anti-parallel to the beam direction, because the transverse polarization component in the cross section is kinematically suppressed (see (2.11)).

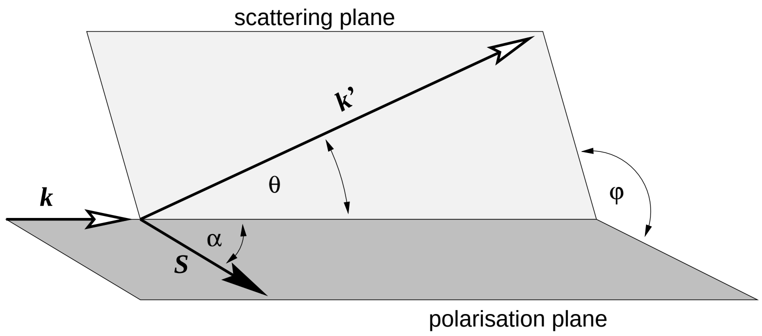

Figure 2.2: Definitions of the angles in polarized scattering. The angle α determines the direction of the polarization in respect to the longitudinally polarized positron beam. θ is the scattering angle and ϕ is the inclination of the scattering plane relative to the polarization plane.

2.2 The Cross Section

The single photon exchange cross section can be expressed as product of a leptonic tensor $L_{\mu\nu}$ and a hadronic tensor $W_{\mu\nu}$[ANS95]:

$$\frac{d^2\sigma}{d\Omega dE'} = \frac{\alpha^2}{2M\boldsymbol{q}^4}\frac{E'}{E}L_{\mu\nu}W^{\mu\nu}. \tag{2.7}$$

$\alpha \approx \frac{1}{137}$ is the fine structure constant in QED. Here the summation over the indices is assumed.

The leptonic tensor can be calculated from the Feynman-rules of quantum electrodynamics for the lepton-lepton scattering diagram with a single photon propagator,

$$L_{\mu\nu}(\boldsymbol{k},\boldsymbol{s};\boldsymbol{k'},\boldsymbol{s'}) = \left[\bar{u}(\boldsymbol{k'},\boldsymbol{s'})\gamma_\mu u(\boldsymbol{k},\boldsymbol{s})\right]^* \left[\bar{u}(\boldsymbol{k'},\boldsymbol{s'})\gamma_\nu u(\boldsymbol{k},\boldsymbol{s})\right], \tag{2.8}$$

where $\boldsymbol{s}$ and $\boldsymbol{s'}$ are the covariant spin four-vectors. For the calculation of the contribution of $L_{\mu\nu}$ to the polarized and unpolarized cross section the tensor is decomposed into symmetric (S) and antisymmetric (A) parts:

$$\begin{aligned} L_{\mu\nu}(\boldsymbol{k},\boldsymbol{s};\boldsymbol{k'},\boldsymbol{s'}) &= L^{(S)}_{\mu\nu}(\boldsymbol{k};\boldsymbol{k'}) + iL^{(A)}_{\mu\nu}(\boldsymbol{k},\boldsymbol{s};\boldsymbol{k'}) \\ &+ L'^{(S)}_{\mu\nu}(\boldsymbol{k},\boldsymbol{s};\boldsymbol{k'},\boldsymbol{s'}) + iL'^{(A)}_{\mu\nu}(\boldsymbol{k};\boldsymbol{k},\boldsymbol{s'}). \end{aligned} \tag{2.9}$$

with the components

$$L^{(S)}_{\mu\nu}(\boldsymbol{k};\boldsymbol{k'}) = k_\mu k'_\nu + k'_\mu k_\nu - g_{\mu\nu}(\boldsymbol{k}\cdot\boldsymbol{k'} - m^2), \tag{2.10}$$
$$L^{(A)}_{\mu\nu}(\boldsymbol{k},\boldsymbol{s};\boldsymbol{k'}) = m\epsilon_{\mu\nu\alpha\beta}s^\alpha(\boldsymbol{k}-\boldsymbol{k'})^\beta. \tag{2.11}$$

$L'^{(S)}$ and $L'^{(A)}$ vanish in the summation over the final spin states $\boldsymbol{s'}$ to obtain the polarized part of the lepton tensor. Additionally, the unknown initial states $\boldsymbol{s}$ are averaged for the unpolarized part. As a result $L^{(A)}$ is eliminated as well:

$$L^{(\mathrm{unp})}_{\mu\nu}(\boldsymbol{k};\boldsymbol{k'}) = 2L^{(S)}_{\mu\nu}(\boldsymbol{k};\boldsymbol{k'}) \tag{2.12}$$
$$L^{(\mathrm{pol})}_{\mu\nu}(\boldsymbol{k},\boldsymbol{s};\boldsymbol{k'}) = 2L^{(S)}_{\mu\nu}(\boldsymbol{k};\boldsymbol{k'}) + 2iL^{(A)}_{\mu\nu}(\boldsymbol{k},\boldsymbol{s};\boldsymbol{k'})e. \tag{2.13}$$

Initial and final state for the hadronic tensor can only be described by quantum chromodynamics and cannot be calculated rigorously. However, by demanding gauge invariance and parity conservation the most simple general form of $W_{\mu\nu}$ can be expressed as:

$$W_{\mu\nu}(\boldsymbol{q};\boldsymbol{P},\boldsymbol{S}) = W^{(S)}_{\mu\nu}(\boldsymbol{q};\boldsymbol{P}) + iW^{(A)}_{\mu\nu}(\boldsymbol{q};\boldsymbol{P},\boldsymbol{S}), \tag{2.14}$$

where the symmetric and the antisymmetric parts are described by the structure functions $W_{1/2}$ and $G_{1/2}$:

$$\begin{aligned} \frac{1}{2M}W^{(S)}_{\mu\nu}(\boldsymbol{q};\boldsymbol{P}) &= \left(-g_{\mu\nu} + \frac{q_\mu q_\nu}{\boldsymbol{q}^2}\right) W_1(\boldsymbol{q}^2,\boldsymbol{P}\cdot\boldsymbol{q}) \\ &+ \left[\left(P_\mu - \frac{\boldsymbol{P}\cdot\boldsymbol{q}}{\boldsymbol{q}^2}q_\mu\right)\left(P_\nu - \frac{\boldsymbol{P}\cdot\boldsymbol{q}}{\boldsymbol{q}^2}q_\nu\right)\right]\frac{W_2(\boldsymbol{q}^2,\boldsymbol{P}\cdot\boldsymbol{q})}{M^2} \end{aligned} \tag{2.15}$$

$$\begin{aligned} \frac{1}{2M}W^{(A)}_{\mu\nu}(\boldsymbol{q};\boldsymbol{P},\boldsymbol{S}) &= \epsilon_{\mu\nu\alpha\beta}q^\alpha\left\{MS^\beta G_1(\boldsymbol{q}^2,\boldsymbol{P}\cdot\boldsymbol{q})\right. \\ &+ \left.\left[(\boldsymbol{P}\cdot\boldsymbol{q})S^\beta - (\boldsymbol{S}\cdot\boldsymbol{q})P^\beta\right]\frac{G_2(\boldsymbol{q}^2,\boldsymbol{P}\cdot\boldsymbol{q})}{M}\right\}. \end{aligned} \tag{2.16}$$

Frequently the structure functions are given as functions of (Q^2,ν) instead of $(\boldsymbol{q}^2,\boldsymbol{P}\cdot\boldsymbol{q})$.

The total unpolarized cross section can be expressed as

$$\frac{d^2\sigma^{(\mathrm{unp})}}{d\Omega dE'}(\boldsymbol{k},\boldsymbol{P};\boldsymbol{k'}) = \frac{\alpha^2}{M\boldsymbol{q}^4}\frac{E'}{E}L^{(S)}_{\mu\nu}W^{\mu\nu(S)} \tag{2.17}$$

while the cross section difference for two opposite target states is given as:

$$\left(\frac{d^2\sigma}{d\Omega dE'}(\boldsymbol{k},\boldsymbol{P},-\boldsymbol{S};\boldsymbol{k'}) - \frac{d^2\sigma}{d\Omega dE'}(\boldsymbol{k},\boldsymbol{P},\boldsymbol{S};\boldsymbol{k'})\right) = \tag{2.18}$$
$$\frac{d^2\sigma^{\boldsymbol{S}}}{d\Omega dE'} - \frac{d^2\sigma^{-\boldsymbol{S}}}{d\Omega dE'} = \frac{2\alpha^2}{M\boldsymbol{q}^4}\frac{E'}{E}L^{(A)}_{\mu\nu}W^{\mu\nu(A)}.$$

The Bjørken limit describes the transition to large Q^2 and ν for fixed x_{bj}:

$$\lim_{\mathrm{bj}} Q^2 \to \infty \quad \lim_{\mathrm{bj}} \nu \to \infty \quad \lim_{\mathrm{bj}} x \quad \mathrm{fest.} \tag{2.19}$$

The unpolarized structure functions F_1 and F_2 are obtained in the Bjørken limit as

$$\lim_{\mathrm{bj}} MW_1(Q^2,\nu) = F_1(x,Q^2) \tag{2.20}$$
$$\lim_{\mathrm{bj}} \nu W_2(Q^2,\nu) = F_2(x,Q^2). \tag{2.21}$$

F_1 and F_2 are practically scale invariant, that is independent of Q^2, indicating that the scattering occurs on point like constituents.

In the parton model the nucleon is considered in a fast moving reference frame to neglect the transverse momentum and the finite mass of the constituents. $F_2(x)$ can then be described as the weighted sum of the constituent momentum distributions. In this model x corresponds for large momentum transfers to the Nachtmann-variable ξ, which is the momentum fraction of the scattered constituent[POV94]. F_2 is then composed from the momentum distributions $q_f(x)$ by summing over all constituents weighted with the square of their electric charge e_{q_f}. The sum itself is weighted by x:

$$F_2(x) = x\sum_f e^2_{q_f} q_f(x). \tag{2.22}$$

For F_1, which is defined by the magnetic interactions with the constituents, and the Callan-Gross relation for spin 1/2 constituents

$$2xF_1(x) = F_2(x) \tag{2.23}$$

in the parton model follows from (2.22):

$$F_1(x) = \frac{1}{2}\sum_f e_{q_f}^2 q_f(x). \tag{2.24}$$

The small deviation from (2.23) that is in fact observed can be explained as an effect of the neglected quark mass and transverse momentum. It is described by the function $R(x, Q^2)$:

$$2xF_1(x, Q^2) = \frac{(1+\gamma^2)F_2(x, Q^2)}{1 + R(x, Q^2)}, \tag{2.25}$$

with $\gamma^2 = \frac{Q^2}{\nu^2} = 4\frac{M^2x^2}{Q^2}$.

For the asymmetric part of the hadronic tensor (2.16) scale invariant structure functions g_1 and g_2 can be defined that are analogous to (2.20-2.21):

$$\lim_{\mathrm{bj}} M^2\nu G_1(Q^2, \nu) = g_1(x, Q^2), \tag{2.26}$$

$$\lim_{\mathrm{bj}} M\nu^2 G_2(Q^2, \nu) = g_2(x, Q^2). \tag{2.27}$$

In the parton model these structure functions are composed from the quark distributions:

$$g_1(x) = \frac{1}{2}\sum_{q_f} e_{q_f}^2 (\overset{\rightrightarrows}{q}_f(x) - \overset{\rightleftarrows}{q}_f(x)), \tag{2.28}$$

$$g_2(x) = 0. \tag{2.29}$$

Here $\overset{\rightleftarrows}{q}_f(x)$ and $\overset{\rightrightarrows}{q}_f(x)$ are the probabilities to find a particular quark type q_f with spin anti-parallel or parallel to the nucleon polarization.

In analogy to F_1, g_1 describes the difference in the spin states of the quark momentum distributions. In this model g_2 vanishes.

However, non-zero values of g_2 are predicted from different models of quark-gluon interactions.

For a longitudinally polarized beam a relation for the extraction of the structure functions from the data may be derived as a function of the angles ϕ and α:

$$\frac{d^2\sigma(\alpha) - d^2\sigma(\pi + \alpha)}{dx\,dy\,d\phi} = \tag{2.30}$$

$$\frac{e^4}{4\pi^2 Q^2}\left\{\cos\alpha\left[\left(\frac{4-2y-y^2\gamma^2}{4}\right)g_1(x,Q^2)-\frac{y}{2}\gamma^2 g_2(x,Q^2)\right]\right.$$
$$\left.-\sin\alpha\cos\phi\sqrt{\gamma^2\left(\frac{4-4y-y^2\gamma^2}{4}\right)}\left(\frac{y}{2}g_1(x,Q^2)+g_2(x,Q^2)\right)\right\}.$$

2.3 Sum Rules

In a theoretical description of quantum chromodynamics (QCD) it is often not possible to give exact descriptions of the x-dependence of structure functions in a given model, whereas predictions for the moments of these functions ($M_n(f) = \int dx\, x^{(n-1)} f(x)$) can be given. These predictions can be compared to experimental results to verify a model.

2.3.1 The Bjørken Sum Rule

The Bjørken sum rule[BJØ66] for the first moment of the difference of g_1 for proton and neutron was derived from the basic principles of SU(6) current algebra and belongs to the fundamental predictions of QCD:

$$\int_0^1 dx\,(g_1^p(x) - g_1^n(x)) = \frac{1}{6}\left|\frac{g_A}{g_V}\right| + \text{QCD-Corrections} = 0.191 \pm 0.002, \quad (2.31)$$

at $Q^2 = 10$ GeV for 1st order corrections in α_s, where g_A/g_V is the ratio of axial and vector coupling constants in neutron β-decay.

A violation of the Bjørken sum rule would question the validity of QCD on a fundamental level. However, so far the measurements at SLAC and CERN have confirmed this sum rule[SLA95a, SMC94a, SMC94b, SMC93, MEZ94]..

2.3.2 The Ellis-Jaffe Sum Rule

This sum rule is based on the assumption that the s quarks, which occur only in the quark-antiquark sea of the nucleon, do not contribute to the spin of the nucleon. In this case the value of the first moment of g_1 to the first order in α_s would be

$$\int_0^1 dx\, g_1^p(x) = \frac{1}{18}(9F - D) = 0.185, \quad (2.32)$$
$$\int_0^1 dx\, g_1^n(x) = \frac{1}{18}(6F - 4D) = -0.024. \quad (2.33)$$

at $Q^2 = 10$ GeV. F, D are the baryon decay constants.

In 1987 a measurement by the EMC[EMC89] produced

$$\int_0^1 dx\, g_1^p(x) = (0.126 \pm 0.010 \pm 0.015)_{\mathrm{EMC/SLAC}}, \tag{2.34}$$

at $\langle Q^2 \rangle = 10$ GeV. This measurement disagreed with the theoretical value including QCD corrections of 0.189, resulting in the so called `spin crisis', which also lead to the conception of the HERMES experiment.

New data from SLAC[SLA93, SLA95a] and CERN[SMC93, SMC94b, SMC94a] confirm the EMC measurement for the proton particularly if higher QCD corrections are included[LAR94].

2.4 The Extraction of g_1 from the Data

For the measurement of g_1 a target is employed whose polarization is parallel or antiparallel to the beam direction. By comparing the cross sections

$$A_{||} = \frac{\sigma^{\rightleftarrows} - \sigma^{\rightrightarrows}}{\sigma^{\rightleftarrows} + \sigma^{\rightrightarrows}} \tag{2.35}$$

the asymmetry $A_{||}$ is obtained. An additional measurement with a target polarization transverse to the electron beam yields $A_{\perp}$:

$$A_{\perp} = \frac{\sigma^{\rightarrow\Uparrow} - \sigma^{\rightarrow\Downarrow}}{\sigma^{\rightarrow\Uparrow} + \sigma^{\rightarrow\Downarrow}}. \tag{2.36}$$

Both asymmetries are determined for a given target and beam polarization, where the beam polarization is not identical to the polarization of the virtual photon that finally interacts with the polarized quark. To determine $g_{1/2}$, the measured asymmetries $A_{||/\perp}$ have to be transformed into the asymmetries $A_{1/2}$ that relate to the photon polarization[ANS95]:

$$A_{||} = D(A_1 + \eta A_2), \tag{2.37}$$
$$A_{\perp} = d(A_2 - \xi A_1), \tag{2.38}$$

with

$$A_1 = \frac{g_1 - \gamma^2 g_2}{F_1}, \tag{2.39}$$
$$A_2 = \gamma \frac{g_1 + g_2}{F_1}. \tag{2.40}$$

The kinematic factors D, d, η and ξ are defined as

$$
\begin{aligned}
D &= \frac{y(2-y)}{y^2+2(1-y)(1+R)}, &(2.41)\\
\eta &= \frac{2\gamma(1-y)}{2-y}, &(2.42)\\
d &= D\sqrt{\frac{2\epsilon}{1+\epsilon}}, &(2.43)\\
\xi &= \eta\frac{1+\epsilon}{2\epsilon}, &(2.44)\\
\epsilon &= \frac{1-y}{1-y+\frac{1}{2}y^2} &(2.45)
\end{aligned}
$$

Two approximations lead to the determination of g_1. First, g_2 is small[SLA95b] and suppressed in equation (2.39) by a factor of γ^2, so that this equation may be approximated as

$$g_1 \approx A_1 F_1 \overset{(2.25)}{=} A_1 F_2 \frac{1+\gamma^2}{2x(1+R)} \qquad (2.46)$$

Second, $A_2 \leq \sqrt{R}$ is an upper limit for A_2 in equation (2.37) [SMC94c], so that in this case ηA_2 may be neglected and g_1 can be determined from $A_{||}$ using the approximation

$$g_1 \approx \frac{A_{||}}{D} F_2 \frac{1+\gamma^2}{2x(1+R)} \qquad (2.47)$$

2.5 The Extraction of A_1^{He} and A_1^n

To extract the virtual photon asymmetries from the measured cross sections the depolarisation factor D of the virtual photon and further attenuation factors have to be taken into account. In the following chapters this will be illustrated for the case of the ^{3}He measurement. From the incomplete beam and target polarization arises a multiplicative attenuation factor $f_d = P_b \cdot P_t$.

According to (2.47) and the relation $dN = \sigma \mathcal{L} dt$ the following numbers of events are expected[FER95I]:

$$N^{\rightleftarrows} = \sigma^{(unp)} \left(\int_{\rightleftarrows} \mathcal{L}(t)dt + A_1^{^3\mathrm{He}} \int_{\rightleftarrows} \mathcal{L}(t) D f_d(t) dt \right), \qquad (2.48)$$

$$N^{\rightrightarrows} = \sigma^{(unp)} \left(\int_{\rightrightarrows} \mathcal{L}(t)dt - A_1^{^3\mathrm{He}} \int_{\rightrightarrows} \mathcal{L}(t) D f_d(t) dt \right), \tag{2.49}$$

where $\int_{\rightleftarrows} \mathcal{L}dt$ is the integrated luminosity for the antiparallel spin state. For $A_1^{^3\mathrm{He}}$ directly follows

$$A_1^{^3\mathrm{He}} = \frac{N^{\rightleftarrows} \int_{\rightrightarrows} \mathcal{L}dt - N^{\rightrightarrows} \int_{\rightleftarrows} \mathcal{L}dt}{N^{\rightleftarrows} \int_{\rightrightarrows} \mathcal{L}Df_d dt + N^{\rightrightarrows} \int_{\rightleftarrows} \mathcal{L}Df_d dt}. \tag{2.50}$$

This still leaves the the calculation of the neutron asymmetry from the helium asymmetry. The ^{3}He is almost exclusively in an S-state where both proton spins have opposite orientation. Therefore they add an unpolarized contribution that would attenuate the asymmetry by a factor of 1/3. On second view the unpolarized cross sections for neutron and proton have to be taken into account as well as the deviations from the ideal S-state: According to [CIO93] the nucleon polarization in the helium nucleus is expressed as

$$P_n^{^3\mathrm{He}} = 0.86 \pm 0.02 \quad P_p^{^3\mathrm{He}} = 0.028 \pm 0.003 \tag{2.51}$$

Using this information A_1^n can be calculated from $A_1^{^3\mathrm{He}}$ following

$$A_1^n = \frac{A_1^{^3\mathrm{He}} - 2\frac{F_2^p}{2F_2^p + F_2^n} P_p^{^3\mathrm{He}} A_1^p}{\frac{F_2^n}{2F_2^p + F_2^n} P_n^{^3\mathrm{He}}}, \tag{2.52}$$

using the known functions $F_2^{p/n}$ and A_1^p.

2.6 Further Measurements

From the measurement of $A_\perp$, with transverse target polarization, the theoretically interesting structure function g_2 can be determined using equations (2.38) and (2.40). This automatically allows a better determination of g_1, because the approximation of A_2 according to (2.47) becomes unnecessary.

For a target with spin 1, as in the case of a tensor-polarized deuteron target, two additional polarized structure functions can be measured. These are $b_1(x)$, with a longitudinally polarized target, and $\Delta(x)$ with a transverse target polarization. Both multipole structure functions are expected to be small [HOO89, JAF89a, JAF89b], where a non-zero value of b_1 might result from the influence of nuclear binding effects on the quark distributions. A finite Δ would indicate the existence of gluons that do not belong to a single nucleon in the deuteron.

Due to the good particle identification of the HERMES detector a multitude of semi-inclusive measurements and analyses are possible. These allow insights into the spin contributions from valence quarks, sea quarks and gluons. For example, a measurement of the pion charge asymmetry for two different targets and target polarizations directly allows the determination of the spin contributions from u and d valence quarks. Spin asymmetries in the kaon distributions (K^-) from a proton target probe the s-quark contribution to the sea quark spin distribution. The polarization of Λ and $\bar{\Lambda}$ hyperons may be determined from their decay products. This allows conclusions about the s-quark spin contribution as well. Polarized J/Ψ production can be detected through the decay into a e^+/e^- or μ^+/μ^- pair and contains information about the gluon spin contribution in the nucleon.

Measurements with transversely polarized target (relative to the beam direction) additionally allow a measurement of the angular momentum contribution to the spin. Several measurements should be carried out with spin alignment not parallel to the accelerator plane in order to detect a possible ϕ dependence.

Chapter 3

The Hermes Spectrometer

For HERMES to conduct experiments the detector needs to be constructed with a view to several considerations. The detector has to determine scattered particles, particularly positrons, in the whole kinematic region as well as a large portion of the hadronic final state, with good particle identification as well as momentum resolution. A spectrometer magnet with a field integral of 1.3 Tm is key in determining the momentum. The magnet is preceded and followed by tracking chambers which can determine the scattering and deflection angle with a high degree of accuracy. With a vertical acceptance of 40 — 140 mrad and a horizontal acceptance of ± 170 in front of the magnet and ± 278 mrad behind the magnet, particles can be detected over the whole acceptance down to 2 GeV. Below 2 GeV not all particles show up due to the pronounced bending of the track caused by the magnetic field. The Cerenkov counter for the separation of pions and heavier hadrons, and the electron-pion separators, preshower, calorimeter and transition radiation detector lead to a high efficiency and low contamination in the particle identification.

The target should allow high luminosity as well as high polarization with only small contamination through unpolarized target components. In this instance, the newly developed polarized internal gas target was successfully used.

A luminosity monitor, whose function is based on the detection of Bhabha scattered electron-positron pairs, provides both relative luminosity values for the measurement of polarization asymmetries as well as absolute values for the possible measurement of absolute structure functions.

The HERMES detector was installed at the HERA storage ring for electrons and positrons, in which transverse beam polarizations of up to 70% have been achieved [DUE95, OEL95]. The longitudinal polarization required for the polarized physics of the HERMES experiment is made possible through spin rotators both in front and behind the detector.

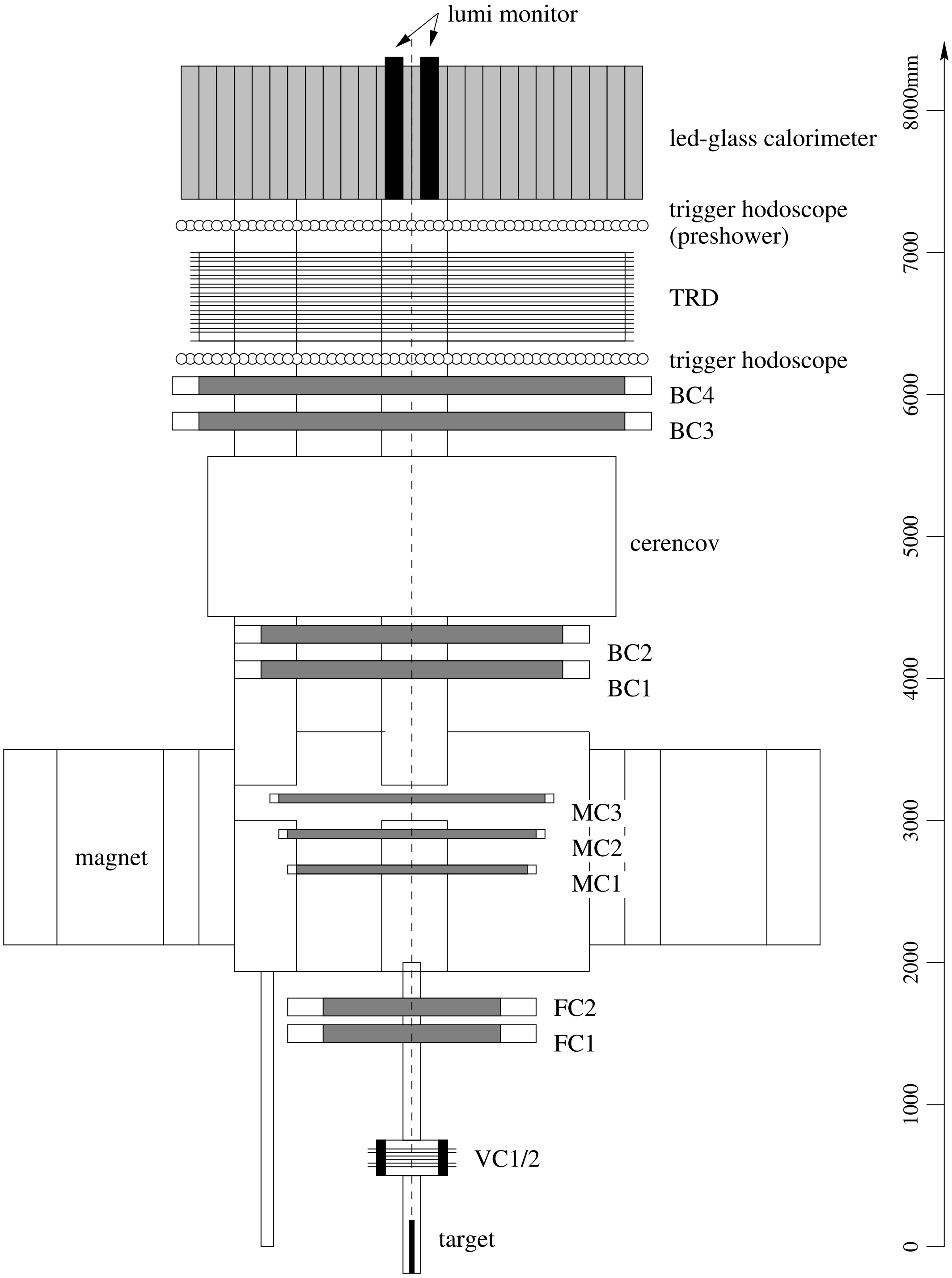

Figure 3.1: Schematic overview of the Hermes spectrometer. The tracking chambers in front of the magnet serve to determine the scattering angle and together with the chambers behind the magnet determine the momentum. The particle identification is undertaken with the Cerenkov counter, the preshower and the calorimeter solely in the latter part of the detector.

3.1 The Target

3.1.1 The Storage Cell Target

HERMES utilizes a recently developed technology - the gas target. Since the density of gas targets is constricted by the capacity of the atomic beam source, it is desirable to conserve produced atoms as long as possible in the beam of the storage ring. This is achieved through the use of a storage cell. This cell is a thin, T-shaped metal tube around the beam axis, which contains the injected target atoms until, after several hundred wall interactions, they drift into the ring towards the vacuum pumps (see figure 3.2). In using this technique the areal density of target atoms is increased multi-fold.

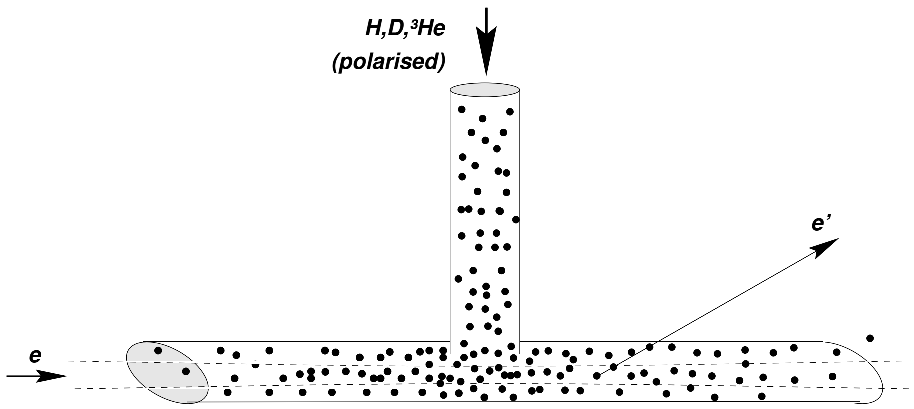

Figure 3.2: Overview of the internal gas target. The electron beam crosses the target cell, in which the target atoms are increased in density.

The HERMES target cell is an elliptical aluminum tube with the measures of $10 \times 30 \times 400$ mm^3 and a wall thickness of less than 0.1 mm. A smooth and thin wall reduces multiple scattering of particles at the cell atoms.

Polarized gas atoms (hydrogen, deuterium or ^{3}Helium) are produced by a source and injected into the cell. They are protected from the depolarizing effects of electron bunch induced high frequency fields by the use of external magnetic holding fields. A dry-film surface treatment[STE95] was used, whose molecules arrange surface hydrogen atoms, and thereby reduce the depolarizing spin exchange interactions of gas atoms with the target wall.

In order to increase the target density, the average atom velocity is reduced by cooling the cell. In the case of ^{3}He it is cooled to 20 K and 100 K for hydrogen and deuterium. In the latter case depolarization effects rise again with lower temperatures[KOR95].

Within short time periods the direction of polarization is changed so as to minimize the systematic errors potentially caused through deviations in detector stability.

3.1.2 The polarized ^{3}He Source

The helium source[LEE93] is capable of delivering high intensities ($2 \cdot 10^{17} \frac{\text{atoms}}{s}$) of polarized ^{3}He atoms. Within a pumping cell, electrical discharges cause a small fraction of atoms to be converted to a metastable state (2^3S_1). A 2^3P_0 can be reached by pumping these atoms with circularly polarized light. Through the emission of a photon the 2^3P_0 reverts into a 2^3S_1 state, which is now polarized due to angular momentum conservation. Polarization can be transferred to the ground state atoms through metastability exchange collisions with the gas.

Currently, polarization values of 50% to 60% have been achieved and is determined by two methods. In one method, the polarization of the gases in the pumping cell can be determined by looking at the relationship between intensities of left and right circularly polarized light. This light is emitted in the decay of $2^3P_0 \longrightarrow 2^3S_1 + \gamma$. In the second measurement, the TOM (target optical monitor) measures the polarization of the light emitted from outer electrons of the helium atoms which are excited by the Coulomb interaction with the electron beam. This polarization can be used to calculate the target polarization.

3.1.3 The Atomic Beam Source for Polarized H and D

The atomic beam source[STO94] is based on the Stern-Gerlach separation of dissociated hydrogen of deuterium beams, where atoms are separated by the spin of their electron. Through several high frequency transitions the electron spin is transferred to the spin of the nucleons. In this way an intensity flux of up to $6 \cdot 10^{16} \frac{\text{atoms}}{s}$ may be achieved with more than 90% polarization.

With the aid of the Breit-Rabi polarimeter[GAU91, BRA95a], which is connected to the storage cell by a tube, the polarization of the target atoms in the target may be measured. The degree of polarization may be determined with a relative uncertainty of 3%.

3.2 The Tracking Chambers

The tracking chambers determine the position of detected charged particles and thereby the kinematics of the events. Their resolution and efficiency also determine the resolution and efficiency of the detector. HERMES has placed a great value on exact angular resolution in the front region of the detector, so as to enable good vertex separation for semi-inclusive physics. To this end high resolution micro-strip gas chambers[BLO95] were installed with a resolution of up to 45 $\mu\mathrm{m}$. The front drift chambers are also notable for their small cell size and good position resolution. The back region of the detector is completely covered by drift chambers with a position resolution of 200 $\mu\mathrm{m}$. As a result of the large number of drift chambers installed an extremely accurate angle determination of the back part of the tracks is possible. An overview of the chamber properties may be seen in table 3.1.

	Vertex		Front		Magnet			Back	
Detector Name	VC-1	VC-2	FC-1	FC-2	MC-1	MC-2	MC-3	BC1/2	BC3/4
Dist. to Target (mm)	727	972	1526	1637	2655	3060	3423	4150	5900
Active hor. (mm)	420	420	680	680	996	1216	1424	1888	2890
Active vert. (mm)	137	145	220	220	263	306	347	520	710
Type	Microstrip Gas		Hor. Drift		Proportional			Hor. Drift	
Cell Size	193 μm		7 mm		2 mm			15 mm	
Nominal Resolution	45 – 56 μm		150 μm		460 – 570 μm			150 μm	
Number of Planes	3	3	6	6	3	3	3	6+6	6+6
Number of Wires (X)	1674	2046	96	96	496	608	720	120	192
Number of Wires (U/V)	2170	2170	96	96	512	608	720	118	186
Readout	digital (APC)		TDC		digital (PCOS)			TDC	
Radiation Length	1.2%		0.20%		0.29%			0.26%	

Table 3.1: Tracking Chamber Properties.

All chambers consist of single detectors which allow position determination in one of the coordinates x, u or v. The right handed HERMES coordinate system is oriented with its z-axis pointing in the beam direction, the y-coordinate points up, while x accordingly points in beam direction to the left. The x-wires are vertically arranged, while u and v wires are set at either 30° or -30° inclination (fig. 3.3).

The consistency in arranging wires in all detectors enables the use of the treesearch algorithm for pattern recognition in the projections (see chapter 4.2).

3.2.1 The Vertex Chambers

The vertex chambers each consist of two detector modules, each with a chamber in the x, u and v orientation. The individual chambers consist of the following (in beam direction): a cathode layer vapor deposited onto 200 $\mu\mathrm{m}$ thick glass, a 3 mm thick gas layer, acting as ionization material and anode strips, 7 $\mu\mathrm{m}$ wide and made

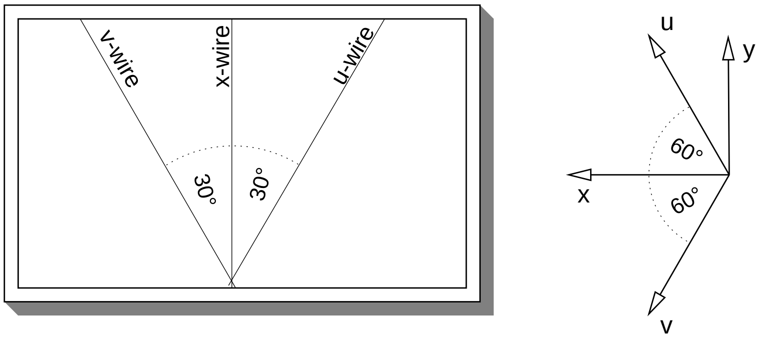

Figure 3.3: The arrangement of wires in the drift chambers and the direction of the measured projections x, u and v. y may be determined from the combination of u and v. In this figure z is pointing backwards in the direction of the beam.

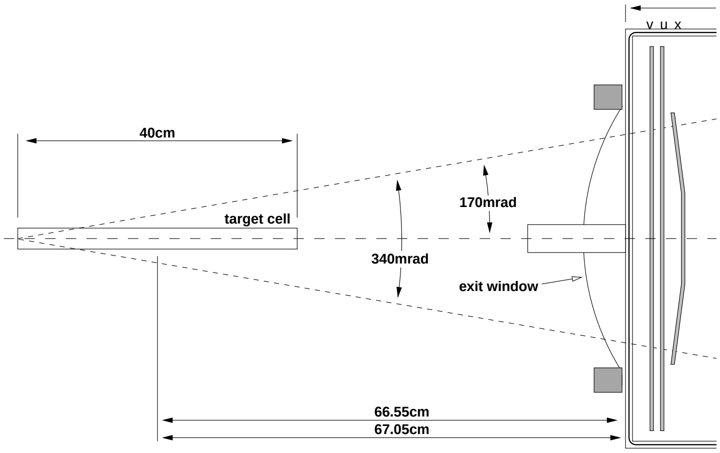

Figure 3.4: A schematic view of the vertex chambers. The x-planes of the chambers are in part inclined relative to the beam direction so as to provide angles as vertical as possible for the scattering products. Left in the figure the target is in the beam pipe of the positron machine at HERA. The vertex chambers are mounted shortly behind the exit window.

of aluminum which is vapor deposited every 193 μm onto a 300 μm thick glass plate. The voltage difference of 600 V between anode and cathode leads to charge multiplication in the ionizing gas similar to a proportional chamber.

The position resolution of a detector is determined through the standard deviation of the difference between the value measured by the detector and the actual course the particle took. The intrinsic resolution of the anode strip, with a width of $d =$

$193\mu\mathrm{m}$

$$\sigma = \sqrt{\frac{1}{d}\int_{-\frac{d}{2}}^{\frac{d}{2}} x^2\,dx} = \frac{193\mu\mathrm{m}}{\sqrt{12}} = 57\mu\mathrm{m} \tag{3.1}$$

can be increased to 45 $\mu\mathrm{m}$ using cluster formation and cluster analysis.

At the outer edges the x chambers are inclined towards the target by 120 mrad to increase the position resolution of the chambers by using a steeper passage angle. Unfortunately, this incline removes the applicability of the treesearch pattern recognition algorithm for the track search, leading to an increase in reconstruction time.

The vertex chamber has a digital readout, hence each hit is only assigned the appropriate cell number. To this end an APC module, developed at NIKHEF[BLO95], is mounted directly onto the substrate. By using an analog readout, which compares signal amplitudes of adjacent cells, it would be possible to increase the resolution to 30 $\mu\mathrm{m}$. However, the associated effort in the readout means a longer dead time of 250 $\mu\mathrm{s}$, which is unacceptable considering the expected HERMES trigger rates.

3.2.2 The Magnet Chambers

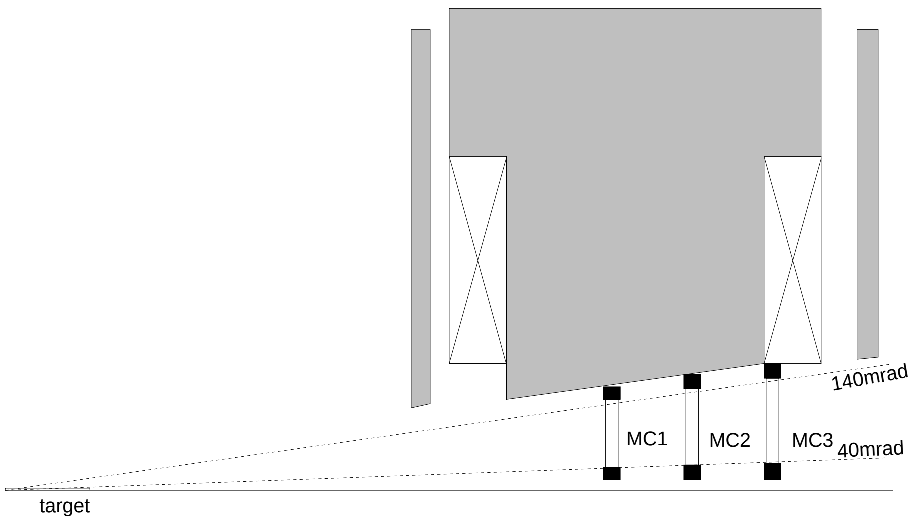

Figure 3.5: Cross section through the spectrometer magnet with the arrangement of the magnet chambers.

The proportional chambers, which are mounted inside the magnet (see figure 3.5), also provide digital information, i.e. whether a cell has been hit or not. They achieve a resolution of 577 $\mu\mathrm{m}$, with their inter wire distance of 2 mm according to equation (3.1) and should be used to connect front and back tracks.

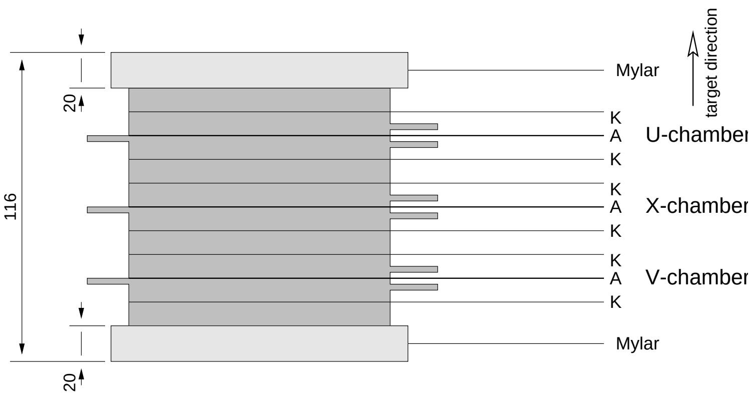

Figure 3.6: Schematic of a magnet chamber module.

Each chamber consists of two cathode foils between which anode wires are strung. They are combined in the order $u - x - v$ to detector modules. The module is closed off at each side by mylar foil (see figure 3.6).

The magnet chambers are read out using LeCroy PCOS-4 systems. The amplifiers and discriminators are located in the narrow space between the chambers at the magnet yoke, but outside of the acceptance.

3.2.3 The Drift Chambers

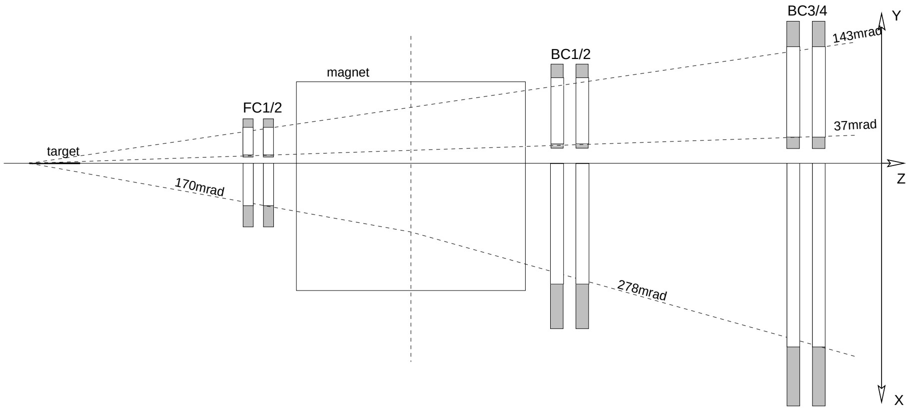

Figure 3.7: Acceptance of the drift chambers. Above vertical (side view), below horizontal (top view).

The drift chambers took on a particular importance in the first year of data taking. As they were the only completely functional tracking chambers, their calibration attracted a great deal of attention. The detectors FC1 and FC2, located in the anterior part of the detector in front of the magnet, are in principle not significantly different from the modules BC1 through BC4, which are situated further back. That is to say between the 7 cathode foils potential and signal wires are alternately strung in a gas mixture composed of Ar/CO_2/CF_4 (90/5/5). Two consecutive planes have the same wire orientation. However, the wires are shifted relative to one another in order to resolve ambiguities.

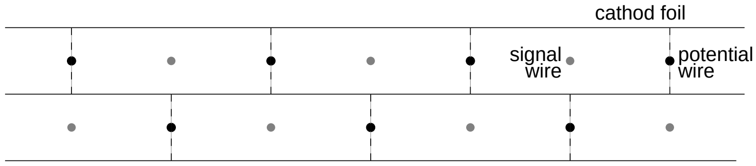

Figure 3.8: Arrangement of signal and potential wires in the x and x' plane.

The six chambers of a module are arranged in the order of u, u',x, x' and v, v'.

In contrast to the above mentioned detector types, drift chambers provide relatively few wires for read out. The potential wire distance is 7 mm in the front chambers and 15 mm in the back chambers. Each wire position has been measured with an accuracy of 20 μm [GUT95].

The position measurement is achieved through the analysis of the drift time: A passing particle ionizes the gas, as a result of this electron cascades move towards the signal wire with a constant velocity. The time measurement begins with the occurrence of a signal at the wire and ends simultaneously in all drift chambers at point in time which is shifted from the moment of the trigger by a constant – a common stop measurement.

From the thus determined drift time and with the aid of a table, the space drift time relation[HAS95], the distance between the originating spot of ionization and the signal wire may be determined (see figure 3.9). This distance is an absolute value, the drift direction is unknown, which leads to the so-called right-left ambiguity: For each hit there are two possible pathways to the left and right of the wire. Chapter 4.2.1 deals more specifically with this matter.

An equally graphic as useful diagram for the space drift time relation is the V-diagram, in which the determined drift time is set against the reconstructed track position in the chamber. With a correct calibration the graph of the function $f(x) = |x|$ should appear (see figures 3.10 and 3.11).

During data taking auto-calibration programs[MEI95] determine the space drift time relation from the data and directly show errors and deviations.

In test measurements with the BC modules resolutions of 150 μm have been measured. With resolutions of up to 200 μm these values have not yet been arrived at. However, the final calibration also has not yet been available.

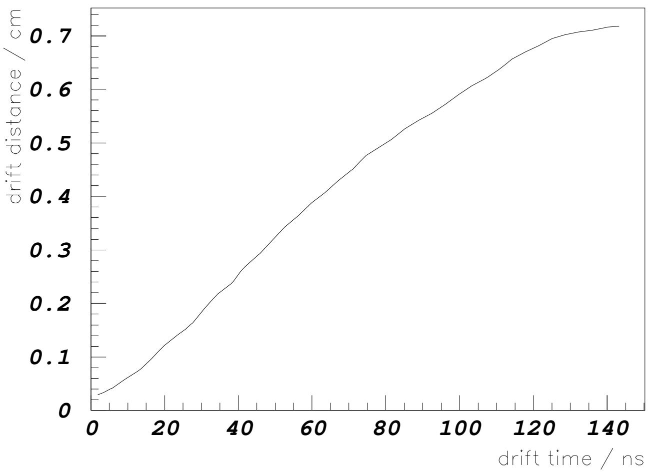

Figure 3.9: The space drift time relation for the back chambers.

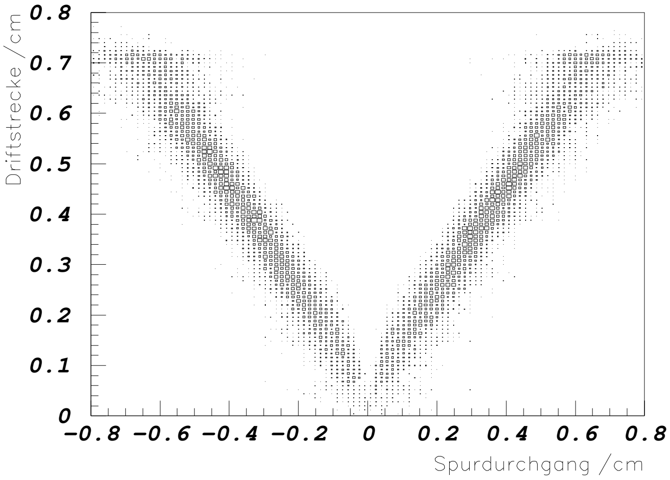

Figure 3.10: The so-called V-diagram contrasts the calculated drift distance from the space drift time relation and the measured track position.

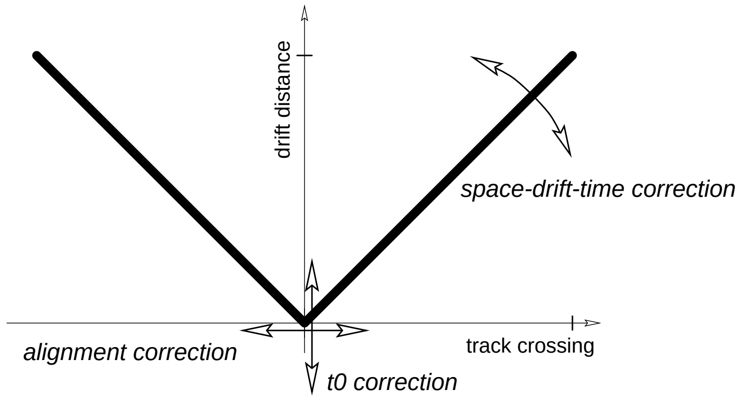

Figure 3.11: Three parameters can be calibrated through the V-diagram: a shift of the chamber in the projection direction of the wires leads to a horizontal shift of the 'V'. A change in t_0 leads to a vertical shift. A correct space drift time relation expresses itself in a slope of ± 1.0.

3.3 The Spectrometer Magnet

The spectrometer magnet in the center of the detector provides a field integral of $\int_z \vec{B} d\vec{s} = 1.3$Tm, in which charged particles are deflected, dependent on their momentum. The variance of the integral is less than 10% over the entire kinematic plane of the spectrometer. In order to minimize any influence on the HERA positron and proton beams, the beam pipes are located within a steel septum plate in the beam plane in the middle of the magnet. Additionally, a correction coil around the positron beam pipe serves to further attenuate the field. Scatter fields in the outer regions of the detector are similarly undesirable, which is the reason why field clamps were mounted in front of and behind the magnet, close to the boundaries of the acceptance. These reduce the field in the chambers FC2 and BC1 to less than 0.1 T.

The energy demand of the magnet was significantly reduced through the the slanted pole surfaces (see figure 3.12), which also adds to the inhomogeneity of the field. The field shape within the magnet is depicted in figure 3.13. Already at the construction stage the expected magnetic field was calculated with the MAFIA program. This calculation shows only minor discrepancies with the final precision measurement[ROE94].

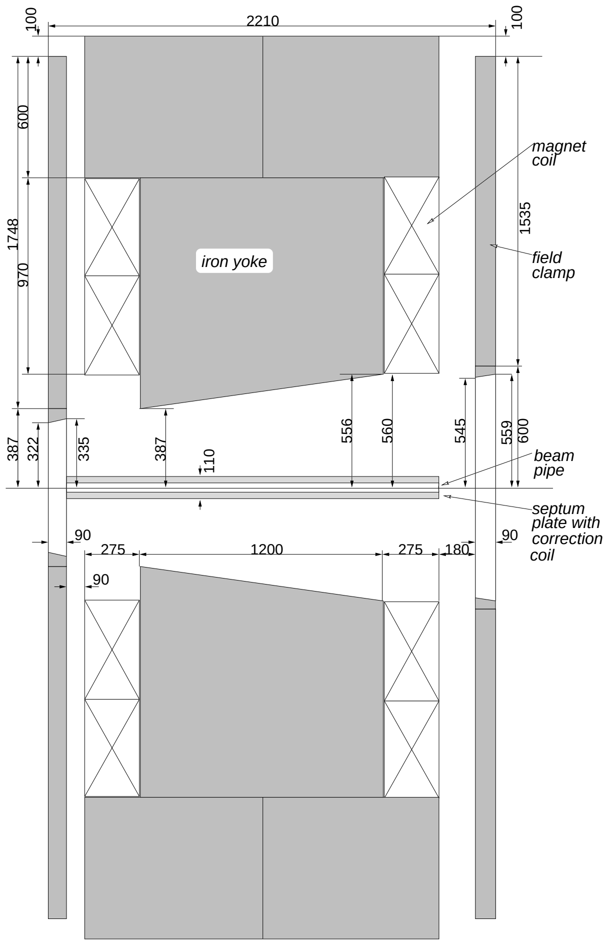

Figure 3.12: Schematic side view of the spectrometer magnet.

3.4 The Particle Identification Detectors

3.4.1 The Lead Glass Calorimeter

The two halves of the calorimeter each consist of 42×10 blocks of radiation resistant lead glass F101 measuring $9 \times 9 \times 50\mathrm{cm}^3$. The length of 50 cm corresponds to 18 radiation lengths in lead glass F101. Photomultipliers situated behind the individual cells evaluate each produced light pulse, where an energy resolution of

$$\frac{\Delta E(E)}{E} = 1.47\% + \frac{5.14\%}{\sqrt{E/GeV}} \tag{3.2}$$

for positrons could be reached[DUE95]. Since pions shower significantly less in the calorimeter the ratio of E_{cal}/P for known momentum P is a good parameter for pion suppression.

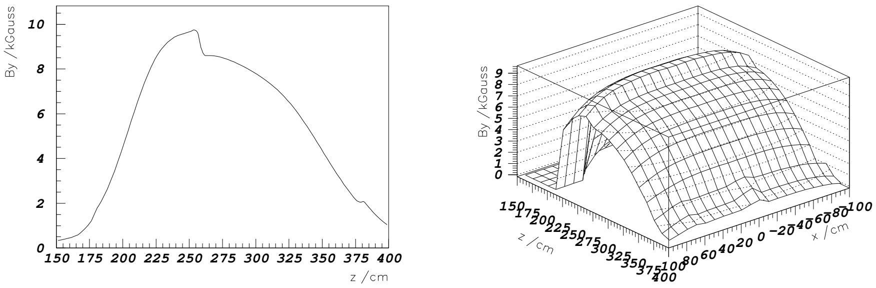

Figure 3.13: Field inside the magnet. Left along a line at x=0 cm, y=10 cm, right in the plane y=10 cm.

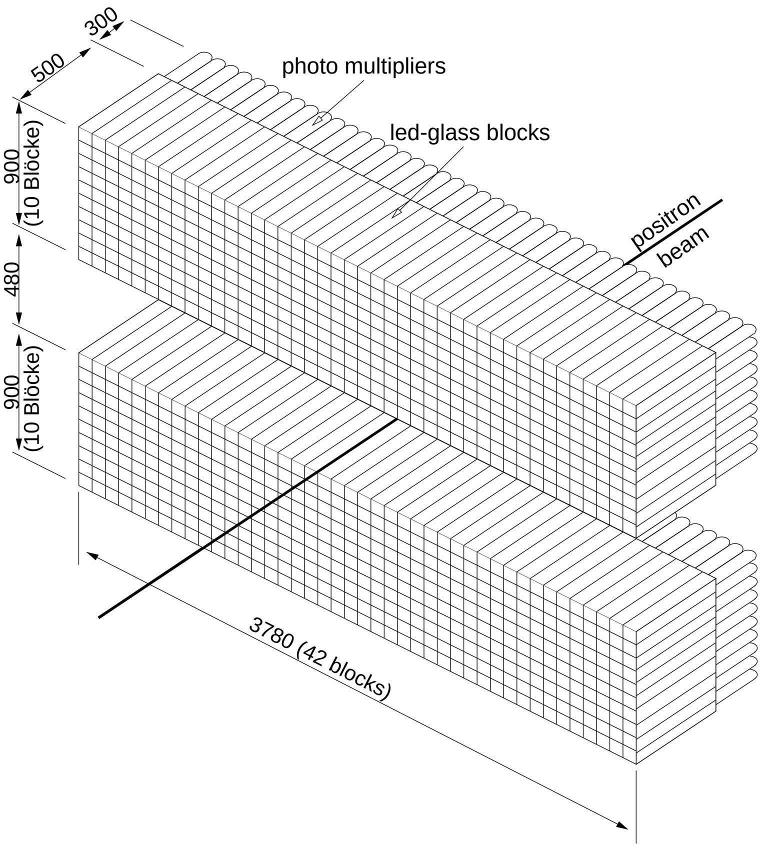

Figure 3.14: Schematic drawing of the calorimeter.

3.4.2 The Hodoscopes

Hodoscopes are used in the HERMES experiment in two different functions. The trigger hodoscope is located directly behind the drift chambers BC4. It's signal is

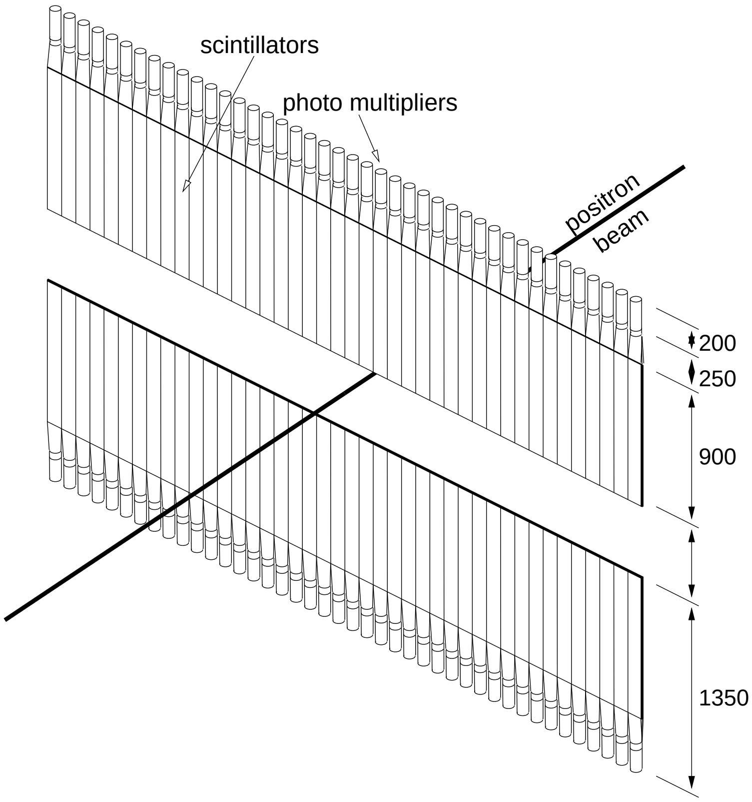

Figure 3.15: Schematic drawing of a hodoscope plane.

used for the hardware trigger together with a calorimeter threshold. This hodoscope has no importance for the analysis, because the scintillators represent only 2.3% of a radiation length and therefore allow no energy measurement. The second hodoscope, the 'preshower' is located behind the transition radiation detector and a 1.1 cm thick layer of lead, in which electrons/positrons and photons shower and therefore produce a signal in the scintillator material that is almost proportional to their energy (see chapter 4.12.1). Both hodoscopes consist of 2×42 scintillator paddles, that are arranged along the x direction above and below the beam pipe (see figure3.15).

3.4.3 The Cerenkov Counter

The Cerenkov counter is located between the drift chambers BC1/2 and BC3/4. Including the window foils of Mylar (100 $\mu\mathrm{m}$) and Tedlar (30 $\mu\mathrm{m}$), the nitrogen gas and the mirrors, this detector has a radiation length of 3.5%. Hence, it can be used in front of the second set of drift chamber modules without any significant influence on the momentum measurement. Highly relativistic particles ($\beta \longrightarrow 1$)

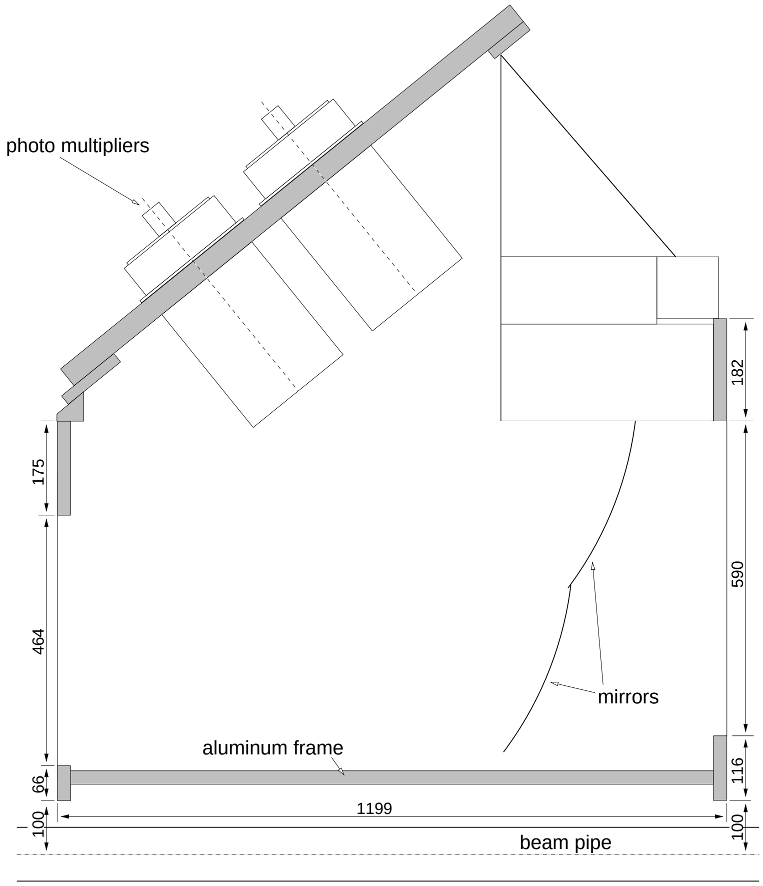

Figure 3.16: Schematic side view of the top Cerenkov counter.

produce an average of 10 Cerenkov photons, which are reflected by 2×10 mirrors into as many photomultipliers. This detector is able to separate e,π from K,p in the energy range from 4.4 GeV to 15.8 GeV. Only protons still are below the Cerenkov threshold between 15.8 GeV and 30 GeV.

This threshold cerenkov may in the future be replaced by a RICH (Ring Image Cherenkov), which will allow the identification of the different hadrons over the entire kinematic range.

3.4.4 The Transition Radiation Detector

Transition radiation is emitted by highly relativistic particles ($\gamma > 1000$) when they cross the boundaries between materials with different dielectric constants. This effect may be used for particles above 3.5 GeV to separate electrons ($\gamma > 7000$) and hadrons ($\gamma < 250$).

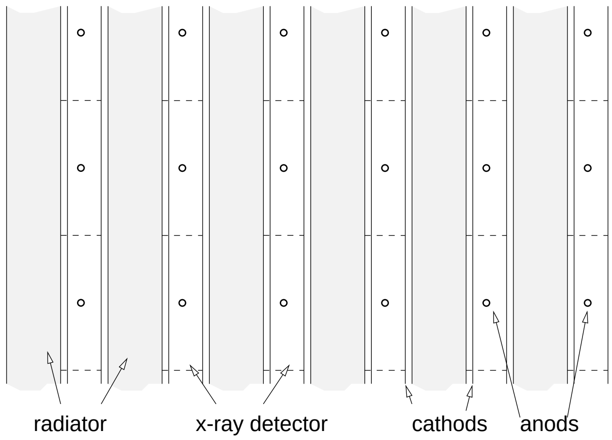

Figure 3.17: Cut through the transition radiation detector in the x-z plane.

The HERMES transition radiation detector consists of 6 consecutive modules, which each consist of a radiator and an X-ray detector. The transition radiation photons are created inside the radiator, which consists of polypropylene fibres with a diameter of 17-20 μm with a density of 100 mg/cm^3. The transition radiation photons have energies in the range of 2 – 15 keV. The following X-ray detector is a planar wire chamber filled with Xe (90%) and CH_4 (10%), optimized for the detection of low energy photons. The signal amplitudes on the individual wires are read out with analog to digital converters.

Correlated backgrounds, e.g. bremsstrahlung photons or δ-electrons, also produce signals in the X-ray detector, but typically only in one of the six detectors along a particle trajectory. This background can be suppressed by using an appropriate average response that uses only the five lowest signals. The electron-hadron separation in the transition radiation detector is better than 100:1 [EME95].

3.5 The Luminosity Monitor

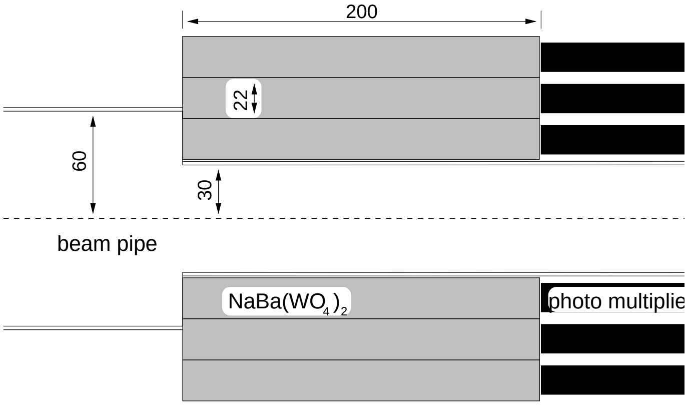

Figure 3.18: Overview of both halves of the luminosity monitor on the left and right side of the beam pipe.

The luminosity measurement is based on a coincidence measurement of e^+e^--pairs that result from Bhabha scattering on the target electrons and from photon pairs that are created by e^+e^--annihilation inside the target. The coincidence rate is practically free of background and is proportional to the product of electron density in the target and beam current. For a helium target with a target density of $1 \cdot 10^{15} \frac{\mathrm{nucleons}}{\mathrm{cm}^2}$ and a positron current of 28 mA the coincidence rate is for example 96 Hz. The two calorimeter blocks of the monitor are located 7 m downstream from the target at an especially narrow section of the beam pipe on the left and right side of the positron beam (see figure 3.18). They consist of 4×3 blocks of radiation resistant $NaBi(WO_4)_2$ measuring $22 \times 22 \times 200\mathrm{mm}^3$, and serve to measure the energy of the electrons, positrons and photons (10-20 GeV)[BEN95].

Chapter 4

The HERMES Reconstruction Program

The task of the HERMES analysis chain is the transformation of the data from the single detectors and the detector control into histograms for the physics analysis.

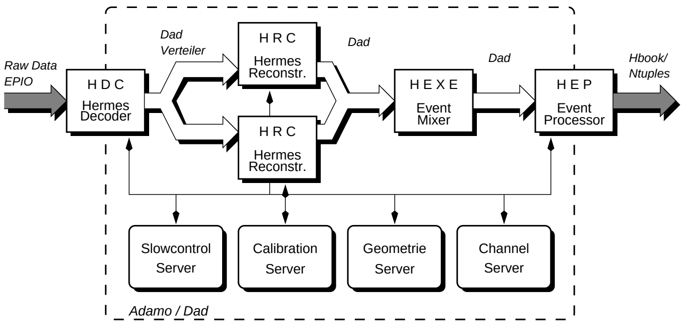

Figure 4.1: The data-flow of the event data in the HERMES experiment

The event builder combines the detector data to a data-flow of events (figure 4.1) in EPIO (Experimental Physics Input Output Package) format. The HERMES decoder (HDC) converts the pulse height and time information from ADC (Analog Digital Converter) and TDC (Time Digital Converter) values into position and energy values. These pre-calibrated values are stored in ADAMO[PTG94] or DAD[WAN95] (see chapter A) format, which are the standard formats for the further analysis. The HERMES reconstruction program, HRC, uses these data to determine particle tracks, momenta and particle types. HEP- the HERMES event processor – finally produces the histograms.

The most time critical component of this analysis chain is HRC itself. For this reason special care was taken in the optimization of the reconstruction process.

4.1 The Structure of the Reconstruction Program

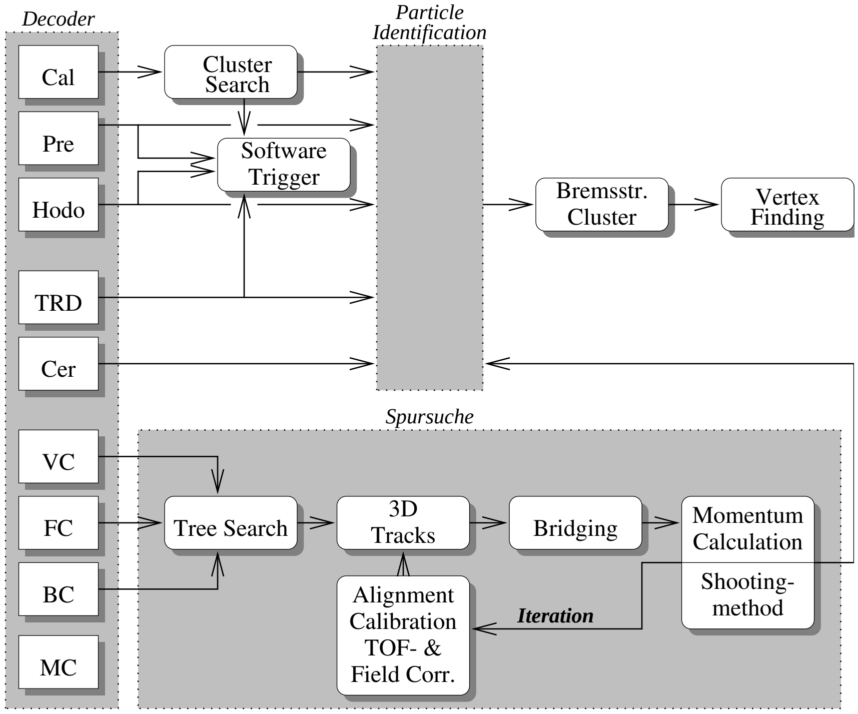

Figure 4.2: Flow Chart of the Reconstruction

HRC gets its data from the HERMES decoder HDC(on the left side in figure 4.2). First the tracking detector data are used to find tracks. Beginning with tracks in the projections in the regions in front of and behind the magnet partial tracks are assembled. Then the partial tracks are combined to trajectories in space by *bridging* and the charge and the momentum of the particles are determined. The particle identification detectors (Cerenkov, TRD, hodoscope and calorimeter) are used to try to find the particle type for each trajectory. In the following chapters the different components of the reconstruction process are discussed in detail.

4.2 Treesearch

Treesearch is a pattern recognition algorithm that identifies straight lines in a picture and so efficiently finds tracks in detector systems [DOR89, BAT90a, BAT90b, DOR90]. The algorithm is based on the use of a pattern data base, that contains all possible particle tracks for a given detector system and resolution.

Novel in the HERMES experiment is the use of treesearch for a large detector and a high resolution of the pattern data base. This is made possible by compressed

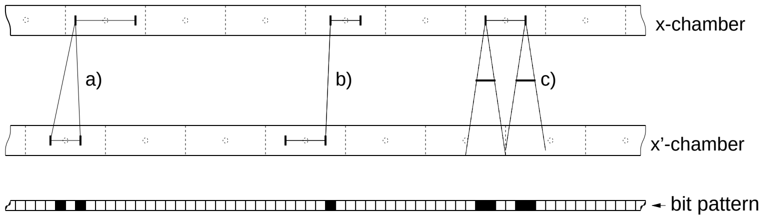

Figure 4.3: Resolution of drift chamber ambiguities. In example a) two tracks are possible within the maximally allowed angle; the passage in the middle between both chambers is entered into the bit pattern. In example b) only one track is possible, while in example c) only of the chambers has fired. As a result the bit pattern has to be broadened corresponding to the maximal acceptance angle.

storage of the patterns.

4.2.1 Track Finding

In order to find a track, the recorded hits from each detector are encoded in a bit pattern of 2^n bits – n is chosen in such a way that the width of a single bit is about 3 to 5 times the detector resolution. The drift chambers provide only the information regarding the distance to the signal wire that a particle has passed instead of the position of the particle track. The resulting right-left ambiguity of two potential track positions per recorded hit is resolved by combining the responses of two consecutive chambers with the same wire orientation (see figure 4.3). The vertex chamber hits are unambiguous and can be transferred directly into the corresponding bit patterns. In both cases the detector resolution is taken into account to widen the bit pattern for single hits if necessary.

In this way a one dimensional bit array is created for each detector and these arrays can be combined into two-dimensional pictures for all chambers with the same wire orientation. Henceforth this picture will be referred to as the detector pattern. As the treesearch pattern data base contains one entry for every potential particle track, this data base makes it possible to generate every detector pattern that is caused by particle tracks alone. Conversely, any track can be filtered out of the detector pattern by matching against the pattern data bank.

126 million tracks are stored in the data bank in the case of the treesearch resolution used for HERMES. A linear method is impractical, both in storing 126 million tracks and in the large number of pattern matchings used in track finding.

Instead the detector pattern at different artificially reduced detector resolutions is compared recursively with the bit patterns from the data bank (see figure 4.4). This starts with a '2-bit detector' that only differentiates between a particle that produced a signal in the left or the right half of the detector. The resolution is successively doubled, reaching, after 11 or 10 steps, respectively, a track width of

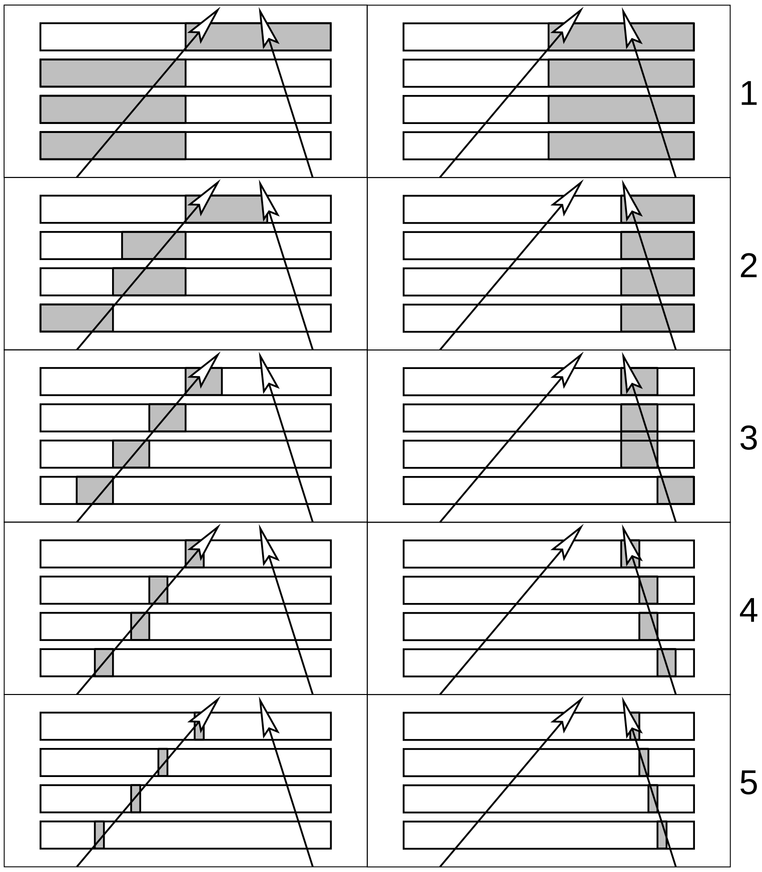

Figure 4.4: Treesearch for two tracks. The detector pattern is matched against the pattern data bank with increasing resolution (from top to bottom).

$2890\mathrm{mm} \times 2^{-11} = 1.4$ mm in the back and of $660\mathrm{mm} \times 2^{-10} = 0.6$ mm in the front area of the detector.

For each detected pattern of a given resolution, also referred to as a parent pattern, only a limited number of child patterns (at doubled resolution) exist that fit into the former. This leads to a significant reduction in the number of necessary pattern matchings (see figure 4.5). For a treesearch depth of 11 levels an average of 70 pattern matchings is necessary to define a track.

The track search algorithm is highly recursive. A linear procedure to search the the pattern data bank would find maximally one track, because only one matching pattern and one of its children might be used for each level of resolution. The flow chart in figure 4.6 illustrates the recursive character of treesearch. Beginning with the trivial pattern at a resolution of one bin (detector has a hit or not) all child patterns at doubled resolution are examined. If a matching pattern is found, the depth of the recursion is increased and the patterns are compared at again doubled reso-

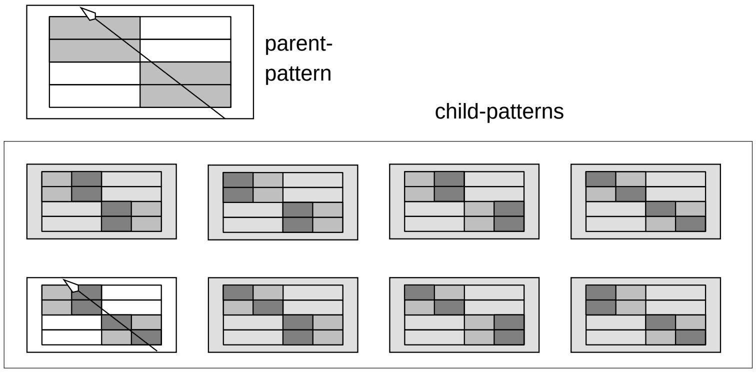

Figure 4.5: Pattern Matching: Every parent pattern has an average of 4-8 child patterns. After doubling the resolution the child patterns are used for the pattern matching. The child pattern that matches the track is marked by a white background.

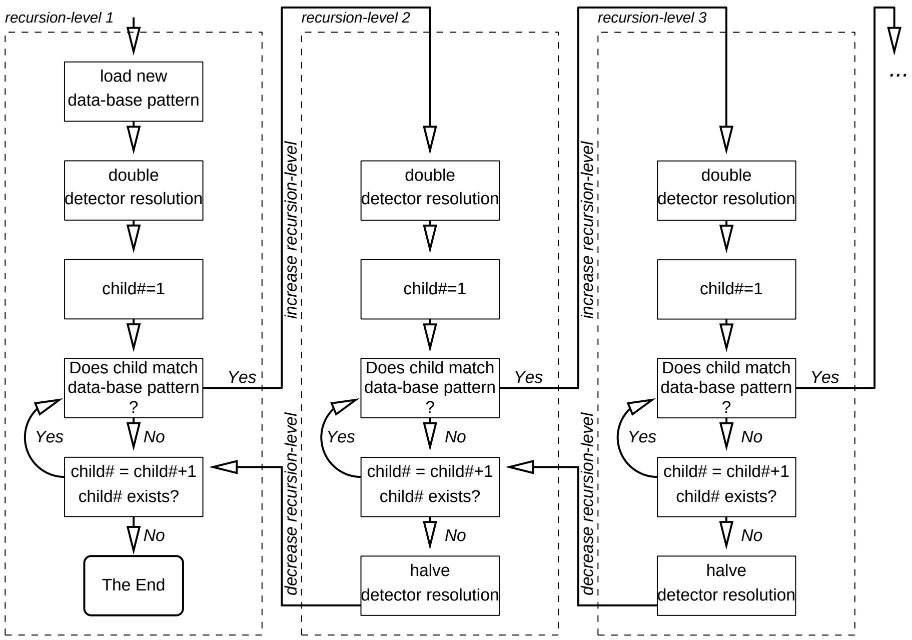

Figure 4.6: Flow chart of the recursive track search in treesearch. The different levels of recursion are shown next to one another for illustration only, the program code only exists once.

lution. Once this initial pattern matching is complete all other child patterns from the original level of resolution are tested and the track search is maybe repeated again into higher resolutions.

Two important problems with treesearch and their solutions should be mentioned here:

Chamber Efficiency The efficiency of the detectors is less than 100%. This may lead to holes in the detector patterns of valid tracks, both in the combined information from the staggered drift chambers and also in the vertex chambers. By reducing the required level of agreement, e.g. to 3 out of 4 bits, treesearch can also identify valid tracks that contain holes.

Binning Problems The uncertainty of the position measurement can also influence the detector pattern in such a way that a wrong bit in the pattern may be set. In this case it may happen that treesearch is not able to put a straight line through the detector pattern. There are two possible solutions: a) treesearch can be applied several times with varying bin borders, b) possible uncertainties are taken into account when the hits are entered into the data bank and the pattern is broadened accordingly. While HRC has both options, the latter is faster and has a higher reconstruction efficiency.

4.2.2 The Pattern Data Bank

The data bank is generated starting from a parent pattern by producing all 2^D ($D =$ number of detectors) potential child patterns and testing whether they could correspond to a particle trajectory (see figure 4.7). Further generations are only produced for valid particle tracks.

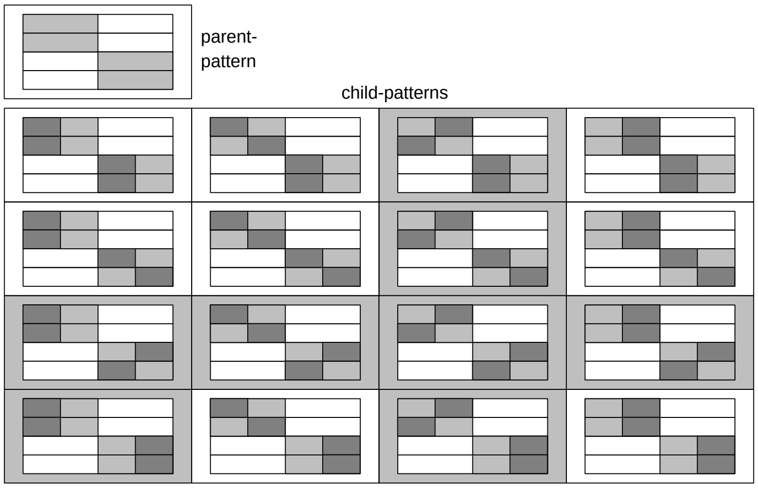

Figure 4.7: Generation of the pattern data bank. The possible 16 child patterns are tested with regard to physical plausibility. In this example only eight patterns (white background) correspond to potential particle tracks.

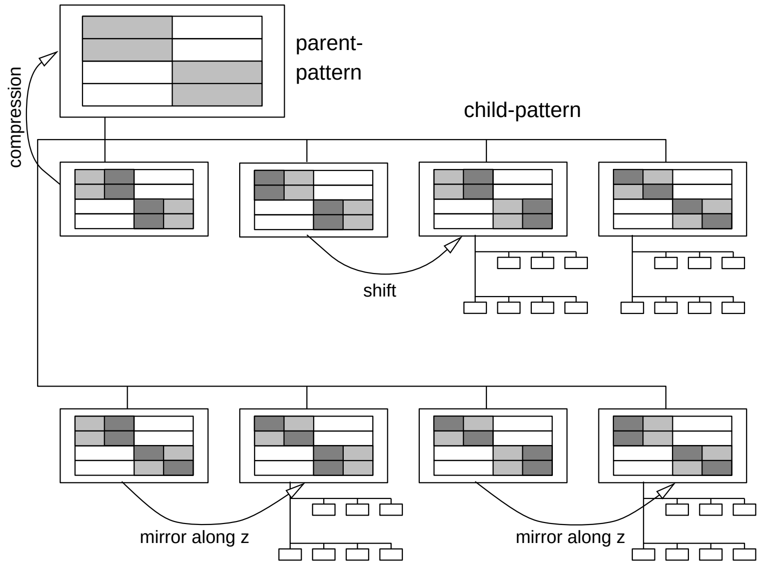

Figure 4.8: Compressing the pattern data bank by symmetry arguments. Assuming straight tracks in a detector that is symmetric with regard to the beam axis squeezed, shifted and reflected patterns only have to contain a reference to the original.

While this solves the problem of the large number of pattern comparisons, the problem of storing the data bank remains.

The required storage space can be reduced to a small fraction by using symmetry arguments. Assuming that the tracks are straight outside of the magnetic field, which is a good approximation in front of and behind the spectrometer magnet, patterns can be transformed into one another by shifting, squeezing and reflecting. This way only a reference to the original has to be stored and the size of the data bank can be reduced from 126 million to 31,000 entries (see figure 4.8).

In the absence of these symmetries treesearch cannot be used with high resolutions. For this reason the x-projection of the front half of the detector is not analyzed with treesearch, as the vertex chamber modules that are inclined relative to the beam axis violate the symmetry (see figure 3.4).

4.3 Track Parameters

After a track has been identified by treesearch the hits in the 'road' along the track can be used to determine the line parameters of the track projection. The parameters are calculated for all possible permutations of hits on the road. (see figure 4.9).

Needed are the y-axis intersection (g_x) and the slope ($g_{x'}$) of the linear function $x(z) = g_x + z \cdot g_{x'}$, where x may of course also be replaced by u and v. These parameters ($\vec{g}^\top = (g_x, g_{x'})$ are derived by minimizing the squared distance between hits and linear trajectory. If all measured hits have the same uncertainty this calculation follows the known formula

$$A^\top A\vec{g} = -A^\top \vec{x}. \tag{4.1}$$

Here is

$$A = -\begin{pmatrix} 1 & z_1 \\ 1 & z_2 \\ & \vdots \\ 1 & z_N \end{pmatrix} \tag{4.2}$$

and $\vec{x}^\top = (x_1, x_2, \ldots, x_N)$ is the vector of x-positions for the N hits in the D detectors ($N \leq D$) of a possible permutation. Correspondingly $\vec{z}^\top = (z_1, z_2, \ldots, z_N)$ is the z-position vector.

However, if the measured values have different uncertainties, a weight matrix is needed in equation (4.1) (see [BRA92]):

$$A^\top \cdot G \cdot A\vec{g} = -A^\top \cdot G\vec{x}. \tag{4.3}$$

This weight matrix is defined as the inverse of the covariance matrix C of the uncertainties:

$$G = C^{-1}, \tag{4.4}$$

with

$$C = \begin{pmatrix} {\sigma_1}^2 & 0 & \cdots & 0 \\ 0 & {\sigma_2}^2 & \cdots & 0 \\ \vdots & \vdots & \ddots & \vdots \\ 0 & 0 & \cdots & {\sigma_N}^2 \end{pmatrix}, \tag{4.5}$$

where the correlations between hits that belong to the same track ($\sigma_j \sigma_i,\ i \neq j$) are neglected at this point.

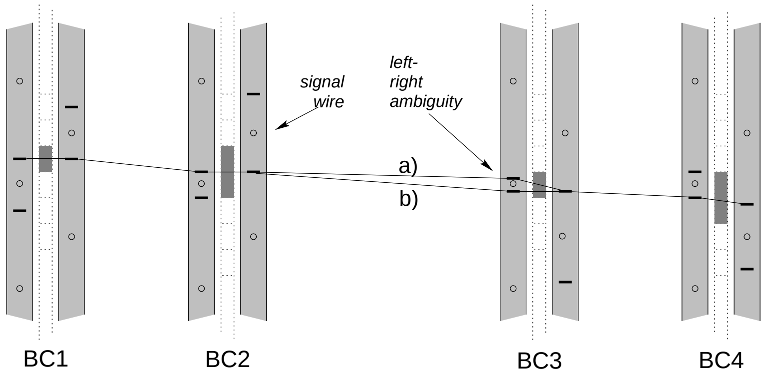

Figure 4.9: Track searching in the treesearch roads. In this example the back drift chambers of a particular wire orientation are shown. The chambers of a module are shifted relative to one another by pairs. The pattern that was found by treesearch is shown between them. Within this road two linear functions are possible – due to the right-left ambiguity. Function b) is selected as the result of the χ^2 comparison.

The covariance matrix of the linear function parameters $\vec{g}$ can be calculated by error propagation from

$$C_g = \left(A^\top \cdot G \cdot A\right)^{-1}. \tag{4.6}$$

If several possible tracks are found within one road defined by treesearch, the smallest χ^2-value

$$\chi^2 = \frac{1}{N-2}\sum_{i=1}^{N}\frac{1}{\sigma_i^2}(x(z_i) - x_i)^2 \tag{4.7}$$

determines the parameters that are finally used (see figure4.9).

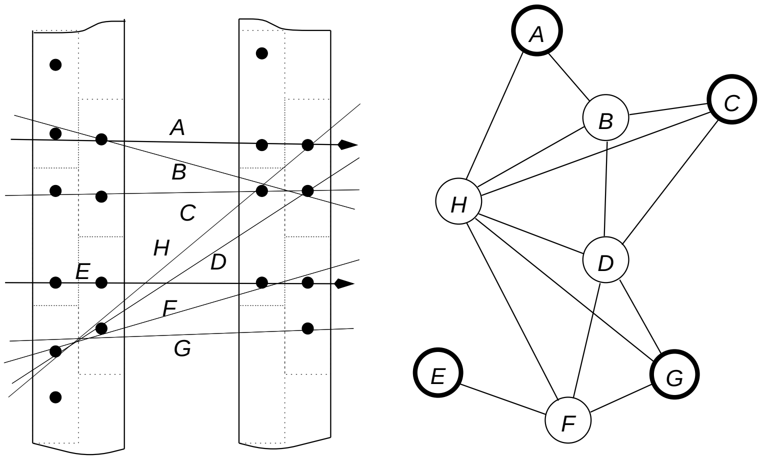

Figure 4.10: Left: Ghost tracks in the HERMES front chambers (Monte Carlo events): Only the tracks A and E correspond to generated particles. Due to the right-left ambiguity of the chambers eight possible particle tracks are found. Right: Connection graph of the tracks. By eliminating the nodes with large edge count (intersections with other tracks) ghost tracks may be largely excluded. Only the bold lined nodes in the diagram correspond to tracks that are examined further.

4.4 Ghost Tracks

Particularly in detector systems with low redundancy the problem of ghost tracks occurs in addition to the lowered efficiency. Ghost tracks are tracks that are visible in the detector system as a series of hits on a straight line but do not belong to a real particle. Figure 4.10 (right side) shows the development of ghost tracks in the HERMES front chamber system, which currently only consists of four detectors per projection. (The vertex chambers are not yet used by default due to problems with the readout electronics.) In the case of the passage of two tracks through neighbouring drift cells, enhanced by the right-left ambiguity, eight ghost tracks are formed. The elimination of these tracks is of much interest, because they contaminate the true measurement with random data. Alternately, the double-track resolution can be reduced significantly by a selection that is too rigorous.

The connection graph as described in [GRO90] proves to be an attractive ansatz. All tracks in the detector are represented as nodes in a graph and those nodes with common hits are connected. To eliminate ghost tracks, nodes with large edge count are removed from the graph. In the example in figure 4.10 four tracks remain after this elimination. The two remaining ghost tracks could certainly have belonged to reasonable tracks, which this method takes into account. They will be eliminated later in the combination to three dimensional tracks, or in the ghost track elimination that is performed on the three dimensional tracks in the same manner as on the projection tracks.

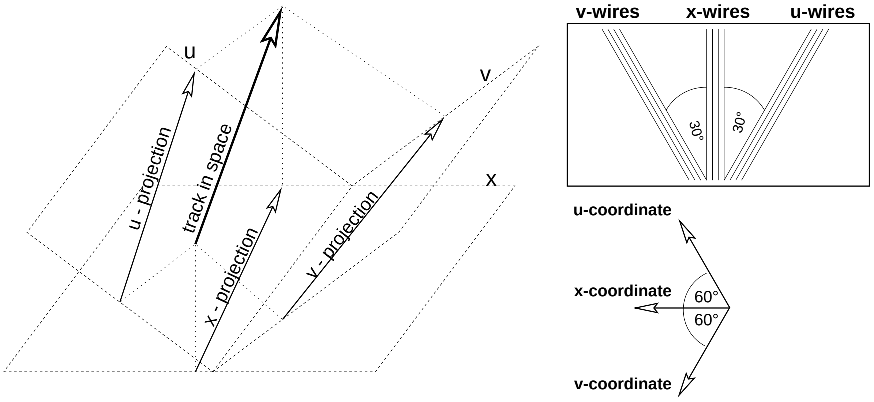

Figure 4.11: Combination of trajectories in the u-, v- and x-projection to a three dimensional track. From the track parameters in u and v a potential trajectory in x is calculated and compared to the trajectories that were found in the x-projection.

4.5 Tracks in Three Dimensions

So far particle trajectories have been only identified and calculated in the projections of the tracking chambers. These projections still have to be combined to three dimensional tracks.

In the back detector, where particle trajectories are found in u-, v- and x-projections, tracks can be constructed as shown in figure 4.11. The parameters of the linear function in x are calculated from all combinations of trajectories in u and v and later compared to the trajectories in x.

In the front detector treesearch cannot be used in the x-projection. Potential tracks in x are again calculated from all combinations of the trajectories in u and v. These x-tracks are then used to define a road in the x-projection of the chambers. From the hits within this road the track parameters in x are calculated analogously to chapter 4.3,

The final three dimensional track is described as

$$\vec{x}(z) = \begin{pmatrix} g_x \\ g_y \\ 0 \end{pmatrix} + \begin{pmatrix} g_{x'} \\ g_{y'} \\ 1 \end{pmatrix} \cdot z \tag{4.8}$$

and is calculated from the parameters of the track projections as follows. The transformation $(x, y) \to (u, v)$ is defined by

$$\begin{pmatrix} u \\ v \end{pmatrix} = B \begin{pmatrix} x \\ y \end{pmatrix} \quad \text{, with } B = \begin{pmatrix} \cos(+30°) & \sin(+30°) \\ \cos(-30°) & \sin(-30°) \end{pmatrix}, \tag{4.9}$$

and the inverse transformation $(u, v) \to (x, y)$ is given as

$$\begin{pmatrix} x \\ y \end{pmatrix} = A \begin{pmatrix} u \\ v \end{pmatrix} \quad \text{, with } A = B^{-1}. \tag{4.10}$$

As x is defined by (u, v) as well as from its direct measurement, the resulting value of x is found by combination of both measurements, weighted by the respective uncertainties:

$$\begin{pmatrix} x \\ y \end{pmatrix} = T_1 \begin{pmatrix} u \\ v \\ x \end{pmatrix}_{\mathrm{proj}} , \tag{4.11}$$

$$\text{with } T_1 = \begin{pmatrix} A_{11} \frac{\Delta x_x^2}{\Delta x_x^2 + \Delta x_{uv}^2} & A_{12} \frac{\Delta x_x^2}{\Delta x_x^2 + \Delta x_{uv}^2} & \frac{\Delta x_{uv}^2}{\Delta x_x^2 + \Delta x_{uv}^2} \\ A_{21} & A22 & 0 \end{pmatrix} .$$

A vector $\vec{x}_{\mathrm{proj}}$ indicates that the coordinates belong to the projection measurements, while vectors without index proj were calculated from these. This distinction is important, because $x = x(u_{\mathrm{proj}}, v_{\mathrm{proj}}, x_{\mathrm{proj}}) \neq x_{\mathrm{proj}}$.

The slopes of the tracks transform in an analogous way, so that the parameters of the three dimensional track may be calculated as

$$\begin{pmatrix} x \\ y \\ x' \\ y' \end{pmatrix} = T \begin{pmatrix} u \\ v \\ x \\ u' \\ v' \\ x' \end{pmatrix}_{\mathrm{proj}} \quad \text{, with } T = \begin{pmatrix} T_1 & 0 \\ 0 & T_1. \end{pmatrix} \tag{4.12}$$

The covariance matrix for the track parameters $(xyx'y')$ is given as

$$C_{xy} = T C_{uvx} T^{\top}, \tag{4.13}$$

where C_{uvx} is the combined covariance matrix of the parameters of the projection trajectories:

$$C_{uvx} = \begin{pmatrix} C_{uu} & 0 & 0 & C_{uu'} & 0 & 0 \\ 0 & C_{vv} & 0 & 0 & C_{vv'} & 0 \\ 0 & 0 & C_{xx} & 0 & 0 & C_{xx'} \\ C_{u'u} & 0 & 0 & C_{u'u'} & 0 & 0 \\ 0 & C_{v'v} & 0 & 0 & C_{v'v'} & 0 \\ 0 & 0 & C_{x'x} & 0 & 0 & C_{x'x'} \end{pmatrix} \tag{4.14}$$

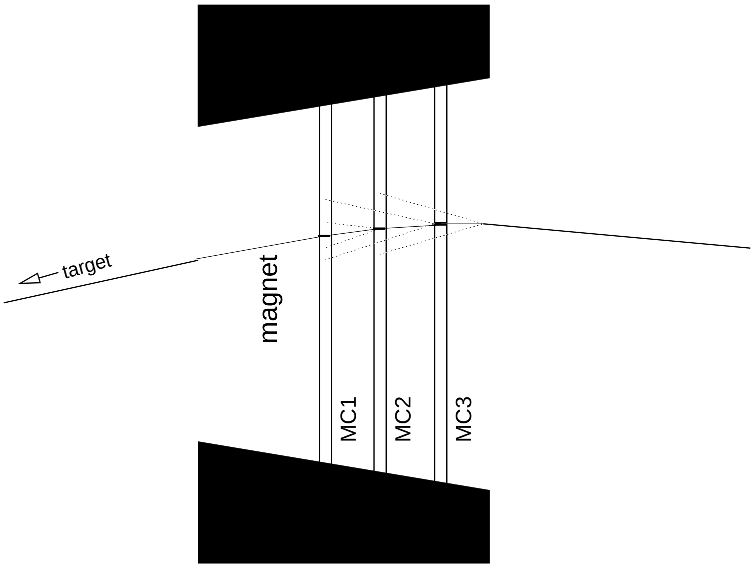

Figure 4.12: Kalman-Filter in the magnet. The partial back track is extended into the magnet and defines regions in the magnet chambers that are examined for hits.

4.6 Combination of the Partial Tracks

So far partial tracks in the front and back detector have been found, which now have to be combined to tracks going through the magnetic field of the spectrometer. HRC uses several methods for this:

4.6.1 A Kalman-Filter through the Magnet

In this method partial back tracks are used to define the region within the magnet where hits from the particle should have been seen. This definition includes information about the magnetic field and the maximal deflection for a particle above a certain momentum. Only small deviations are expected in y, larger ones in x. A hit in the last magnet chamber that could be identified using the u, v and x information is assumed to be part of the trajectory and the search is extended to the next magnet chamber (see figure 4.12). If no hit could be identified in the last chamber, the track can still be continued by a hit in the next chamber, given that at least two out of three chambers registered a signal.

At the present time this method is only used in tests, because the magnet chambers were not fully functional during the first year of HERMES data taking and a combination of u, v and x information to hits in three dimensions was only possible for a few regions.

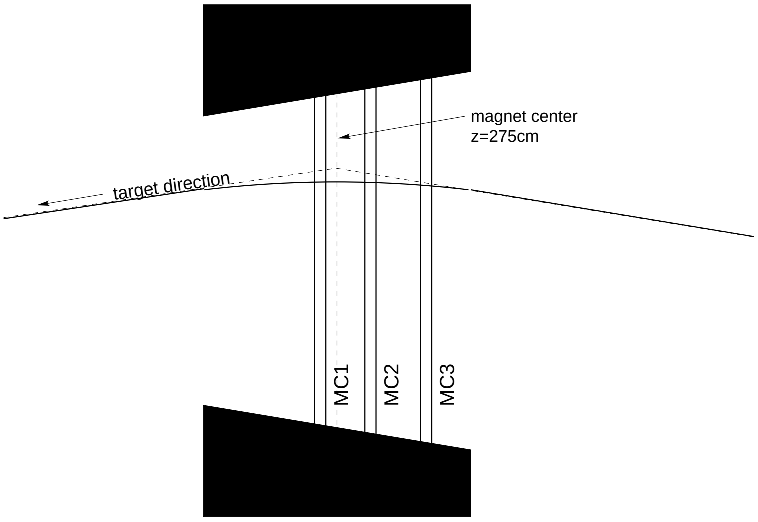

Figure 4.13: Combination of front and back tracks inside the magnet. In th x projection (shown here) as well as in the y projection, where the deflection due to the magnet is small, the extensions of front and back track meet almost exactly in one point in the middle of the magnet.

4.6.2 Position Comparison in the Center of the Magnet

The intersections of the partial front and back track with the $x - y$ plane in the center of the magnet ($z = 275$cm) lie very close to one another. The deviations between them are up to 1.0 cm for low energy particles and become accordingly smaller for higher energy (and thus less deflected) particles (see figure 4.14).

By using this fact, candidates that belong to one track can be found with high probability. For an improved analysis HRC can use an internal table (10^6 entries) that contains the distance between both intersection points as a function of vertex position, vertex angle and particle energy with an accuracy of 200 $\mu\mathrm{m}$. This resolution is strongly dominated by the chamber resolution and scattering effects.

4.6.3 Forced Bridging

In case the vertex chambers are not functioning, the partial tracks can be forced to agree in the center of the magnet. This idea by Pavel Galumian[PAV95I] improves the angle resolution significantly. A reconstruction based only on the front chambers FC1 and FC2 would be dominated by their relatively low position resolution.

The algorithm originally assumed that partial front and back track meet exactly in the middle of the magnet and calculated the momentum from the re-calculated parameters of the front track (see chapter 4.8).

By iterating the procedure (see figure 4.15) to take deviations from an exact agreement of the partial tracks into account the momentum resolution could be improved considerably.

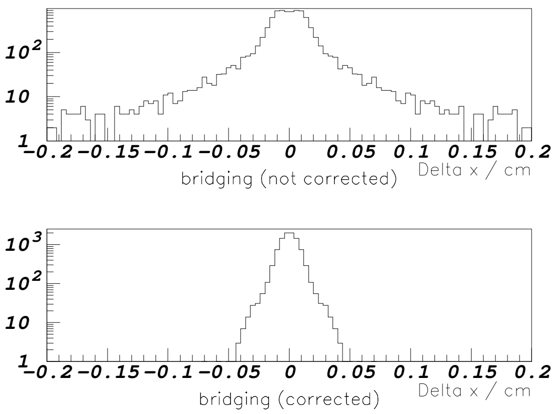

Figure 4.14: The histograms show the distance between the intersections of front and back track with the center plane of the magnet. The observed good agreement may be used to match front and back track. The top histogram does not include the offset correction, while the bottom one does.

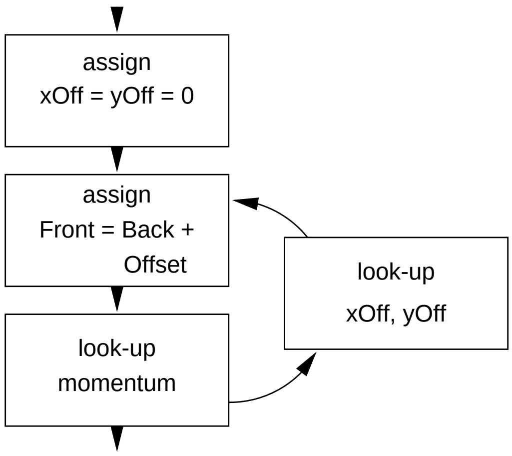

Figure 4.15: Flow chart of the forced bridging. In the beginning it is assumed that the extensions of front and back track match exactly in the middle of the magnet. With this assumption a first estimate of the momentum is calculated from which the partial front track is re-calculated. This results in an improved momentum measurement and a more exact track correction. After 2-3 iterations the required accuracy is reached.

4.7 Interpolation of the Magnetic Field

The magnetic field is available as a lattice measurement of the three field components B_x, B_y and B_z, where the distances of the lattice nodes is 4.8 cm in x, 9.8 cm in y and 1 cm in z. The nodes of the lattice themselves were measured with an accuracy of $\Delta B < 1$ G and $\Delta x < 50\ \mu\mathrm{m}$. More detailed information about the measurements by A.Izotov and G.Röper and the, in part, sophisticated correction calculations may be found in [ROE94].

It was important for the analysis to have a fast method for interpolation with high differentiability, so as to keep the calculation of particle trajectories inside the magnet efficient.

Linear interpolation of the support points (x_i, y_i)

$$y_i(x) = (x - x_i)\frac{y_{i+1} - y_i}{x_{i+1} - x_i} + y_i \quad , x_i \leq x < x_{i+1}, \tag{4.15}$$

is frequently used (see e.g. [COR92]), but offers no differentiability in the support points (see figure 4.16 top).

Quadratic interpolation

$$a_i(x) = a_i^{(2)} x^2 + a_i^{(1)} x + a_i^{(0)} \quad , x_i \leq x < x_{i+1} \tag{4.16}$$

with

$$\begin{aligned} a_i^{(2)} &= \frac{\frac{y_{i+1}-y_i}{x_{i+1}-x_i} - \frac{y_{i+2}-y_i}{x_{i+2}-x_i}}{x_{i+2} - x_{i+1}} \\ a_i^{(1)} &= \frac{y_{i+1} - y_i}{x_{i+1}} - a_i^{(2)}(x_{i+1} + x_i) \\ a_i^{(0)} &= a_i^{(2)} x_i^2 + a_i^{(1)} x_i + y_i \end{aligned}$$

cannot solve this problem either (see figure 4.16, middle).

Only by using cubic splines the resulting function becomes twice continuous differentiable. However, this takes a relatively large computational effort. A simple continuous differentiability with can be achieved a lot easier by a linear combination of tho neighbouring quadratic interpolations, as can be seen at the bottom of figure 4.16:

$$K_i(x) = \frac{a_{i-1}(x)(x_{i+1} - x) + a_i(x)(x - x_i)}{x_{i+1} - x_i}. \tag{4.17}$$

For the three dimensional interpolation the $4^3 = 64$ closest lattice points are used by first calculating 16 curves in z-direction. In the next step 4 planes are calculated from these and finally one three dimensional interpolation is formed.

The method described here is used for both the reconstruction as well as for the Monte Carlo Program.

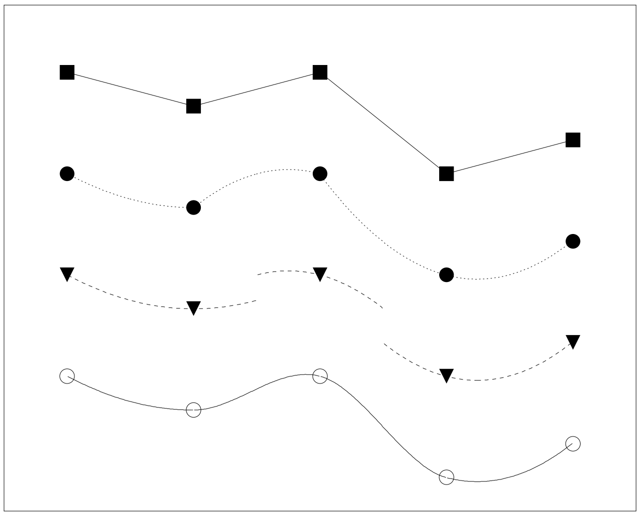

Figure 4.16: Different interpolation algorithms. From top to bottom: Linear interpolation, quadratic interpolation, quadratic interpolation with limits in the middle between the support points, linear combination.

4.8 Momentum Determination

The determination of the momentum in an inhomogeneous magnetic field is usually just as time critical as the track finding itself. Also in this respect considerable gains could be realized in HRC by using a refined look-up-table technique.

4.8.1 The Momentum Matrix

Instead of calculating the momentum for each particle individually, 500,000 electron and positron trajectories through the detector are calculated with well defined kinematics before the analysis begins. For this purpose the four parameters

1. Z-position of the vertex: z_v,
2. Scattering Angle in x : x',
3. Scattering Angle in y : y' und
4. Momentum : P

are varied on a lattice within the acceptance of the HERMES detector.

This calculation results in four matrices

1. $\Delta x'_{ijkl}$: the alteration in the angle in the x-direction in the magnetic field as a function of the indices in z_v, x', y' and P,
2. Δx_{ijkl}: the x-offset of the extension of the partial front track with respect to the back track at the center of the magnet (see chapter 4.6),
3. Δy_{ijkl}: the y-offset of the extension of the partial front track with respect to the back track at the center of the magnet (see chapter 4.6) and
4. $\Delta y'_{ijkl}$: the (small) alteration in the y-direction for the respective track.

Only the first matrix $\Delta x'_{ijkl}$ is of importance for the momentum determination. The computation of the matrices is very time consuming (DEC 3000/300lx: 18 hrs, SGI Challenger 14 CPUs 20 min, Linux i585 133 MHz 4h 20min). However, it has to be done only once per software installation and magnetic field.

A second order Runge-Kutta algorithm is used to solve the equations of motion for the particles in the magnetic field, because a magnetic field is only known as an extended quadratic interpolation. The Richardsen-extrapolation[STO78, WAN92] is used to increase the accuracy and to improve the regulation of the step width.

If the reconstruction now finds a particle whose kinematics corresponds to the described matrix, the momentum is determined with few operations to an accuracy of 0.1%. This is achieved by interpolation and by interpolating the inversion of $\Delta x'_{ijkl}$ in $P(x')$. The time consuming solution of the equations of motion can thus be avoided at the time of the reconstruction for 98% of all events.

4.8.2 Shooting Method

In the case that a track does not fit into the kinematic region of the momentum matrix, a different method must be used to determine the momentum. This is for example the case if the particle is created at a secondary vertex, outside the target.

For this purpose HRC uses the so called shooting method, where a front particle track is brought into agreement with the back track by varying the momentum.

The computation of the track in the magnetic field uses a 2nd order Runge-Kutta algorithm analogous to chapter 4.8.1.

The trajectories of two tracks $\vec{x}_0^{(1)}(t, P_0 - \frac{\Delta P}{2})$ and $\vec{x}_0^{(2)}(t, P_0 + \frac{\Delta P}{2})$, or as a function of the position variable z: $\vec{x}_0^{(1)}(z, P_0 - \frac{\Delta P}{2})$ and $\vec{x}_0^{(2)}(z, P_0 + \frac{\Delta P}{2})$ are calculated iteratively starting from the assumption of a momentum P_0 for a homogeneous magnetic field.

Newton's iteration technique to find the zeros is used by finding the minimum of

$$\vec{x}(z_H, P) - \vec{x}_H(z_H) \tag{4.18}$$

where $\vec{x}_H(z_H)$ is a point on the partial back track at $z = z_H$.

HRC now tries to connect the x-coordinate of the computed trajectory with the back track. Therefore the iteration procedure is simplified to:

$$P_{n+1} = P_n - \frac{\frac{x^{(1)}(z_H, P - \frac{\Delta P}{2}) + x^{(2)}(z_H, P + \frac{\Delta P}{2})}{2} - x_H(z_H)}{\frac{x^{(2)}(z_H, P + \frac{\Delta P}{2}) - x^{(1)}(z_H, P - \frac{\Delta P}{2})}{\Delta P}}. \tag{4.19}$$

The required accuracy of 0.2% is usually achieved after 2-3 iterations.

4.9 Track Dependant Calibration

For the finding of tracks in the spectrometer, calibration values for the decoder (HDC) are necessary. These calibrations can only be based on track independent input parameters. Further corrections have to be applied after the first momentum determination:

- The space drift time relation in the drift chambers depends on the angle of the particle track. This angle is only known after the track finding.
- The drift signal runtime in the signal wires is only known after the vertical position of the track in the detector has been determined. This results in a slightly different drift time.
- The space drift time relation also depends on the magnetic field. For this correction the intersection point of the track with the chamber must be known as well.
- Rotations of the detector or slightly bent chamber planes may also be corrected by knowledge of the interaction point.
- The track itself is bent in the vicinity of the magnetic field. This effect could be taken into account for the curvature of the track. However, the suggested method of assuming straight tracks and correcting the measurements of the chambers accordingly is more elegant and efficient. This kind of correction leads to a simpler energy measurement from the track parameters.
- The Cerenkov detector has a somewhat position dependent efficiency due to the structure of the mirror system.
- Even lightly deflected foils lead to different gains in the transition radiation detector. Therfore the intersection point of the track with the detector has to be well known.
- Hodoscope signals are attenuated on the way to the photomultiplier. The timing signal also has to be corrected with respect to the total track length and the intersection.
- The electromagnetic energy measured by the calorimeter has to be corrected for the impact angle into the lead glass.

At the time of completion of this thesis not all of these track dependant calibrations have been completed. In particular there are no sufficient measurements about the detector rotation yet. However, the interface is already implemented in the program.

After these corrections have been applied, the track parameters and the momentum are recalculated.

4.10 Vertex Reconstruction

Two kinds of vertices are of interest in the HERMES detector: The primary vertex defined by the interaction of a beam particle with a target particle and secondary vertices created by the conversion or decay of a neutral particle. A vertex can be detected by the reconstruction if at least two tracks emerge from it or if a single track comes directly from the target. HRC considers tracks belonging to a vertex if they approach the center of the vertex to within 2σ. In the following the algorithm to define the vertex is introduced and the treatment of uncertainties in the vertex definition is discussed.

4.10.1 Vertex Search

The vertex search is oriented to finding the vertices as well as the tracks that belong to them. The tracks are organised into groups.

The starting assumption of the algorithm is that all identified tracks belong to the same vertex. They are assigned to group 1.

For all N tracks in this group a point $\vec{v}$ is sought which minimizes the sum of squared distances from $\vec{v}$ to the tracks

$$\vec{x}_i(t) = \vec{s}_i + t \cdot \vec{r}_i. \tag{4.20}$$

The distance of between this point and the track is given as

$$d_i(\vec{v}) = \sqrt{(\vec{v} - \vec{s}_i)^2 - \frac{[(\vec{v} - \vec{s}_i)\vec{r}_i]^2}{\vec{r}_i^2}} \tag{4.21}$$

The extreme value condition for the sum of the squared distances

$$\vec{\nabla}_{\vec{v}} \sum_{i=1}^{N} d_i^2 = 0 \tag{4.22}$$

leads to the definition of the vertex $\vec{v}$ from

$$0 = N \cdot \vec{v} - \sum_{i=1}^{N} \vec{s}_i - \sum_{i=1}^{N} \vec{r}_i(\vec{r}_i\vec{v} - \vec{r}_i\vec{s}_i). \tag{4.23}$$

Using $\vec{n} = \frac{\vec{r}}{|\vec{r}|}$, 4.23 reduces to the the solution of a three dimensional inhomogeneous system of linear equations:

$$A\vec{v} = \vec{I}, \tag{4.24}$$

with

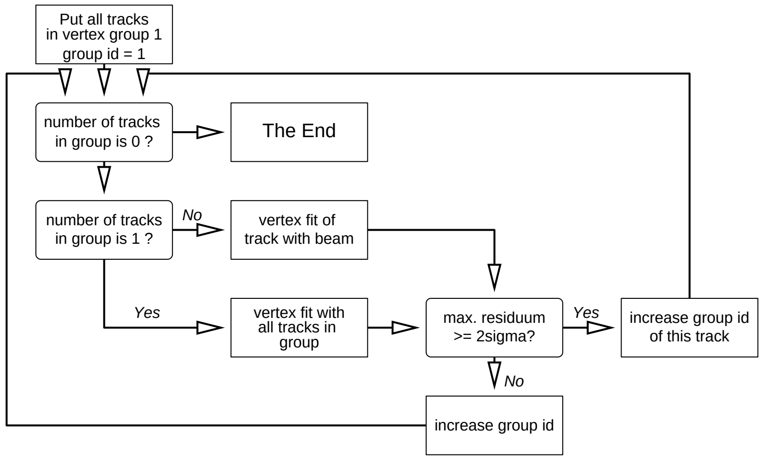

Figure 4.17: The vertex fit algorithm. In the beginning all tracks are assigned to a common vertex. Tracks with a distance of 2σ or more to the center of the vertex are removed and considered for further vertices.

$$A = N\delta_i^j - \sum_{l=1}^{N} (\vec{n}_l \otimes \vec{n}_l)_i^j \quad \text{and} \tag{4.25}$$

$$\vec{I} = \sum_{l=1}^{N} [\vec{s}_l - \vec{n}_l(\vec{s}_l\vec{n}_l)]. \tag{4.26}$$

Here $\vec{a} \otimes \vec{b}$ is the tensor product of two vectors.

$$(\vec{a} \otimes \vec{b})_{ij} = a_i \cdot b_j. \tag{4.27}$$

If the track lies outside of 2σ from the vertex (see chapter 4.10.2), it is assigned to a new group and the vertex fit according to 4.24 is repeated for all remaining tracks. If all tracks within one group lie within the 2σ limit around the vertex, the procedure is repeated with the next group of tracks.

If a group consist of exactly one track, it is assumed that the vertex position is within the positron beam and a fit according to equation 4.24 is executed with this track and the positron beam. Figure 4.17 illustrates this algorithm.

4.10.2 Error Propagation of the Vertex Reconstruction

The calculation of the uncertainty from the track covariance matrices is based on a paper by Oleg Grebeniuk[GRE95]:

The error propagation for equation (4.24) is rather complex, because the calculation of $\vec{v}$ is nonlinear in the track parameters, resp. covariances, of the different tracks.

Starting from (4.24) the variation in $\vec{v}$ may be expressed as

$$\delta\vec{v} = A^{-1}(\delta\vec{I} - \delta A\vec{v}) \tag{4.28}$$

The total variation can also be expressed as a sum over the variations for the single tracks:

$$\delta\vec{v} = \sum_l \delta\vec{v}_l. \tag{4.29}$$

After a few steps $\delta\vec{v}_l$ is derived as

$$\delta\vec{v}_l = M_l\delta\vec{X}_l. \tag{4.30}$$

where $\delta\vec{X}_l$ is the variation of the track parameters

$$\delta\vec{X}_l = \begin{pmatrix} \delta x_l \\ \delta y_l \\ 0 \\ \delta x'_l \\ \delta y'_l \\ 0 \end{pmatrix}. \tag{4.31}$$

The 3×6 matrix M_l is composed of two 3×3 matrices

$$T_l = (B - B\vec{n}_l \otimes \vec{n}_l) \tag{4.32}$$

where $B = A^{-1}$ represents the influence of the position parameters and

$$T'_l = \left(\frac{(\vec{v} - \vec{s}_l)\vec{n}_l B + (B\vec{n}_l) \otimes (\vec{v} - \vec{s}_l - 2[(\vec{v} - \vec{s}_l)\vec{n}_l]\vec{n}_l)}{|\vec{r}_l|}\right) \tag{4.33}$$

represents the influence of the track slopes. The two matrices $T_l, T'_l$are combined to M_l:

$$M_l = (T_l|T'_l) \tag{4.34}$$

As there is no contribution to the total uncertainty from the z or z' component in the following the reduced 3×4 matrix R_l will be used.

The covariance matrix of the vertex as defined by 4.24 follows from 4.29 and 4.30 to

$$C_{\vec{v}} = \sum_l R_l C_l R_l^\top \tag{4.35}$$

with C_l as in equation4.6.

Hence, the distance between track and vertex may be expressed in the metric of the covariance matrix, so that the condition of a 2σ distance for a track to belong to a vertex can be expressed as

$$d_l^2 = ||\vec{v} - \vec{s}_l||^2 - \frac{(\vec{v} - \vec{s}_l, \vec{n}_l)^2}{||\vec{n}_l||^2} \leq 2 \tag{4.36}$$

(with $(\vec{a}, \vec{c}) = \vec{a}C_{\vec{v}}^{-1}\vec{c}$ resp. $||a|| = \vec{a}C_{\vec{v}}^{-1}\vec{a}$).

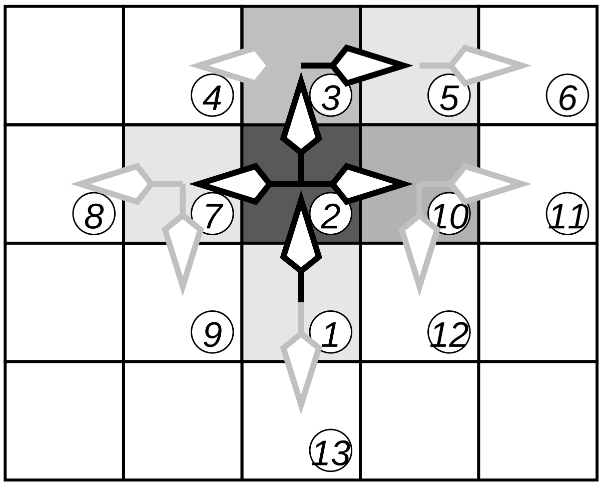

Figure 4.18: Recursive cluster search in adjacent cells. Starting from any cell (marked as 1) the adjacent cells are searched recursively one after the other. The order corresponds to the numbering of the cells.

4.11 Cluster Search in the Calorimeter

Clusters in the calorimeter develop as a result of showers from high energy particles. Not only the block that was hit responds, but some or all of the adjacent blocks as well. Cluster widths of $\sigma_{cl} \approx 4.5$ cm have been measured in test beams at DESY and CERN, in agreement with Monte Carlo studies. This means that if a particle hits the center of a block at the most the neighbouring cells contain a significant amount of the cluster energy.

It is easy to determine the calorimeter energy of charged particles: The back track is extended towards the calorimeter and the energy in the calorimeter cells around the point of incidence is added up. However, this procedure offers neither a position correlation of track and cluster, nor can it relay information about clusters from neutral particles (e.g. photons).

HRC includes two cluster search algorithms which will be introduced in the following paragraphs.

Recursive Search in Adjacent Cells This procedure starts at any cell that has registered a hit. Starting from here, first the upper, the right, the lower and the left adjacent cells are searched for hits. If necessary the search is continued with the new neighbouring cells. Blocks that have been tested are not checked again (see figure 4.18).

In this way connected cells with hits are found and combined into clusters. The

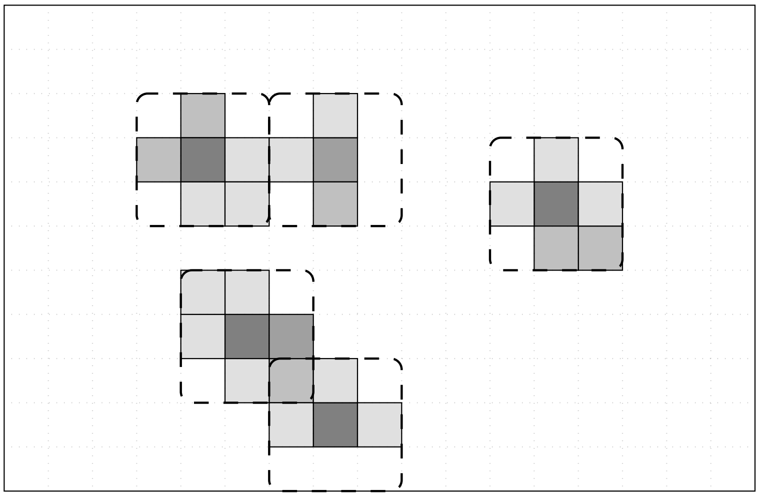

Figure 4.19: Cluster search for energy maxima in rows and columns. Cells that represent a maximum both in their row and column are marked as cluster center.

cluster energy is determined by summing over the cells of the cluster

$$E_{cl} = \sum_i E_i, \tag{4.37}$$

and the center of gravity of the cluster is defined as

$$\begin{pmatrix} x_{cl} \\ y_{cl} \end{pmatrix} = \frac{1}{\sum_i \sqrt{E_i}} \sum_i \sqrt{E_i} \begin{pmatrix} x_i \\ y_i \end{pmatrix} \tag{4.38}$$

where x_i and y_i are the centers of the respective cells.

Unfortunately the drawback of this procedure is that the connected clusters cannot be separated and that even center and energy of them are falsified. Therefore a different method is usually applied:

Search for Local Energy Maxima This method is based on finding the local energy maxima in the calorimeter plane. The 3x3 surrounding cells are called a 'cluster' in this case.

The energy and the center of the found clusters are determined according to (4.37) and (4.38). Overlap between clusters ($C^{(1)}$ and $C^{(2)}$) is taken into account by distributing the energy between them according to the ratio of the sums of non-overlapping cells from both clusters:

$$E^{(1)} = \sum_{i \in C^{(1)} \cap / C^{(2)}} E_i \left(1 + \sum_{i \in C^{(1)} \cap C^{(2)}} E_i \; / \sum_{i \in C^{(1)} \cup C^{(2)}} E_i \right), \tag{4.39}$$

$$E^{(2)} \quad = \quad \sum_{i \in C^{(2)} \cap / C^{(1)}} E_i \left(1 + \sum_{i \in C^{(1)} \cap C^{(2)}} E_i \;/\; \sum_{i \in C^{(1)} \cup C^{(2)}} E_i \right). \qquad (4.40)$$

4.11.1 Track – Cluster Correlation

As described previously, the track parameters from the back region of the detector can be correlated with the calorimeter. HRC first identifies the closest cluster to a given point of incidence and assigns this cluster to the track if the incidence point of the track is within $2\sigma_{cl}$ of the center of the cluster.

Many of the scattered particles lose a part of their energy in the form of bremsstrahlung as a result of multiple scattering in the detector material, especially the target cell and the exit window. As a result another cluster from the bremsstrahlung photons may be found where the extension of the front track meets the calorimeter.

For low energy particles (<10 GeV) particle clusters and bremsstrahlung clusters may be separated because of the strong bending of the track inside the magnet. At higher energies both clusters lie closely together.

To avoid a different treatment of high and low energy particles, the energies of both clusters, should be added as an option for the analysis, if they can be separated.

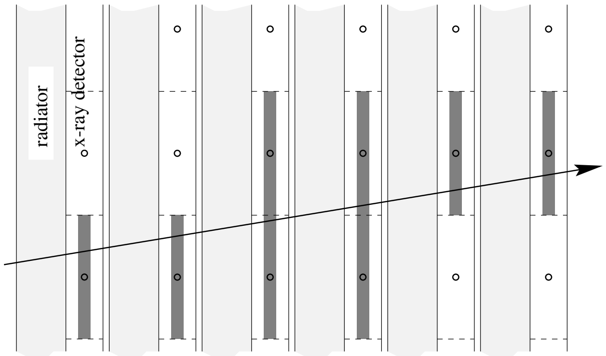

Figure 4.20: Assignment of TRD cells to a track. At the cell borders possible overlap is taken into account.

4.12 Particle Identification

The particle identification uses the Cerenkov counter, the transition radiation detector, the preshower and the lead glass calorimeter to determine probabilities for the particle type. It is mainly based on program extensions by B. Bray.

Charge and momentum of every track are known from the track reconstruction. Additionally the track parameters can be used to determine the components of the particle identification detectors, in which signals from the track are expected. The track cluster correlation combines the calorimeter signal with a track.

4.12.1 Preparation of the Identification

The Transition Radiation Detector

In the transition radiation detector the measured energy values in the detector along the particle track are summed up. The detector cells are assigned to a track if the track passes through it or if it approaches the cell to within 10% of the cell width (see figure 4.20).

The six energy values that are found in this way are averaged to a truncated mean:

$$E_{\mathrm{trd}} = \frac{1}{5}\left(\sum_{i=1}^{6} E_i - \max_{i=1\ldots 6} E_i\right), \tag{4.41}$$

to exclude possible hits from correlated δ electrons from the mean value.

If two tracks cross in one or more cells, the energy values from these cells are divided between both tracks according to the ratio of the energy deposits in the cells which are not shared by both tracks.

The Preshower

The light signal, that is created in the scintillator material of the preshower when a particle crosses it, is attenuated on the way Δy to the photomultiplier according to:

$$I_{\mathrm{mess}} = e^{-\frac{\Delta y}{\lambda}} I_0 \tag{4.42}$$

with an attenuation length λ, so that the signal must be corrected following

$$I_{\mathrm{real}} = I_{\mathrm{mess}} e^{\frac{\Delta y}{\lambda}} . \tag{4.43}$$

Equation (4.42) is only valid under certain conditions. The signal for tracks close to the beam pipe (and thus far away from the photomultiplier) is amplified as a result of the reflection at the scintillator surface.

A better correction follows empirically from

$$I_{\mathrm{real}} = I_{\mathrm{mess}} \frac{a}{(a + b\Delta y^2) e^{-\frac{\Delta y}{c}}} \tag{4.44}$$

with the fit parameters a, b and c.

Measurements at Caltech[BRA95I] result in a correction that is illustrated in figure 4.21.

If two tracks cross the same preshower element this is registered for further analysis.

The Cerenkov Counter

In the Cerenkov counter those elements are determined that are expected to see photons from the Cerenkov cone of the track. The signals from these elements are summed up and assigned to the track. Overlap with the expected regions of other tracks is registered for further analysis.

4.12.2 Identification with Hard Cuts

This relatively simple procedure tests whether signals from the particle identification detectors lie within a region that is typical for a particular type of particle. Only pions and positrons/electrons are identified. The different particle fluxes, that is their frequency in the detector, cannot be taken into account.

An electron has been identified if

$$\begin{array}{rcccl} & R^e_{\mathrm{cal},1} & \leq & \frac{E_{\mathrm{cal}}}{P} & \leq & R^e_{\mathrm{cal},2} \\ \wedge & R^e_{\mathrm{pre},1} & \leq & R'_{\mathrm{pre}} & \leq & R^e_{\mathrm{pre},2} \\ \wedge & C^e_{\mathrm{trd},1} & \leq & E_{\mathrm{trd}} & & \\ \wedge & C_{\mathrm{cer},1} & \leq & E_{\mathrm{cer}} & & . \end{array} \tag{4.45}$$

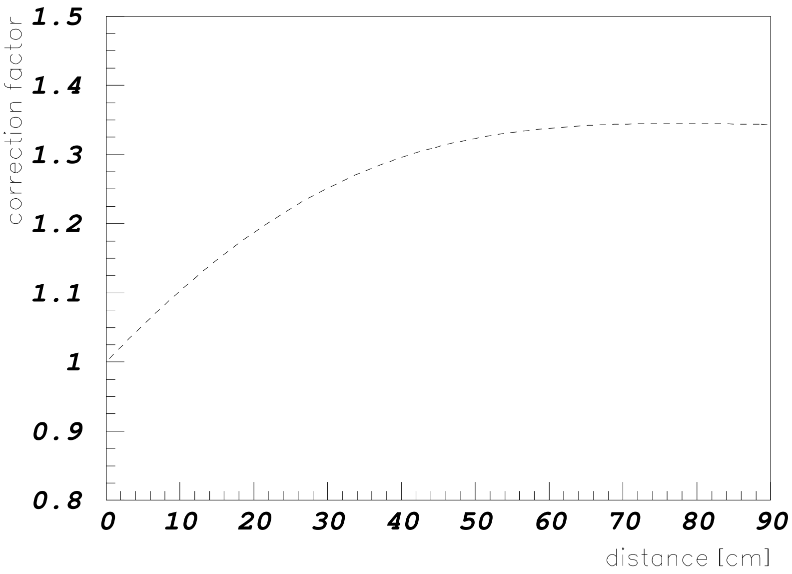

Figure 4.21: Correction factor for the attenuation of the preshower signal as a function of the pathlength inside the scintillator.

R'_{pre} is a ratio of preshower signal and particle momentum that has been normalized for the electron or positron momentum. It is on average

$$\left\langle R'_{\text{pre}} \right\rangle = 1 \tag{4.46}$$

if the detected particle is an electron or a positron, while R'_{pre} is smaller for hadrons. For the first analysis the following hard cuts were used for the momentum ratios ($R^e_{\text{cal},1}$, $R^e_{\text{cal},2}$, $R^e_{\text{pre},1}$, $R^e_{\text{pre},2}$) and signal heights ($C^e_{\text{trd},1}$, $C_{\text{cer},1}$):

$$\begin{array}{rcccc} & 0.8 & \leq & \frac{E_{\text{cal}}}{P} & \leq & 2.0 \\ \wedge & 0.5 & \leq & R'_{\text{pre}} & \leq & 2.0 \\ \wedge & 8000\text{ADC}-\text{channels} & \leq & E_{\text{trd}} & & \\ \wedge & 0.1\text{photons} & \leq & E_{\text{cer}} & & . \end{array} \tag{4.47}$$

Similar conditions are valid for the detection of a hadron:

$$\begin{array}{lrcccl} & & & E_{\mathrm{cal}} & \leq & C^{\pi}_{\mathrm{cal},2} \\ \wedge & & & \frac{E_{\mathrm{cal}}}{P} & \leq & R^{\pi}_{\mathrm{cal},2} \\ \wedge & C^{\pi}_{\mathrm{pre},1} & \leq & E_{\mathrm{pre}} & \leq & C^{\pi}_{\mathrm{pre},2} \\ \wedge & & & E_{\mathrm{trd}} & \leq & C^{\pi}_{\mathrm{trd},2} \\ \wedge & C_{\mathrm{cer},1} & \leq & E_{\mathrm{cer}} & & . \end{array} \tag{4.48}$$

The applied hard cuts have to be optimized by Monte Carlo studies and by tests with real data. For the pion identification it is problematic that low energy pions ($P < 6$ GeV) do not give a Cerenkov signal, so that pions cannot be separated from other hadrons (mainly kaons and protons) in this momentum region. This 6 GeV threshold for pions can be lowered by using a different gas than the nitrogen that was used in 1995.

4.12.3 Identification by the Probability Product

As in the identification by hard cuts (chapter 4.12.2) the particle identification using the probability product has until now only been applied to the electron/pion separation.

The basic principle of the identification method assigns a weighted probability ($\mathcal{L}_{\mathrm{D}}^{\pi/e}$) to every particle type (π, e) for each detector. This weighted probability is derived from the detector response for a given particle type, kinematic and particle flux. The flux is the probability of finding such a particle in this kinematic region.

The unweighted probability of finding a specific particle in a single detector D can be calculated as:

$$\mathcal{P}_D^e = \frac{\mathcal{L}_D^e}{\mathcal{L}_D^e + \mathcal{L}_D^\pi}, \tag{4.49}$$

$$\mathcal{P}_D^\pi = \frac{\mathcal{L}_D^\pi}{\mathcal{L}_D^e + \mathcal{L}_D^\pi}. \tag{4.50}$$

This method can of course be extended to multiple particle types, but until now not enough calibration data are available for the hadronic separation:

$$\mathcal{P}_D^\imath = \frac{\mathcal{L}_D^\imath}{\sum_\jmath \mathcal{L}_D^\jmath}. \tag{4.51}$$

The weighted total probability from all particle identification detectors is found as the product of the weighted single detector probabilities:

$$\mathcal{L}^\imath = \prod_D \mathcal{L}_D^\imath. \tag{4.52}$$

The unweighted total probability follows from

$$\mathcal{P}^i = \frac{\mathcal{L}^i}{\sum_j \mathcal{L}^j}. \tag{4.53}$$

In the following the determination of the single detector probabilities in the four particle identification detectors will be discussed.

4.12.4 The Preshower

In the calculation of the preshower probabilities an asymmetric Gaussian is used to model the expected detector response:

$$\mathcal{A}(x, \bar{x}, \sigma_l, \sigma_r) = \begin{cases} e^{-\frac{(x-\bar{x})^2}{\sigma_l}} & \text{for } x < \bar{x} \\ e^{-\frac{(x-\bar{x})^2}{\sigma_r}} & \text{for } x \geq \bar{x}. \end{cases} \tag{4.54}$$

Input parameters for the calculation of the probabilities are the particle momentum P, the preshower energy E_{pre} and the preshower momentum ratio R'_{pre} from equation (4.46).

The weighted probabilities are then given as

$$\mathcal{L}^e_{\text{pre}} = c_e \mathcal{A}(R'_{\text{pre}}, R_m, \sigma_{Rl}, \sigma_{Rr}), \tag{4.55}$$

$$\mathcal{L}^\pi_{\text{pre}} = c_\pi \mathcal{A}(E_{\text{pre}}, E_m, \sigma_{El}, \sigma_{Er}) \tag{4.56}$$

which makes use of the fact that electrons produce a momentum dependent signal, while the hadron signal is practically momentum independent. The constants $c_e, c_\pi, R_m, \sigma_{Rl}, \sigma_{Rr}, E_m, \sigma_{El}$, and σ_{Er} must be optimized by Monte Carlo studies and by fits to the real data.

4.12.5 The Calorimeter

The probability that the calorimeter has detected an electron depends on the momentum of the particle and the measured energy value of the cluster that the track points at. The calorimeter is calibrated for electromagnetic energy, so that for an electron/positron it should on average be found that $\left\langle \frac{E_{\text{cal}}}{P} \right\rangle = 1$. The variance follows from the uncertainty in the spectrometer resolution (see 5.3) and from the energy resolution of the calorimeter

$$\Delta E_{\text{cal}} = c_0 + \frac{c_1}{\sqrt{P}} \tag{4.57}$$

with

$$\Delta E = \sqrt{\Delta E_{\mathrm{cal}}^2 + \Delta P_{spek}^2} \tag{4.58}$$

to

$$\mathcal{L}_{\mathrm{cal}}^e = \frac{1}{2\pi} e^{-\frac{1}{2}\frac{(E_{\mathrm{cal}}-P)^2}{(P\Delta E)^2}}. \tag{4.59}$$

In reality also bremsstrahlung from external and internal processes is collected in the calorimeter cluster. For the case of $E_{\mathrm{cal}} > P$ an additional correction has to be applied.

For pions it is found that

$$\mathcal{L}_{\mathrm{cal}}^\pi = \begin{cases} c_\pi e^{-c_\pi(\frac{E_{\mathrm{cal}}}{P} - \frac{c_{tr})}{P}} & \text{for } P > c_{tr} \\ c_\pi & \text{for } P \leq c_{tr}, \end{cases} \tag{4.60}$$

where c_{tr} is the trigger threshold of the calorimeter (now at 3.5 GeV). Below this threshold the weighted probability to good approximation can be taken as a constant, because in this region the pion flux strongly dominates the positrons. The remaining constants again are derived from the data.

4.12.6 The Transition Radiation Detector

Extensive Monte Carlo studies have been carried out for the transition radiation detector[EME95]. They resulted in a two dimensional table for each particle type and detector plane with the weighted probabilities as a function of particle energy, track angle and detector response.

From this table the probabilities for a particular particle are obtained by quadratic interpolation. Following (4.52) these weighted probabilities can be combined to a total detector probability.

A different method uses the truncated mean values as in (4.41) to extract total detector probabilities from a different table.

4.12.7 The Cerenkov Counter

In the analysis of the Cerenkov counter the expected number of photoelectrons in the detector is determined from the measured momentum for each mass hypothesis as a function of $\beta^\imath = \frac{P}{\sqrt{(m_0^\imath)^2+P^2}}$:

$$n_\gamma^\imath = \begin{cases} 2.9\frac{1-\left(\frac{\beta_{tr}}{\beta^\imath}\right)^2}{1-\beta_{tr}^2} & \text{for } \beta^\imath \geq \beta_{tr} \\ 0 & \text{otherwise} \end{cases} \tag{4.61}$$

The parameter β_{tr} depends on the Cerenkov gas and represents the threshold for the emission of Cerenkov photons.

From $n_\gamma^\imath$ follows a Poisson distribution $\Pi^\imath(i, n_\gamma^\imath)$ for the expected number of photons.

The number of measured photons x_γ is smeared by the detector resolution for i emitted photons $\sigma_{\text{cer}}(i)$, so that the total probability follows from

$$\mathcal{L}_{\text{cer}}^\imath = \sum_i \Pi^\imath(i, n_\gamma^\imath) \frac{1}{2\pi\sigma_{\text{cer}}(i)} e^{-\frac{(x_\gamma - i)^2}{2\sigma_{\text{cer}}(i)^2}}. \tag{4.62}$$

Chapter 5

Testing the Reconstruction

5.1 The Hermes Monte Carlo Program

The HERMES Monte Carlo program (HMC) was, as the first part of the HERMES offline software, already available in the early planning phase of the experiment. It was used mainly for background studies, acceptance calculations, development of the reconstruction, calculations of the detector response and naturally also to test the reconstruction and analysis software. The first version and the design of the program were developed by M. Düren. Since then a number of authors have changed and extended the program.

HMC is based on GEANT3[SJO94], but includes considerable extensions and improvements. These relate to the geometry and material definitions which are entirely externally configurable, so that HMC can be adapted to any detector geometry without substantial modifications. Particular emphasis was put on a correct detector simulation and the GEANT event display was enhanced by a complex display of the HERMES detector components. HMC includes a multitude of different internal physics generators. The expected kinematics for scattered positrons are simulated through the cross sections for the unpolarized and polarized structure functions $F_2(x, Q^2)$, $R(x, Q^2)$ and $g_1(x)$ that are known from earlier measurements, including radiative corrections. PEPSI(Polarized Electron Proton Scattering Interactions)[VEL91, IHS95I] is based on LEPTO and calculates the hadronic final states from polarized leptoproduction. Generators for Møller- and Bhabha-scattering, photo production and interfaces for external generators are included as well.

A good Monte Carlo program is indispensable for realistic tests of the reconstruction software. The closer to reality the generated data are, the more confidence can be placed in the reliability, accuracy and efficiency of the analysis. HMC is particularly designed for this purpose, so that even the output of the program essentially agrees with the output of the decoder for the real data.

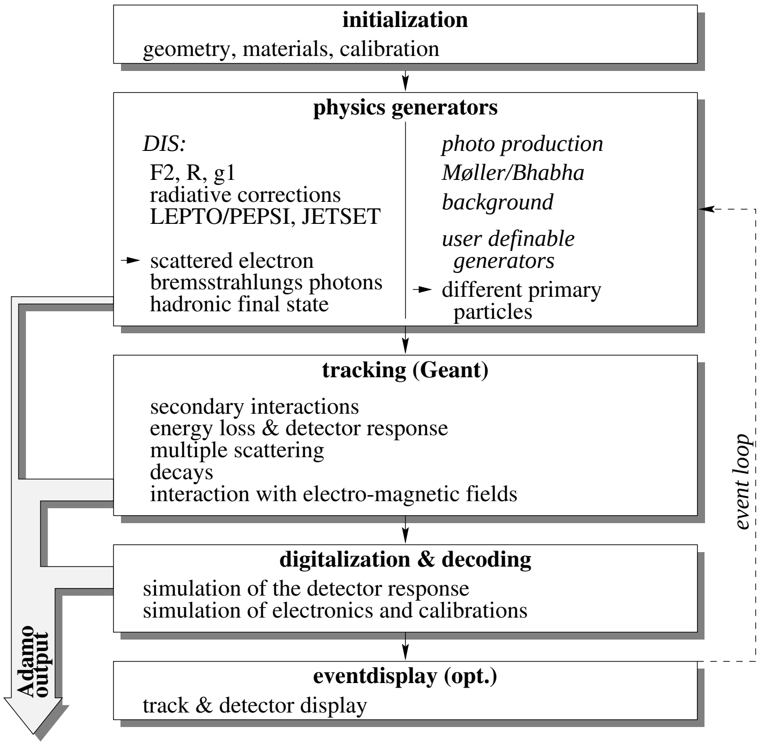

Figure 5.1: Simplified flow chart for the HERMES Monte Carlo program HMC. After the initialization the event simulation happens in the essential program modules generation, tracking and digitization. Output in ADAMO format are forwarded for tests to the analysis or the reconstruction.

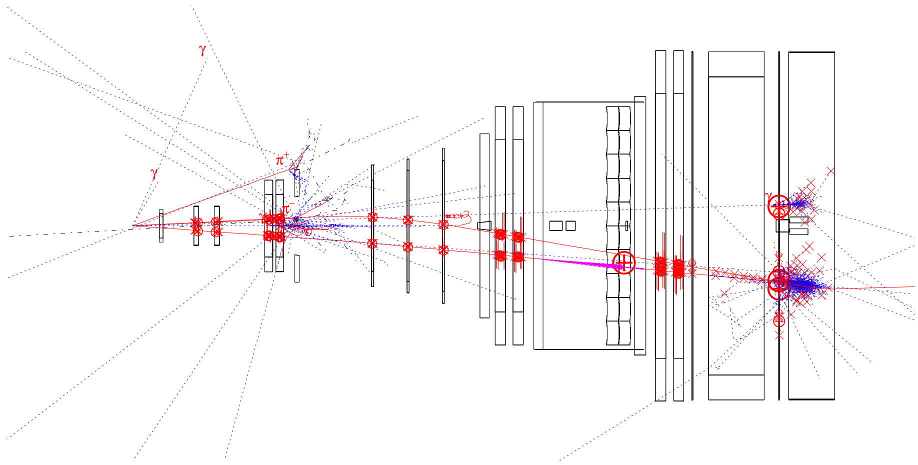

Figure 5.2: A HMC generated deep inelastic event in the x-z projection.

A very useful program element is the introduction of so called 'Düren-particles', special GEANT particles, that do not interact with matter, but with (macroscopic) electromagnetic fields. In this way, effects like multiple scattering and energy losses can be treated separately from the actual reconstruction. This allows direct measurements of the energy and angle resolution of the pure tracking algorithm.

5.2 Reconstruction Efficiency

Of special importance for the determination of the quality of the reconstruction program is the reconstruction efficiency, which is the probability that a track is recognized by the reconstruction program. On closer inspection a multitude of different definitions can be given for this efficiency, all of which cover different qualitative aspects.

- The simples definition is

$$\epsilon_0 = \frac{\text{Number of found tracks}}{\text{Number of actual tracks}}. \tag{5.1}$$

  It's meaning is limited, due to the fact that the tracks are not tested for authenticity, so that ghost tracks may incorrectly appear to increase the quality of the reconstruction.

- This can be taken into account through the following definition:

$$\epsilon_1 = \frac{\text{Number of correct found tracks}}{\text{Number of actual tracks}}. \tag{5.2}$$

- Or to assign more weight to the detection of ghost tracks

$$\epsilon_2 = \frac{\text{Number of correct found tracks} - \text{Number of ghost tracks}}{\text{Number of actual tracks}}, \tag{5.3}$$

  where this efficiency may even reach negative values.

Additionally a number of influences on the efficiency have to be considered. Starting with the kinematic parameters of a track over the particle type to the multiplicity of an event and of course the type of event itself, correlations can be found and if possible eliminated.

In the following first the dependencies of Monte Carlo data and real data on several reconstruction parameters will be examined and optimized, before the the different influences will be discussed in detail.

5.2.1 Efficiency Tests with Monte Carlo Data

Monte Carlo data are particularly suited for efficiency studies, because it is only with them that the number and kinematics of the particles that are to be reconstructed are exactly known.

Response probabilities of 92.11% for the front chambers and 93.65% for the back chambers were assumed. First the dependence of the efficiency on the track finding parameters in HRC according to equation (5.2) is examined.

The conditions that determine the maximally allowed number of missing hits for a track have the largest influence on the efficiency. If the response probability of a drift chamber (δ) is known, the theoretical reconstruction efficiency may be determined.

If for example it is required that in no projection track in the back detector region with $N = 4 \cdot 2$ planes a hit may be missing, the projection efficiency follows to

$$\pi_0 = (\delta)^N \tag{5.4}$$

or for exactly M $(M < N)$ missing hits the general binomial distribution

$$\pi_M = \begin{pmatrix} N \\ M \end{pmatrix} (\delta)^{(N-M)}(1-\delta)^M. \tag{5.5}$$

If maximal p missing hits per projection and t missing hits per track are allowed, the reconstruction efficiency $\epsilon_{p/t}$ follows as a combination of the projection efficiencies:

$$\epsilon_{0/0} = \begin{pmatrix} 0 \\ 0 \end{pmatrix} (\pi_0)^3 \tag{5.6}$$

$$\epsilon_{1/1} = \epsilon_{0/0} + \begin{pmatrix} 3 \\ 1 \end{pmatrix} \pi_1 (\pi_0)^2 \tag{5.7}$$

$$\epsilon_{1/2} = \epsilon_{1/1} + \begin{pmatrix} 3 \\ 2 \end{pmatrix} (\pi_1)^2 \pi_0 \tag{5.8}$$

$$\epsilon_{1/3} = \epsilon_{1/2} + \begin{pmatrix} 3 \\ 3 \end{pmatrix} (\pi_1)^3 \tag{5.9}$$

$$\epsilon_{2/2} = \epsilon_{1/2} + \begin{pmatrix} 3 \\ 1 \end{pmatrix} \pi_2 (\pi_0)^2 \tag{5.10}$$

$$\epsilon_{2/3} = \epsilon_{1/3} + \begin{pmatrix} 3 \\ 1 \end{pmatrix} \pi_2 (\pi_0)^2 + 3!\ \pi_2 \pi_1 \pi_0 \tag{5.11}$$

$$\begin{aligned}
\epsilon_{2/4} &= \epsilon_{2/3} + \begin{pmatrix} 3 \\ 2 \end{pmatrix} (\pi_2)^2 \pi_0 + \begin{pmatrix} 3 \\ 1 \end{pmatrix} \pi_2(\pi_1^2) && (5.12)\\
\epsilon_{2/5} &= \epsilon_{2/4} + \begin{pmatrix} 3 \\ 2 \end{pmatrix} (\pi_2)^2 \pi_1 && (5.13)\\
\epsilon_{2/6} &= \epsilon_{2/5} + \begin{pmatrix} 3 \\ 3 \end{pmatrix} (\pi_2)^3 && (5.14)\\
\epsilon_{3/3} &= \epsilon_{2/3} + \begin{pmatrix} 3 \\ 1 \end{pmatrix} \pi_3(\pi_0)^2 && (5.15)\\
\epsilon_{3/4} &= \epsilon_{2/4} + \begin{pmatrix} 3 \\ 1 \end{pmatrix} \pi_3(\pi_0)^2 + 3!\ \pi_3\pi_1\pi_0 && (5.16)\\
\epsilon_{3/5} &= \epsilon_{2/5} + \begin{pmatrix} 3 \\ 1 \end{pmatrix} \pi_3(\pi_0)^2 + 3!\ \pi_3\pi_1\pi_0 + \\
&\quad \begin{pmatrix} 3 \\ 1 \end{pmatrix} \pi_3(\pi_1)^2 + 3!\ \pi_3\pi_2\pi_0 && (5.17)\\
\epsilon_{3/6} &= \epsilon_{2/6} + \begin{pmatrix} 3 \\ 1 \end{pmatrix} \pi_3(\pi_0)^2 + 3!\ \pi_3\pi_1\pi_0 + \begin{pmatrix} 3 \\ 1 \end{pmatrix} \pi_3(\pi_1)^2 + \\
&\quad 3!\ \pi_3\pi_2\pi_0 + \begin{pmatrix} 3 \\ 2 \end{pmatrix} (\pi_3)^2\pi_0 + 3!\ \pi_3\pi_2\pi_1 && (5.18)\\
\epsilon_{3/7} &= \epsilon_{3/6} + \begin{pmatrix} 3 \\ 2 \end{pmatrix} (\pi_3)^2 \pi_1 + \begin{pmatrix} 3 \\ 1 \end{pmatrix} \pi_3(\pi_2)^2 && (5.19)\\
\epsilon_{3/8} &= \epsilon_{3/7} + \begin{pmatrix} 3 \\ 2 \end{pmatrix} (\pi_3)^2 \pi_2 && (5.20)\\
\epsilon_{3/9} &= \epsilon_{3/8} + \begin{pmatrix} 3 \\ 3 \end{pmatrix} (\pi_3)^3 && (5.21)\\
\ldots
\end{aligned}$$

The probabilities for weaker conditions can be calculated analogously.

Because HRC always combines two detector planes to one point in the bit pattern, the above formulae are only valid in the event that treesearch tolerates a missing point. In case 100% agreement is required, π_2 is given as:

$$\pi_2^{(100)} = \left(\begin{pmatrix} N \\ 2 \end{pmatrix} - 4 \right) (\delta)^{N-2}(1-\delta)^2, \tag{5.22}$$

because 4 permutations are omitted, where both missing hits fall into exactly one detector module (BC1, BC2, BC3, BC4). Equation (5.5) is only valid for 75% agreement in the pattern recognition through the treesearch algorithm.

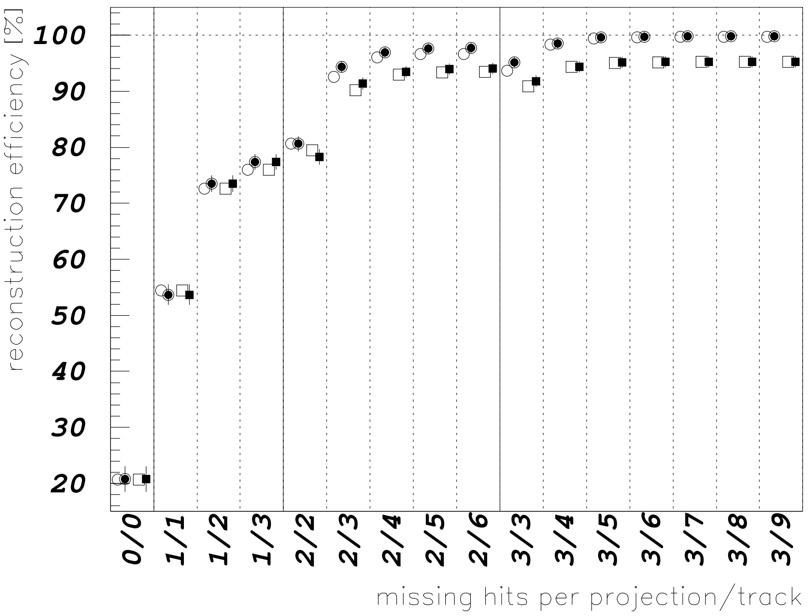

Figure 5.3: Reconstruction efficiency in the back chambers from Monte Carlo data. For different restrictions concerning the number of missing hits per track projection / per track, theoretical (empty) and measured reconstruction data (full symbols with error bars) are shown. The circles (◯) correspond to the values for 75% treesearch agreement, the squares (□) correspond to the values for 100% agreement.

Figure 5.3 shows the efficiency for different conditions on the allowed number of missing hits theoretically as well as a result from reconstructed Monte Carlo data. The good agreement of expected and found reconstruction efficiency confirms the sound operation of Monte Carlo and reconstruction software.

According to the equations (5.6)-(5.21) the theoretical reconstruction efficiencies for the front and back detectors may also be determined as a function of the chamber efficiencies (see figure 5.4). The reconstruction efficiency for the back chambers is very high, even for a large number of allowed missing hits. It is possible to put such low requirements on the number of hits per track in the back chambers due to the high redundancy of the system (8 chambers per wire orientation). On the other hand, in the front chambers already 2 missing hits per projection lead to a significant contribution of ghost tracks.

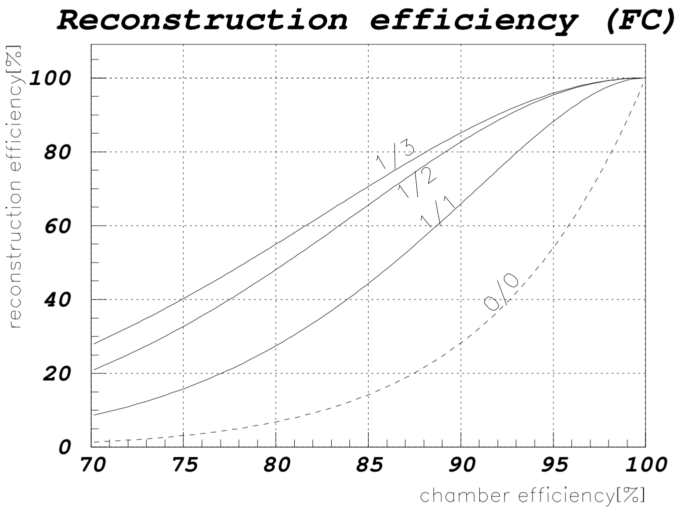

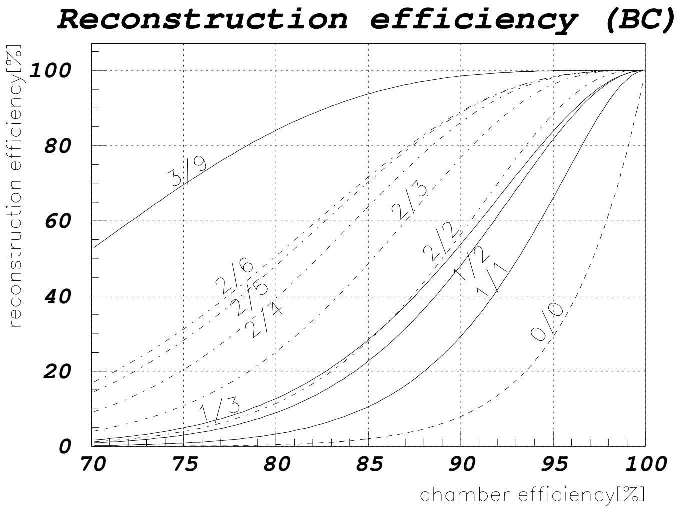

Figure 5.4: Reconstruction efficiency as a function of single chambers efficiencies in the front (top) and back (bottom) detector region. The different curves correspond to the different requirements on the maximally allowed number of missing hits per projection / track.

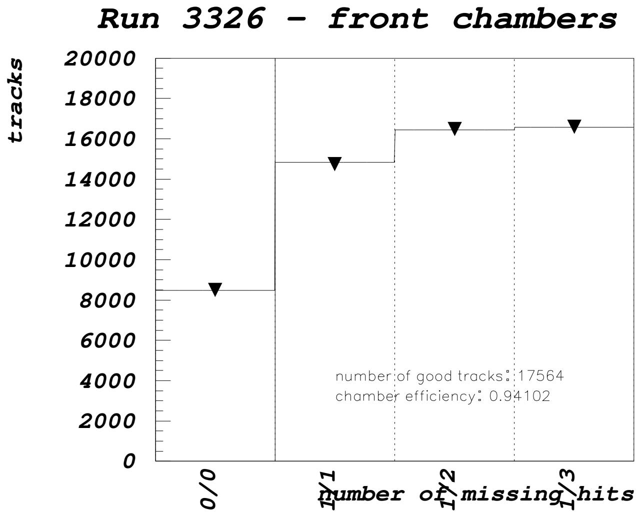

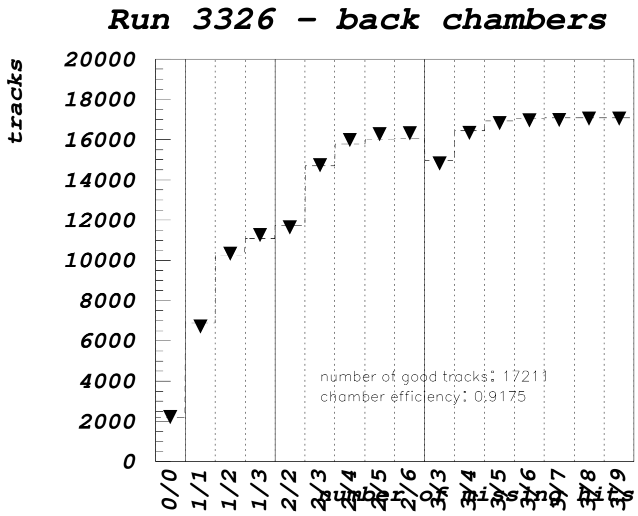

Figure 5.5: Efficiency test with real data. The number of tracks in the front and back drift chambers was determined for different requirements on the track quality (allowed number of missing hits per projection/track). An optimization algorithm used with the equations (5.6) to (5.21) gives the shown average chamber efficiency. The shape of the curve otherwise fulfills the expectations.

5.2.2 Efficiency Test with Real Data

As previously mentioned, tests of the reconstruction efficiency are hardly possible with real data. The raw data are strongly contaminated by background, so that good events cannot be filtered out. Hence, no ratio of reconstructed and good events can be determined.

However, the existing reconstruction program offers different qualities of reconstruction by changing the parameters. By varying the number of maximal allowed missing hits the chamber efficiency can be calculated with an optimization algorithm. As this optimization problem is overdetermined (only two parameters, the mean chamber efficiency and the number of good tracks, are determined) the dependence of the efficiency on the reconstruction parameters can be compared to theoretical expectations. This allows the testing of the method (see figure 5.5).

Additionally to this test of the software, this method probably gives the most reliable result for the total reconstruction efficiency and the usable response probability of the chamber. In general for the response probability only the existence of a signal in the respective cell is checked. The usable response probability also tests, whether the drift time, that is the position measurement, of the responding wire is reasonable and can be used for the track reconstruction.

5.3 Momentum and Angular Resolution

The momentum and the angular resolution of the spectrometer determine the resolution for all kinematic variables of the detected particles (see equations (2.2) – (2.4)).

There are several factors that influence the angle and momentum measurement:

1. Multiple scattering of the particles in the detector and target material.
2. The finite position resolution of the detectors.
3. Errors in the calibrations, i.e. wrong interpretation of the measured data.
4. Alignment errors, i.e. uncertainties in the construction or the surveying of the detectors.
5. Consciously accepted uncertainties to increase the speed of the software.
6. Numerical errors in the calculation of the track parameters.
7. Software errors.

The size of the respective errors should decrease from the top to the bottom of the list.

Software Errors

Extensive tests have been carried out, to find software errors that can never be entirely excluded in large programming packages and to ensure that they do not influence the results of the program.

Unfortunately, software errors are hard to find. Under lucky circumstances they lead to a crash of the program, under less fortunate circumstances they only induce small systematic errors that lead to a wrong total result. As an example consider the trajectory of a charged particle in a magnetic field; Many experiments use a linear interpolation of the support points for the parametrisation of the magnetic field. On the other hand the GEANT module for the calculation of the trajectory uses a 4th order Runge-Kutta method. In applying a 4th order differential equation method, which allows for a large step width, wrong results emerge because the linear interpolation used for the parametrisation of the magnetic vector field is not four times continuous differentiable (compare[STO78]).

Such an error cannot be found under normal circumstances, first because the effect is small and second because the wrong results are consistent for Monte Carlo and the reconstruction. This can be avoided by using two independent differential equation methods as it was done in the HERMES software.

Frequently software errors can only be found if several independent methods lead to the same result. The best tests available for the HERMES software are comparisons between Monte Carlo and real reconstructed data, where the used libraries are disjunct, except the admittedly critical interpolation of the magnetic field.

Software errors are analyzed by explicit tests of the resolutions with regard to the dependence on different kinematic variables.

Numerical Errors

Hardware based numerical errors are of little importance as all calculations are executed with double precision floating point numbers, i.e. 53 bit mantissa or $2.22 \cdot 10^{-16}$ accuracy. The number of floating point operations per track is below 10^6, even if the shooting method is applied. Therefore the hardware based numerical error should be smaller than $2.22 \cdot 10^{-13}$. The calculation of the track coordinates uses still significantly less operations.

Algorithmic sources of errors can be found mainly in the calculation of the tracks through the magnetic field. The magnet survey has an uncertainty of $\frac{\Delta B}{B} \leq 10^{-4}$, the Richardson extrapolation to regulate the step width was done for a maximal error of 10^{-4}, so that the resulting error should be smaller than$2 \cdot 10^{-4}$. This is valid for the accuracy of the shooting method as well as for the precision of the supporting points of the momentum matrix.

Consciously Accepted Uncertainties to Increase the Speed of the Software

This includes the already mentioned regulation of the step width, where the obtainable accuracy and the required time $t_{\rm cpu}$ for the track calculation are inversely proportional to one another. (To be exact, the accuracy is inversely proportional to $(t_{\rm cpu})^{n_v}$, where n_v is the order of the method.) The expected uncertainty should lie below the nominal detector resolution.

A further source of uncertainties is the finite number of support points for the momentum matrix, which results in uncertainties in the interpolation. These uncertainties depend strongly on the first and second derivatives of the momentum in the 4-dimensional parameter space of the matrix. For this reason an analytical error calculation is not possible, as no analytical function describing the magnetic field is available.

Instead special Monte Carlo generated events with particles that do not interact with matter and and whose positions in the HERMES detectors are exactly known can be used to test the accuracy of the momentum matrix interpolation. Figure 5.6 shows the result.

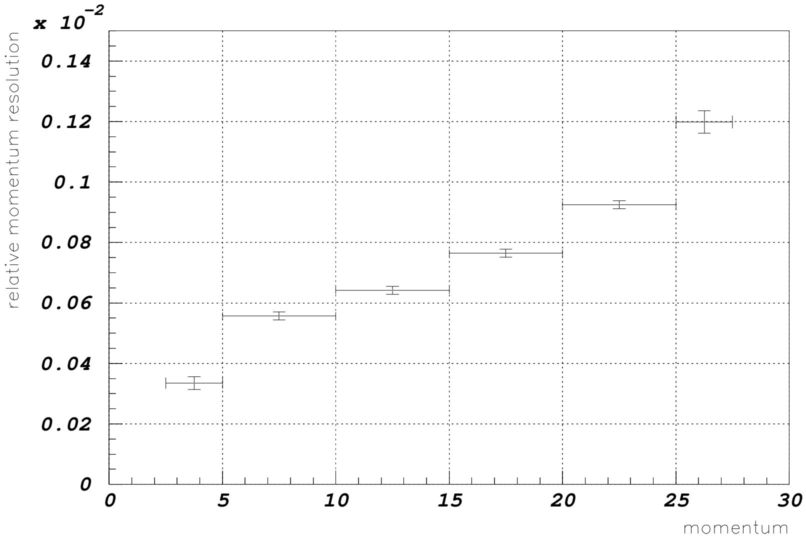

Figure 5.6: Determination of the momentum resolution of the momentum matrix interpolation in HRC. The uncertainty is a lot smaller than the one expected from detector resolution and multiple scattering and can therefore be neglected.

Alignment Errors, i.e. Inaccuracies in the Construction and the Surveying of the Detectors

Inaccuracies in the construction or in the surveying of the detectors lead to a shift of the reconstructed tracks and therefore contribute to an incorrect measurement of the scattering angle and the momentum. The scattering angle can be determined directly from the detector coordinates – changes in the slope of the beam have only a negligible influence –and its uncertainty can be calculated according to equations (4.3),(4.12) and (4.12). The uncertainty in the momentum measurement on the other hand can only be determined from simulations.

Rotations of the detectors and translations in y (i.e. parallel to the magnetic field of the spectrometer) and in z (in beam direction) only give second order contributions to the uncertainty. Translations in x on the other hand create to the first order a different deflection angle in the magnet and therefore lead to a first order contribution to the error in the momentum.

In the following examples individual detectors in the front and back drift chambers have been shifted in x and the Monte Carlo has been used to study the influence on the measured momentum and the reconstruction efficiency. For the front region the vertex chambers were intentionally not used for the track finding, because at the time they were also not available for the real data.

In the first example only one of the front chambers has been shifted in x by Δx:

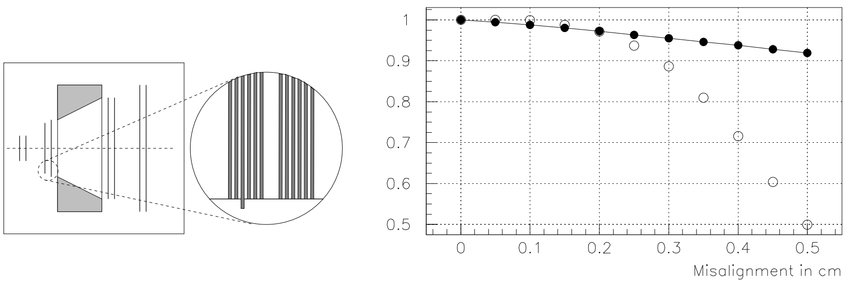

The solid circles (•) represent the measured momentum shifts ($\frac{\Delta P}{P}$); the empty circles (○) represent the reconstruction efficiency as a function of Δx. For comparison: The surveying of the HERMES detector was carried out with an accuracy of 0.02 cm.

If two x planes are shifted in the same direction, an already somewhat larger error is observed:

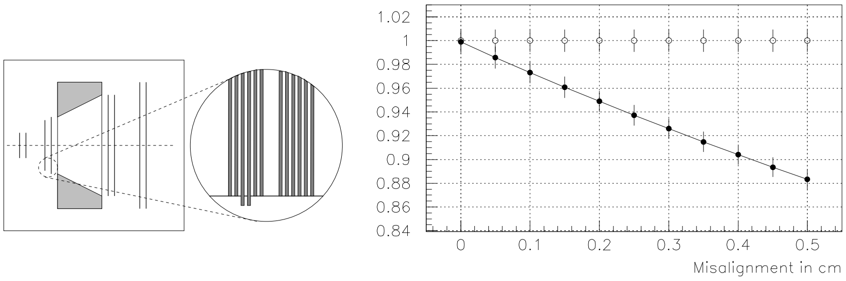

However, here the reconstruction efficiency is nearly constant at 100%, hence the number of reconstructed tracks appears to be a bad measure for an automatic alignment procedure.

An increase of the shift of the entire detector further increases the error, because the correction to x from u and v wires disappears:

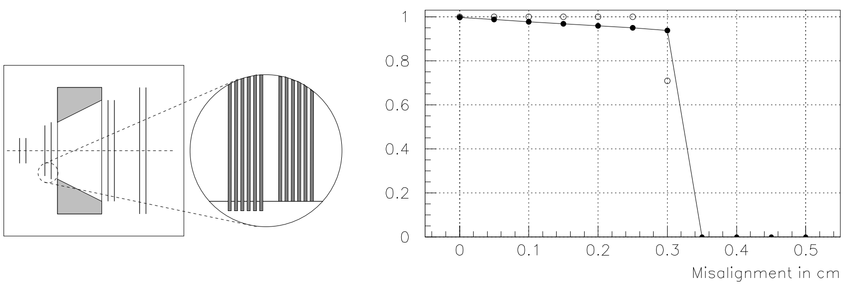

If the generated angular shift exceeds $\Delta x > 0.3$cm, then the bridging in the magnet fails and no tracks are found.

If all front chambers are shifted in parallel, no influence on the reconstruction efficiency is observed:

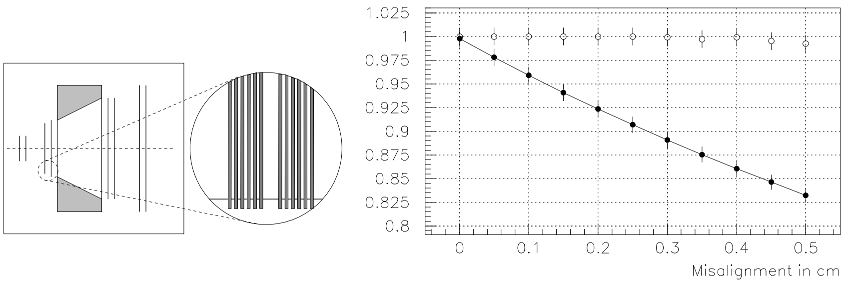

However, the error on the momentum becomes so large that a general shift of the size of the uncertainty of the surveying of HERMES would lead to a systematic error $> 1\%$. Studies with real data without a magnetic field could at least provide a relative alignment of the front and back drift chambers[GUT95I].

Shifts in the back drift chambers have a smaller impact on the momentum measurement, due to the fact that the lever arm for the angle measurement is significantly larger. Additionally there is a high degree of redundancy in the detectors for the parameter fit. A shifted chamber

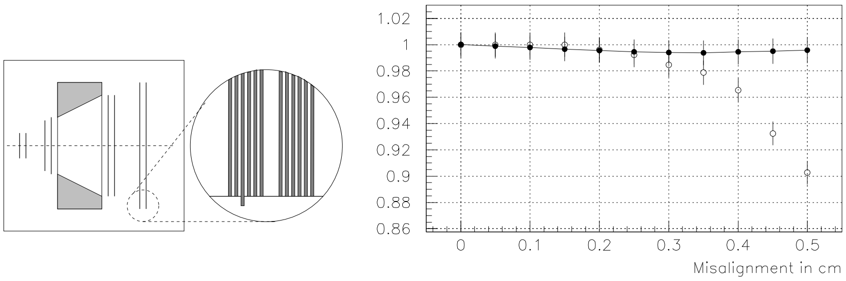

has little influence on the momentum resolution. Interestingly, if the shift exceeds a certain value, the hit resulting from the right left ambiguity may be assigned to the track, which lowers the efficiency but improves the error on the momentum measurement. This becomes even more clear in the event that two chambers are shifted together:

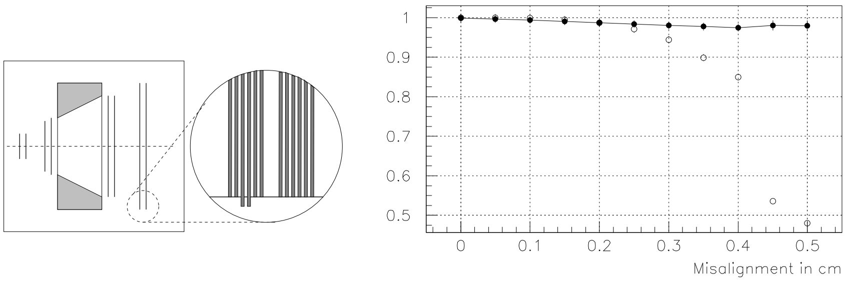

If a complete detector in the back drift chambers is shifted

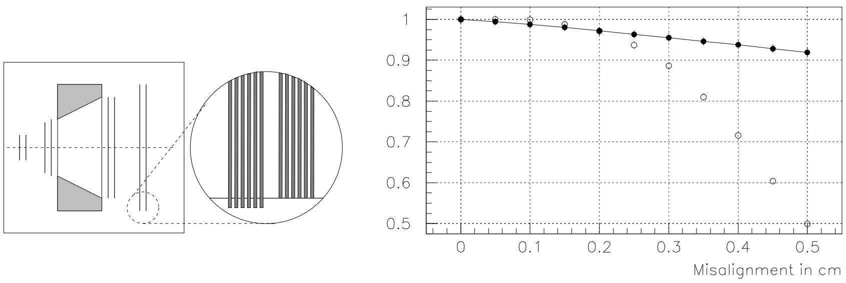

then the track is pulled into this direction and a lower efficiency and a worse momentum measurement are the result. In the case that two detector modules are shifted together

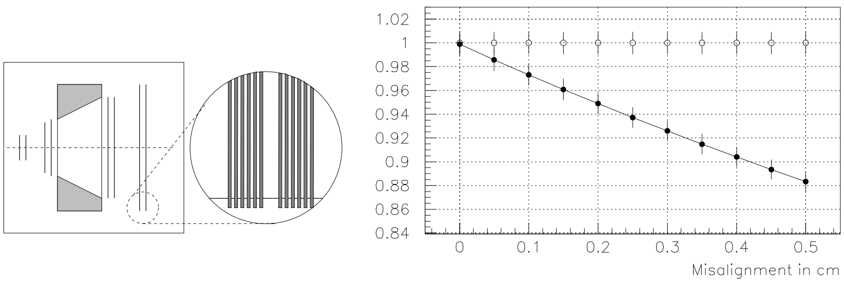

the efficiency does not suffer. Here also the track quality criterion χ^2 (equation (4.7)) is not significantly affected, due to the small lever arm between the two back detector modules. Therefore very complex and varied considerations are necessary for the automatic position measurement of the detectors for measured tracks to avoid misoptimizations.

Calibration Errors

Calibration errors that influence the momentum or angle resolution appear only in the drift chambers. The first data production, whose results will still be discussed in chapter 6, was only based on a rough calibration. The average spatial resolution per chamber was 500-700 $\mu\mathrm{m}$. By improving the space drift time relation and the t_0 values (see chapter 3.2.3), in the mean time chamber resolutions of up to 200 $\mu\mathrm{m}$ have been achieved.

Basically, incorrectly calibrated space drift time relations lead to errors similar to the ones resulting from chamber planes being shifted randomly relative to one another: The high degree of redundancy in the rear detector region minimizes this influence, while in the front region without the vertex chambers significant influences on angle and energy measurement are observed.

The next chapter will compare the resolutions that may be obtained for different chamber resolutions.

The Finite Spatial Resolution of the Detectors

The largest contribution to the error on the momentum and angle measurement for a particle in the detector arises from the finite spatial resolution of the detectors. The de-facto failure of the vertex chambers in the first year of data taking notedly affects the angle measurement in the front detector region.

Figure 5.7 shows the momentum resolution determined from Monte Carlo data in different energy regions for detector resolutions of 0 $\mu\mathrm{m}$(the pure reconstruction

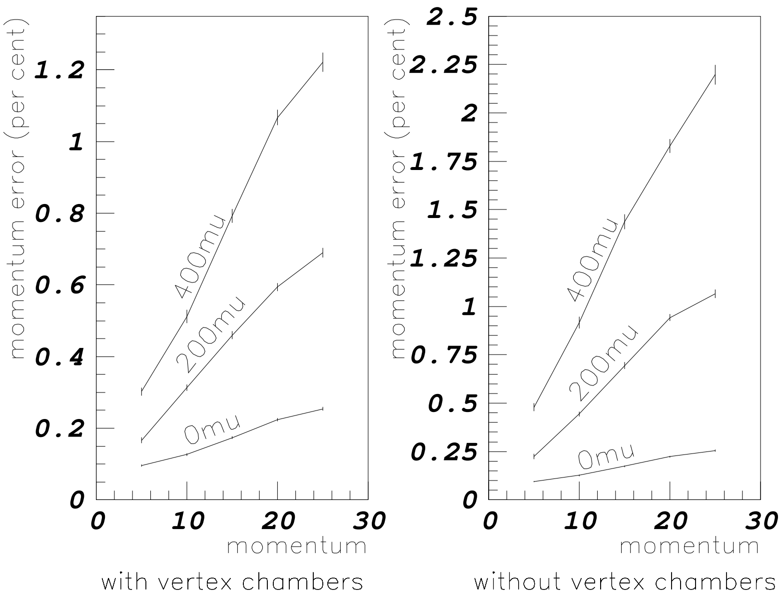

Figure 5.7: The momentum resolution of the spectrometer as a function of the particle energy and the chamber resolution, neglecting multiple scattering.

resolution), 200 μm(the design value) and 400 μm(the at the moment measured value).

For the angular resolution to the first order no energy dependence is expected. However, figure 5.8 shows a small tendency for a worsening of the resolution at larger energies. This may be explained by the fact that high energy particles cross the detector under small angles and that for small angles the lever arm for the determination of the angle is smaller. In the case of the reconstruction without vertex chambers a small energy dependence is expected, because the spatial coordinate of the forced bridging is energy dependent (compare 4.6.3).

Multiple Scattering of the Particles in the Detector and Target Material

In contrast to the measurement errors due to the reconstruction and the digitization of the chamber data, multiple scattering introduces an error that affects the trajectory and the energy of a scattered particle mostly before it enters the spectrometer. Figure 5.12 shows the radiation length of the material in the detector versus z.

Following the Bethe-Heitler equation a particle crossing material with the radiation

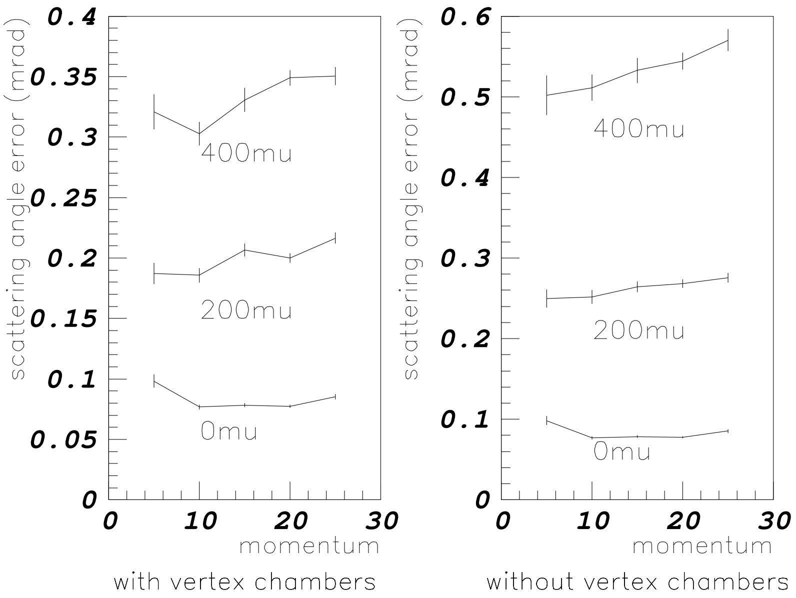

Figure 5.8: The angular resolution of the spectrometer in the scattering angle θ as a function of the particle energy and the chamber resolution, neglecting multiple scattering.

length x_R loses energy by emitting electromagnetic radiation:

$$-\frac{dE}{dx} = \frac{E}{x_R} \tag{5.23}$$

Therefore, the average energy of a particle at the position x_1 becomes

$$\langle E(x_1) \rangle = E_0 e^{-t}, \tag{5.24}$$

with $t = \int_{x0}^{x_1} \frac{dx}{x_R(x)}$.

For the variance of the angular distribution the Moliere theory[PDG94] for a particle with momentum p and velocity $v = \beta c$ is

$$(\Delta\theta)^2 = \left(\frac{13.6\mathrm{MeV}}{\beta c p}\right)^2 t(1 + 0.038 \ln t)^2. \tag{5.25}$$

Analogous to the previous chapter, the momentum and angle resolutions can be plotted for different detector resolutions. For the exact detector digitization – in

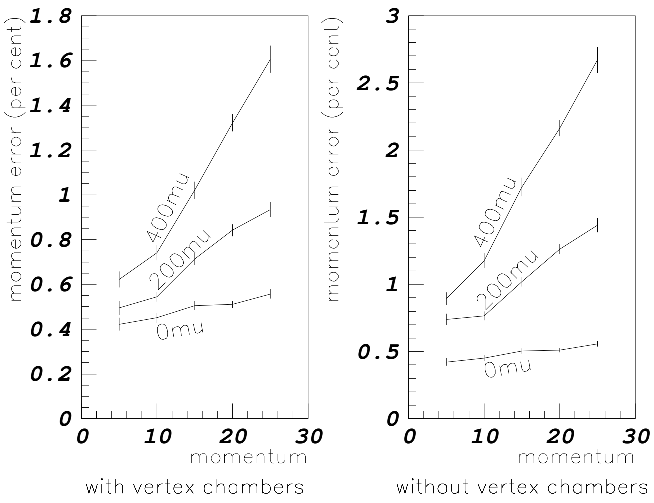

Figure 5.9: Momentum resolution of the spectrometer for different chamber resolutions. Multiple scattering effects are included.

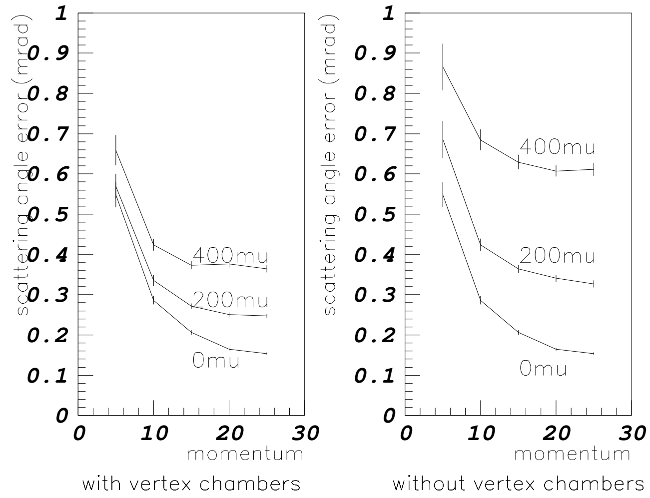

Figure 5.10: Angular resolution of the spectrometer for different drift chamber resolutions. Multiple scattering effects are included.

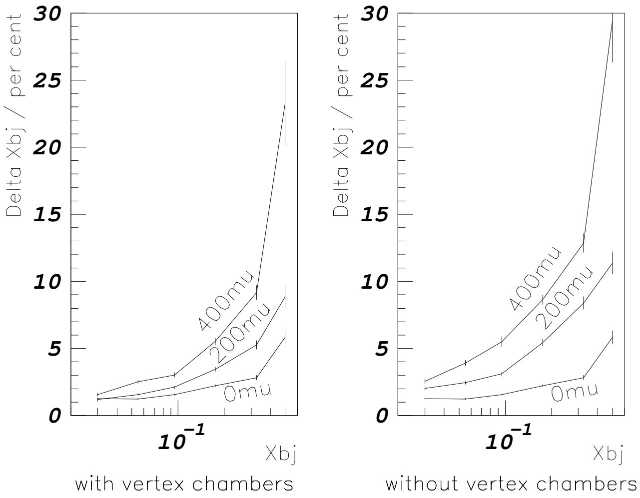

Figure 5.11: Resolution in x_{bj} of the spectrometer for different drift chamber resolutions.

the diagrams referred to as 0 $\mu\mathrm{m}$ spatial resolution – multiple scattering in the detector dominates the determined uncertainty of the measurement (see figures 5.9 and 5.10). The momentum uncertainty arising from the interpolation of the momentum matrix (see figure 5.6) is negligible at less than 0.15%. The effects of the uncertainties on the measurement of x_{bj} are shown in figure 5.11.

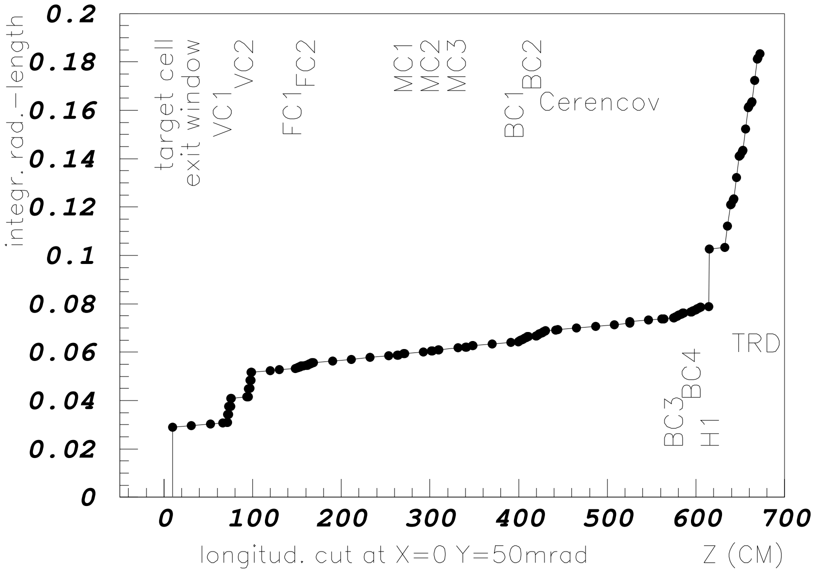

Figure 5.12: Integrated radiation length of a particle at $\theta_x = 0$ mrad $\theta_y = 50$ mrad in the HERMES spectrometer.

5.4 Effects on the Asymmetry Measurement

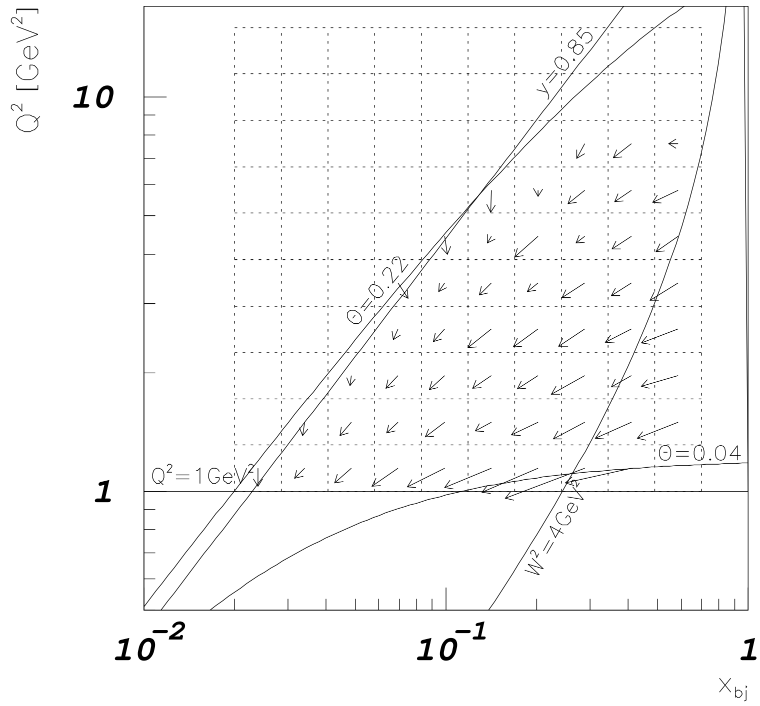

Figure 5.13: The migration of the kinematic variables x and Q^2. The average reconstructed value of x and Q^2 for the Monte Carlo generated data in each element of the lattice is indicated by the tip of the arrow.

As a result of the energy loss of the scattered particles in the detector material, the generated particles migrate in the x-Q^2 plane towards smaller x and Q^2 values (see figure 5.13). This systematic convolution of the kinematic variables can largely be compensated by the so-called 'unfolding' [AGO94].

The statistic alterations of the measured kinematics due to the finite detector resolutions lead to larger problems, that can reach 30%, especially for large x values ($x \approx 0.5$) (see figure 5.11). They introduce a contamination from events from different kinematic regions into the analysis, which may affect the measured asymmetry. The larger the expected error is, the larger is the first derivative of the distributions in the measured kinematic variable.

The structure function g_1^n from the 1995 data, that is based on the measurement on a polarized ^{3}He target, appears to be very flat at higher values of x, so that the expected systematic uncertainty of the measurement stays small over the entire kinematic range. For the measurement of g_1^p in 1996, detectors with increased spatial resolution will be available in the front region of the spectrometer, which will significantly improve the resolution at larger energies.

5.5 High Multiplicity Events

High multiplicity events pose a problem for the reconstruction, because the double track resolution of the front chambers directly influences the reconstruction efficiency. The cell width of 7 mm in about 1.4 m distance to the vertex does not allow the separation of two tracks with projection angles in u, v or x of less than 5 mrad. The probability for such an overlap of two tracks is, due to the small angle, to first order proportional to the number of tracks minus one and otherwise depends on the kinematics of the detected particles.

In a Monte Carlo experiment deep inelastic events were accumulated to simulate reactions with a certain multiplicity. The result is shown in figure 5.14 as a function of the number of detected particles.

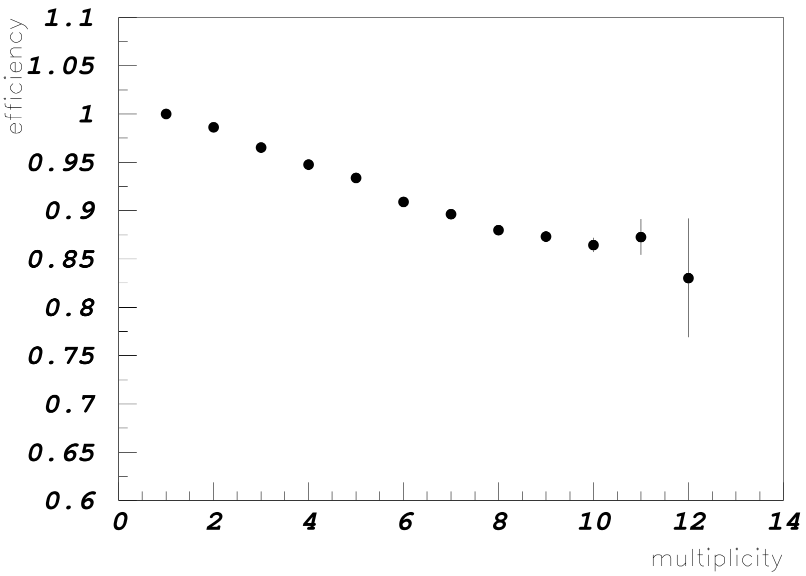

Figure 5.14: The dependence of the reconstruction efficiency on the multiplicity of the events. The reduction of the efficiency for higher multiplicities is mainly based on the loss of double tracks with small common angle.

5.6 Ghost Tracks

If the reconstruction were to produce a significant amount of ghost tracks, this would considerably deteriorate the results of the measurement. These tracks principally represent another form of – software induced – correlated background (see chapter 4.4).

However, it can be demonstrated, that for the background and multiplicity conditions in the HERMES detector ghost tracks are not to be expected:

Here it is again problematic to determine the number of ghost tracks that the software generates from real data. The number and position of the real tracks in the real data are not a priori known for comparison.

Monte Carlo studies have better starting conditions: In fact, despite the low redundancy in the front region, using the forced bridging technique and the large number of drift chambers in the back region, HRC could not find a single ghost track in 20,000 deep inelastic Monte Carlo events. The ghost track suppression appears to be sufficient.

Nevertheless, the Monte Carlo program does not generate a realistic background. For this reason additional tests where carried out with high track multiplicities, by far exceeding the multiplicities that can be expected for HERMES.

Here the track contamination and its variance as a function of multiplicity is of interest. The track contamination is given as

$$k = \frac{\text{number of hits not from this particle}}{\text{number of hits}} \tag{5.26}$$

for a reconstructed track. The number of hits that are not caused by the particle itself can be determined in Monte Carlo events. Here a linear increase with the multiplicity is expected that is especially dominated by the double track resolution of the front chambers (see figure 5.15). For a track contamination of more than 25% the track can be referred to as a ghost track.

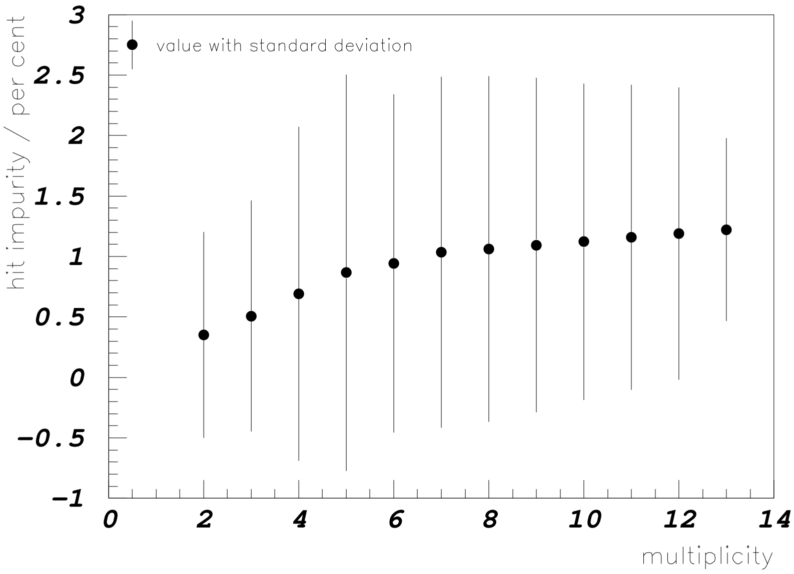

Figure 5.15: The track contamination as a function of the multiplicity of the events. The error bars indicate the standard deviation of the measurement, not the measurement error.

Chapter 6

First Preliminary Results

6.1 Kinematic Distributions

A natural first test of the data reconstruction is the comparison of the distributions of kinematic variables from reconstructed data and from reconstructed Monte Carlo events. In this way differences in the geometric representation of the experiment as well as errors or inadequacies in the Monte Carlo generators may be found. The Monte Carlo generators were programmed on the basis of the NMC measurements.

Here the distributions of 20,000 positrons from deep inelastic Monte Carlo events are compared to the distributions of 75,000 particles from 20 runs that were identified as positrons. A run is the data taking period of 5–15 minutes, in which about 500 Megabyte of raw data are collected.

The following facts have to be considered in advance: Monte Carlo generated events are generated corresponding to the kinematic plane which describes the HERMES acceptance (see figure 6.1). For this reason the reconstructed data as well as the real data have to be restricted to these parameters. The individual restrictions can be explained as follows:

$$Q^2 > 1\mathrm{GeV}^2, \tag{6.1}$$

because the structure functions only show scaling in this region;

$$y < 0.85, \tag{6.2}$$

to keep the radiative corrections small – the trigger threshold in the calorimeter is set to 3.5 GeV for the same reason.

$$W^2 > 4\mathrm{GeV}^2, \tag{6.3}$$

to exclude the resonance region;

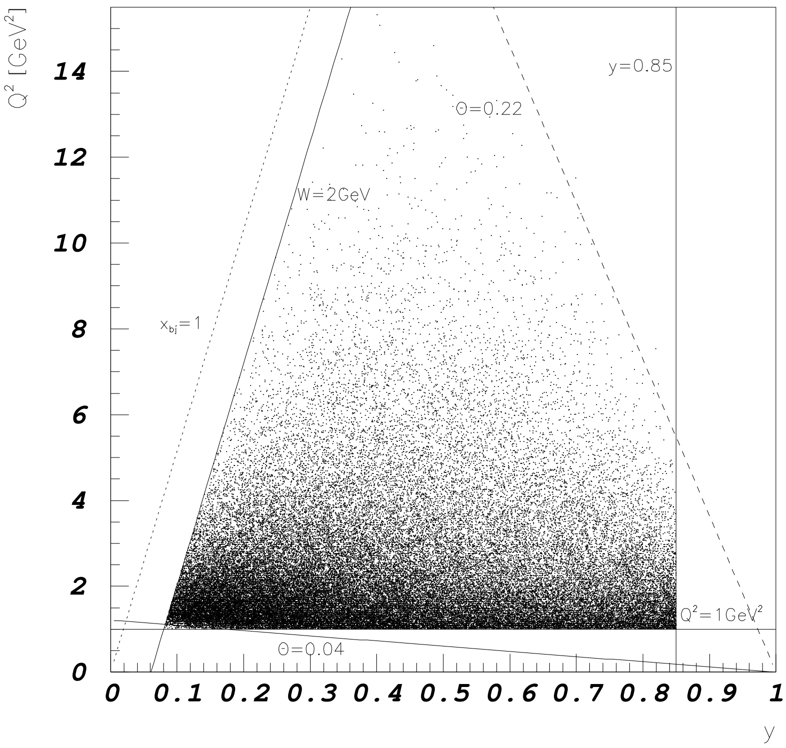

Figure 6.1: The acceptance of the Hermes spectrometer in the $Q^2 - y$ plane. For this diagram the deep inelastic events from only 10 runs have been used to keep the distribution clear.

$$0.04 \leq \theta \leq 0.22, \tag{6.4}$$

corresponding to the angular acceptance of the spectrometer.

Furthermore, for the real data a contribution from positrons that do not originate from deep inelastic scattering must be taken into account. This background, e.g. from photon conversion, leads to an alteration in the spectra if it is not corrected for.

For a charge symmetric background the measured electron spectrum can be subtracted from the positron spectrum to correct it (see figure 6.2).

Figure 6.3 shows the comparison between Monte Carlo generated deep inelastic events and real data where the positron background has been subtracted.

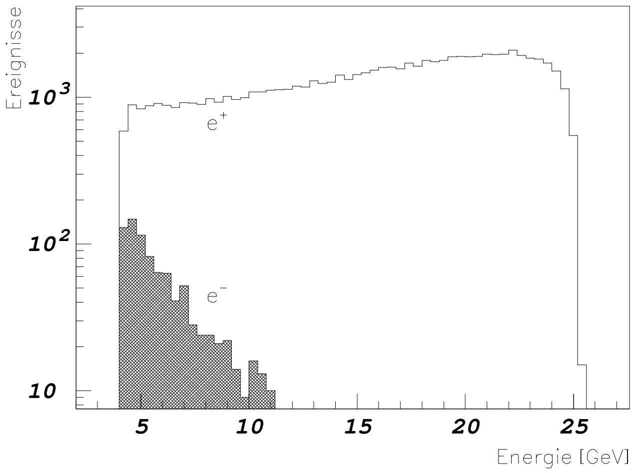

Figure 6.2: Contribution of positrons and electrons to the data. Due to the electron contribution the positron contribution from photon conversion can be estimated.

The first diagram shows the momentum distribution of the electrons in deep inelastic events. Small deviations can be observed. The distribution of Monte Carlo data are steeper than the real data for large momenta. This effect is understood and can be traced to the difference in chamber resolution in the experiment and the Monte Carlo. In this energy region the momentum measurement is especially sensitive to the chamber resolution and a smearing, as should not occur for a good calibration, leads to a smaller slope of the curve for high momenta. For small energies a small deviation is observed that results from pion contamination of the real data. Improved particle identification algorithms (see chapter 4.12) will further suppress this effect.

The angular distributions in ϕ and θ show good agreement. This is also true for the vertex distribution, which in both cases corresponds to the basic density distribution in the internal gas target convoluted with a finite resolution.

The small deviations in Q^2 and x are based on the momentum deviations explained before.

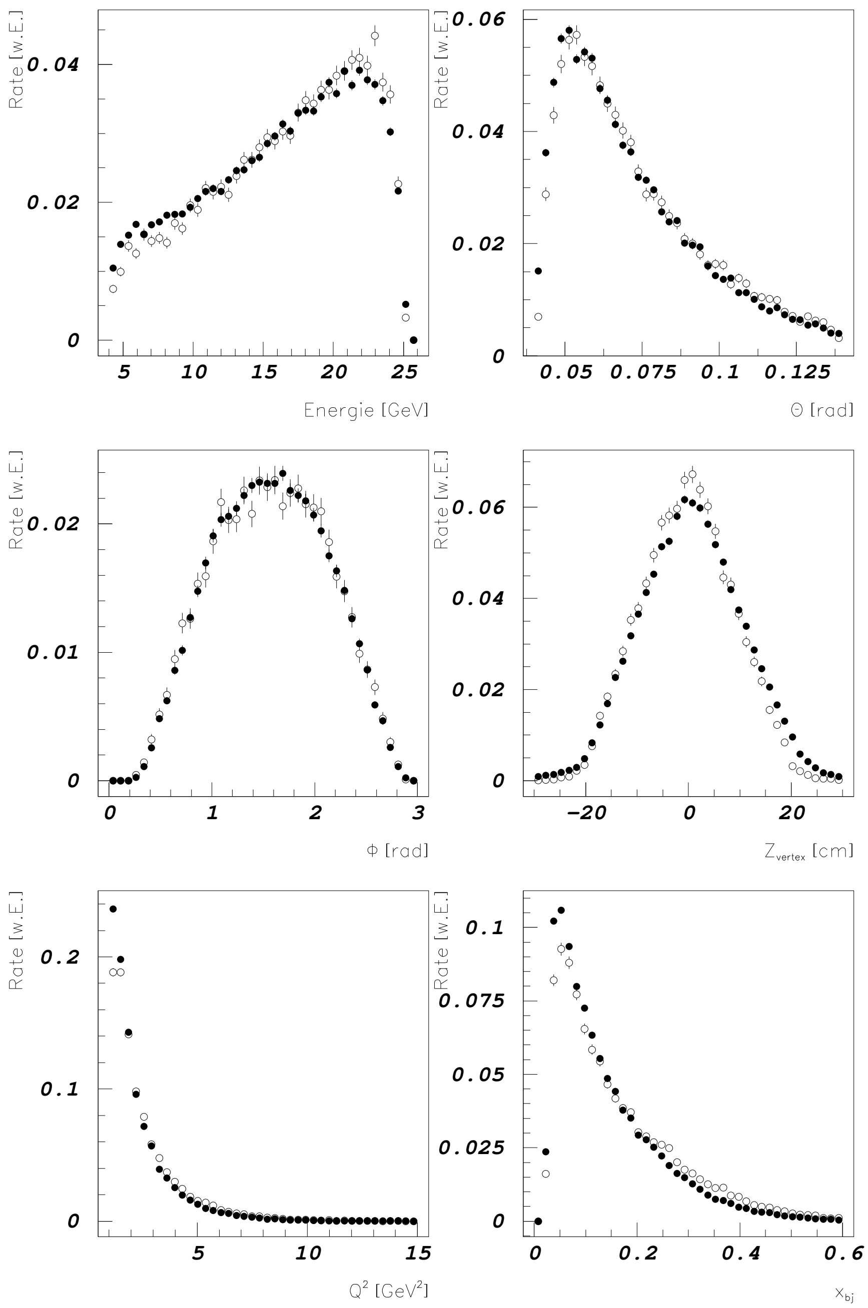

Figure 6.3: Comparison of Monte Carlo data (○) to real data (●). The kinematic distribution show a good agreement between model and reality.

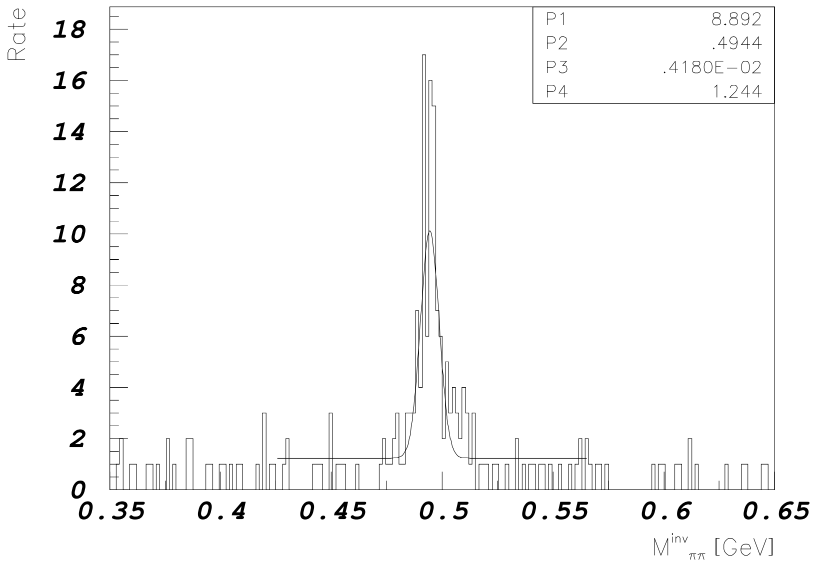

Figure 6.4: The K_s^0 signature measured by HERMES. Plotted is the invariant mass for two pions of opposite charge, where the pion vertex lies at least 30 cm behind the primary electron vertex. The measured mass $m_{K^0}^{\rm exp} = (494.4 \pm 0.7)$ still shows a small deviation relative to the literature value of $m_{K^0} = (497.672 \pm 0.033)$.

6.2 The K^0 Mass

The determination of the K^0 mass from the K_s^0 decay

$$K_s^0 \longrightarrow \pi^+ + \pi^- \quad (68.6\%) \tag{6.5}$$

is particularly suited for the calibration of the spectrometer.

- The mass $m_{K^0} = (497.672 \pm 0.033)$MeV[PDG94] is sufficiently well known.
- The life time $\Delta t_{K^0} = (0.8925 \pm 0.0012)10^{-10}s$ is short enough to expect practically all decays in front of the front chambers and long enough to create a sharp signal.
- The cross section for K_s^0 is large enough to form a clear signal above the background.

The K_s^0 mass is calculated from the invariant mass of two detected pions with opposite charge and common vertex behind the primary vertex:

$$\begin{aligned} (m_{K^0})^2 &= (p_{\pi^+} + p_{\pi^-})^2 \\ &= 2(m_\pi^2 + E_{\pi^+}E_{\pi^-} - \vec{p_{\pi^+}}\vec{p_{\pi^-}}) \end{aligned} \tag{6.6}$$

The additional condition that the two pion vertex lies 30 cm behind the primary vertex results in a practically background free kaon spectrum. However, the statistics are strongly reduced. This is illustrated in figure 6.4. An obvious ansatz for a fit function is a Gaussian with a constant background. Here the width is dominated by the detector resolution and not by the decay width. The result of the fit (χ^2 = 0.6) gives a kaon mass of $m_{K^0}^{(\mathrm{exp})} = (494.4 \pm 0.7)$ MeV and a width of $\Delta m_{K^0}^{(\mathrm{exp})} = (4.2 \pm 0.9)$ MeV. The value for m_{K^0} indicates an error in the calibration of the spectrometer in the data reconstruction of 0.5%. In the meantime the extent of the parametrisation of the magnetic field that was used in this analysis has been revised. It was extended by 20 cm in forward and backward direction relative to the beam axis, because the stray fields also contribute to the momentum measurement. First studies show that this corrects the improved error in the calibration.

The decay width ($\Delta E_{K_s^0} \approx \frac{\hbar}{2\gamma\Delta t_{K_s^0}} = \gamma^{-1} \cdot 7.4 \cdot 10^{-6} eV$ with $\gamma = 4 \ldots 40$) is negligible compared to the detector resolution. Hence, the measured width leads directly to the resolution of the spectrometer:

$$\begin{aligned} \Delta m_{K^0} &= \frac{1}{m_{K^0}} \left\{ \left[(\Delta E_1 E_2)^2 + (\Delta E_2 E_1)^2 \right] [1 - \cos(\theta)]^2 \right. \\ &\quad \left. + \left[\Delta\theta E_1 E_2 \sin(\theta) \right]^2 \right\}^{\frac{1}{2}} \end{aligned} \tag{6.7}$$

where θ is the angle between the two pion momenta.

A comparison of the measured kaons to equation (6.7) leads to $\Delta E = 0.04$ GeV and $\Delta\theta = 1$ mrad. For a mean pion energy of 3.6 GeV follows an energy resolution of about 1% in this energy range, which is in good agreement with the results from Monte Carlo studies (see chapter 5.3).

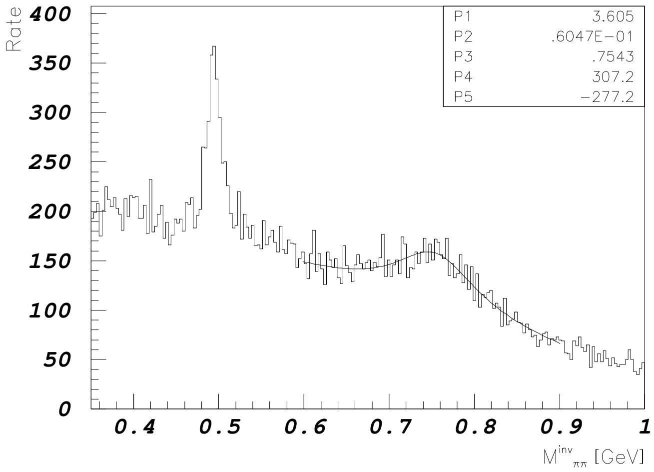

Figure 6.5: The invariant mass distribution for two pions with opposite charge. The sharp peak on the left side results from the K_s^0, the wider peak on the right from the ρ-resonance.

6.3 The ρ(770) Mass

Contrary to the just discussed K_s^0-resonance, the decay

$$\rho \longrightarrow \pi^+ + \pi^- \quad (\sim 100\%) \tag{6.8}$$

has a large natural line width. The ρ-mass is cited as $m_\rho = (769.9 \pm 0.8)$ MeV with a width of $\Delta E_\rho = (151 \pm 1.2)$ MeV[PDG94].

Figure 6.5 shows the invariant mass spectrum for two hadrons with common vertex and opposite charge from about 1000 runs. The hadrons are mostly pions. However, in the momentum region below 6 GeV they cannot be unambiguously identified (see chapter 4.12.2). The sharp K_s^0 signal on the left and the wider ρ resonance can clearly be seen.

A fit with a Breit-Wigner distribution and a linear falling background in the range from 600 to 900 MeV leads to a value for the ρ mass of $m_\rho^{(\exp)} = (754 \pm 10)\ MeV$. For the relativisticly reduced width of the resonance $\Delta m_\rho = (60 \pm 6)$ MeV is obtained. The χ^2 value of the fit is $\chi^2 = 0.94$, corresponding to an uncertainty in the mass measurement of $\frac{m^{(\exp)} - m}{m} = (-1.9 \pm 1.3)\%$.

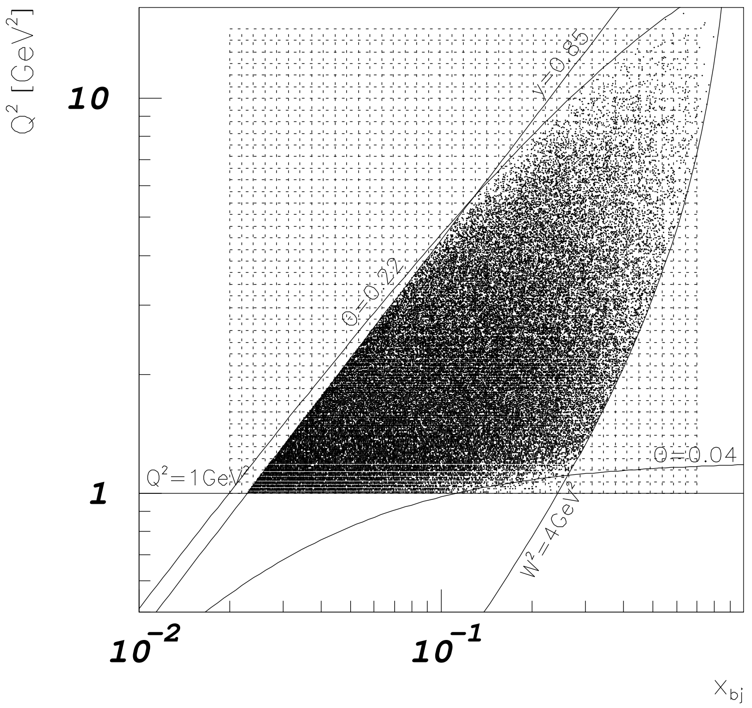

Figure 6.6: Partition of the Q^2-x in lattice with 40×40 points. The kinematic boundaries are shown together with the events from 10 runs. Only about 30% of the lattice are covered.

6.4 The Asymmetry $A_1^n(x, Q^2)$

The described analysis represents only preliminary results and is not supposed to anticipate the soon to be expected final g_1 analysis of the HERMES collaboration.

In its first year of data taking in 1995 the HERMES experiment ran with a longitudinally polarized ^3He target with a target density of $1 \cdot 10^{15} \frac{\text{nucleons}}{\text{cm}^2}$.

In this analysis only about one third of the reconstructed data were used, because at the time of the analysis not all target polarization values were available yet. Simple filters for data quality have been used. It was taken into account that a run may contain unusable data for a limited range of time due to detector trips and that if one detector half tripped, the other half might still be usable.

The number of detected positrons, normalized to the length of the time interval Δt_i, the luminosity $\mathcal{L}_i$ and the data taking dead time T_i, are a criterion of quality:

$$\mathcal{C}_i^{e^+} = \frac{N}{\Delta t_i \mathcal{L}_i (1 - T_i)}. \tag{6.9}$$

This parameter test loses in reconstruction efficiency, that result from chamber trips, as well as those that result from problems with the particle identification.

Additionally the mean signals of preshower and Cerenkov counter, as well as the ratio of calorimeter energy and momentum for electrons and pions were used for the particle identification.

The distributions of these quality parameters and the cuts used as defined by a 2σ interval around the expectation values of the distributions, are shown in figure 6.7.

For the analysis the data are divided into intervals of 200 second lengths, separately for the upper and lower detector half and for the polarization state. Due to variable run lengths and the switching of the target polarization during a run, the interval length effectively may be between 10 and 250 seconds. In each of these intervals the registered deep inelastic events are counted in a lattice with 40×40 elements in the x-Q^2 plane (see figure 6.6). Then they are stored together with the integrated luminosity $\mathcal{L}$ and the quality parameters.

In this way $2.57 \cdot 10^6$ events are evaluated for the first third of the 1995 data. In a second step the quality parameters are compared to the admissible limits. Using the beam and target polarization and the attenuation factor $A_1^{^3\mathrm{He}}(x, Q^2)$ is calculated for every lattice point following equation (2.50) with the photon polarization $D(x, Q^2)$ (see equation (2.37)). After the quality controls, $2.10 \cdot 10^6$ events remain.

To calculate A_1^n, equation (2.52) is applied to every point in the lattice and finally the lattice is projected onto 10 elements in x. The elements of the lattice have to be weighted accordingly, that is proportional to the inverse square of the statistic uncertainty of their contents. The radiative corrections to $A_1^n(x, Q^2)$ are applied using an iterative method following [AKU95I].

With equation (2.47) A_1 can be transformed into g_1 using $F_2^n(x, Q^2)$ [NMC92] and $R(x, Q^2)$ [WHI90]

About two months after the completion of this thesis the first preliminary results from the HERMES experiment have been published. The analysis is essentially based on the above described method. The data selection for the preliminary result was based on very restrictive conditions. Less than 40% of the 1995 data are used for the calculation. In this preliminary result the values for the lowest and the highest x_{bj} were not used. For the final publication it can be expected that further spectrometer studies allow the recovery of a large part of the data that are not yet used for the analysis. This would help to significantly reduce the statistic and systematic uncertainty of the measurement, which now is still relatively large.

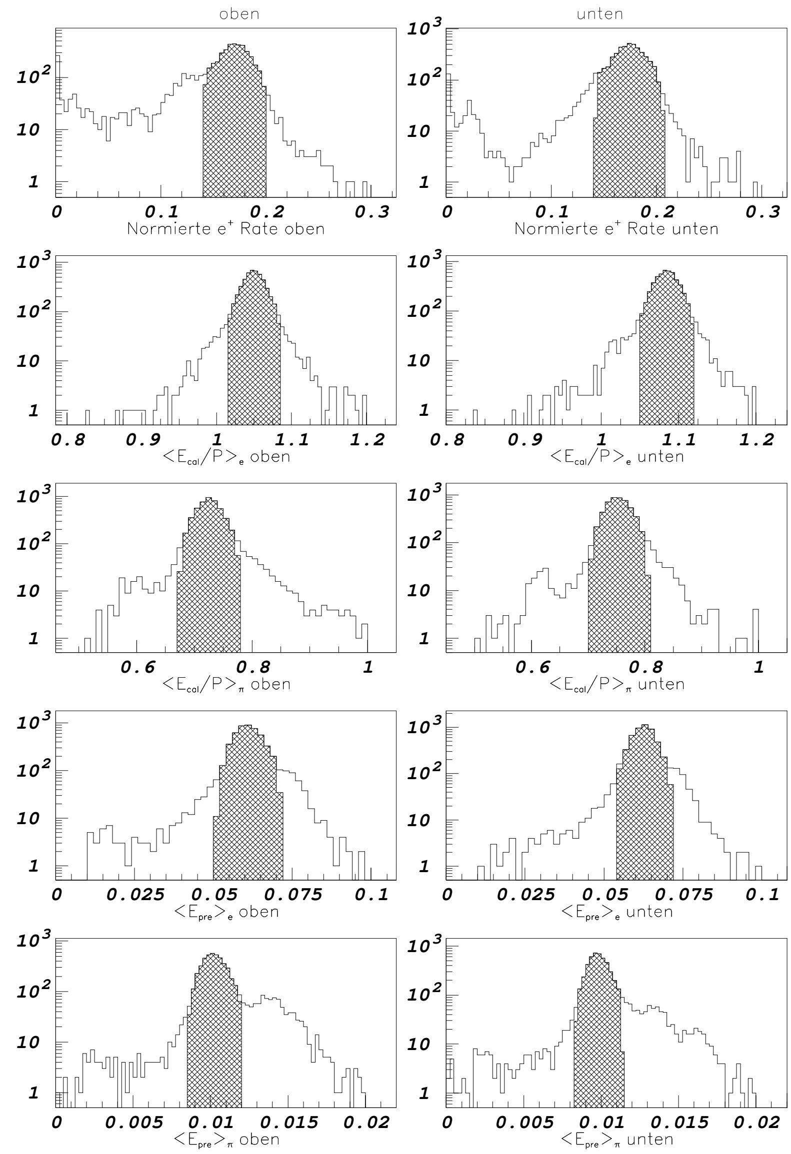

Figure 6.7: These distributions were used for the quality control of the A_1 analysis. At the top the normalized rate of deep inelastic events is shown, below the mean calorimeter energy divided by the momentum and the mean preshower energy, both for positrons and pions. On the right and left side the upper and lower detector are shown separately. The double signal in the Cerenkov is the result of a change in the radiator gas during data taking.

The preliminary HERMES result for g_1^n is shown in figure 6.8. For the calculation of the Ellis-Jaffe integral (see equation (2.33)), g_1^n is calculated for a fixed $Q^2 = 3$ GeV^3, assuming that A_1 does not depend on Q^2. The values outside the published x-region have to be extrapolated for the Ellis-Jaffe integral. For the region of $x < 0.03$ it is assumed that $g_1(x) = \mathrm{const.}$[ELL88], while for $x > 0.6$ $g_1(x) \sim (1-x)^3$ is used following [BRO95].

The preliminary result is

$$\int_0^1 dx\, g_1^n(x) = -0.032 \pm 0.013_{\mathrm{stat.}} \pm 0.017_{\mathrm{syst.}}. \tag{6.10}$$

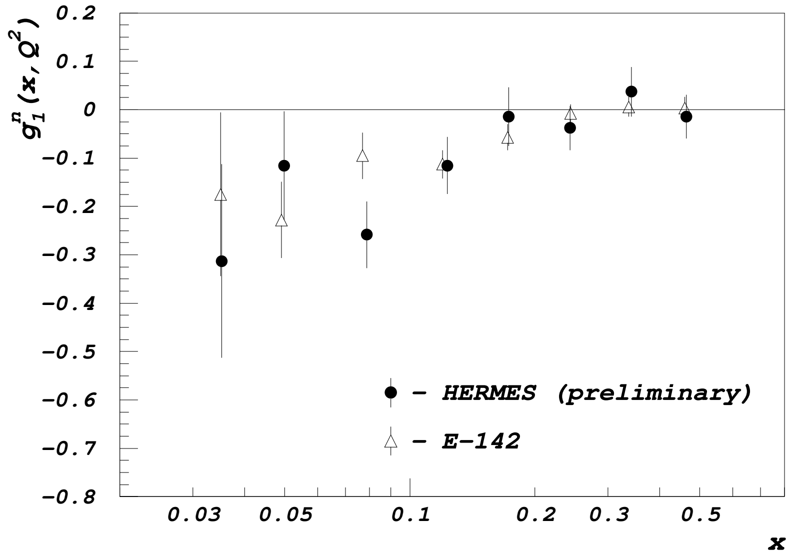

Figure 6.8: The preliminary HERMES result for g_1^n. For comparison the results of E-142 are shown as well. Only statistical uncertainties are included. $g_1^n(x,Q^2)$ is shown for every x value at the respective mean Q^2.

Chapter 7

Conclusion and Outlook

The object of this thesis was to create a reliable and fast reconstruction program that allows the analysis of data in a manner suited for publication shortly after the end of the first data taking period. The reconstruction program together with other essential parts of the analysis software was in fact able to analyse the first events and to determine momentum distributions only three hours after the complete detector had started to take data.

The failure of a large part of the magnet chambers as well as difficulties with the vertex chamber electronics complicated the analysis. Nevertheless, despite these unexpected incidents HERMES could prove soon after the running in phase of the experiment, that the taken data agreed with the expectations resulting from the measurements of earlier experiments. The determination of the kaon mass from $K-s$ decays in the detector could demonstrate that the momentum measurement of the spectrometer is calibrated to better than 0.5%.

The thus proven reliability of the analysis software was mainly achieved by the application of modern programming methods and intensive tests with realistic Monte Carlo simulations.

After the conclusion of the first data taking period the most important tasks, namely the calibration of the detectors and the data quality control of individual runs, will soon be completed. Thanks to the high speed of the analysis – the complete reconstruction of the 1995 data requires about 3 weeks – the first results can be expected in the near future.

Changes to the detector in 1996 make extensions to reconstruction software necessary. The strong holding fields for the hydrogen/deuterium target must be considered in the vertex determination and additional drift chambers in the front region of the detector have to be integrated into the track reconstruction. The modular structure of the program will allow a simple and fast realization of these objectives.

Appendix A

The Online Data Bank - DAD

HERMES had decided at the beginning of the software development to use a consistent data management module. This way the data format for the analysis as well as the format for the expectedly large amounts of constant and variable detector parameters are always readily available to all analysis components.

Several points needed to be considered for the decision about a software package:

- Availability. Was the product available free of charge? A commercial product is not generally applicable in a large collaboration if considerable financial resources are needed.
- Support. Is the product supported and will it be developed further?
- Language Support. Is it possible to access data in C and Fortran77, the two programming languages originally supported by HERMES ?
- Resources. Is the additionally needed CPU power and storage space small?
- Interface. Are user interfaces available that allow easy access and modification of the data bank?

The reason for the collaboration's decision in favour of the ADAMO package instead of other free packages, e.g.GDBM by the Free Software Foundation, lies mainly in the requirement for Fortran77 support. This was only available in good quality for ADAMO.

ADAMO itself contains data management functions for individual processes, but no data bank management. Also the user interfaces needed some improvement.

Through the development of the HERMES packages DAD and PINK these and other limitations were overcome, while the original structure of the previously developed software packages, especially the HERMES Monte Carlo program and the reconstruction, were retained completely.

A.1 The Data Management Module ADAMO

ADAMO[PTG94] was developed by the Programming Techniques Group at CERN. In ADAMO data are organised in an *entity-relationship* model, i.e. it manages data sets and relations between them. ADAMO offers a multitude of resources to the programmer to allow an effective access of the data. However, only one process on one machine can access this data bank.

The data access offered by ADAMO is not sufficient for the analysis software, which is realized as a chain of successive processes running in parallel on different processors and computers. Control and monitoring programs that record the detector status during data taking need the possibility to communicate – here a data bank on the basis of ADAMO could be used as well as a communication service.

A.2 The Client-Server Concept

DAD was realized as a client-server concept: The data organization is carried out by one ore several central processes, called servers. These servers also distribute the data to the client processes according to their requirements.

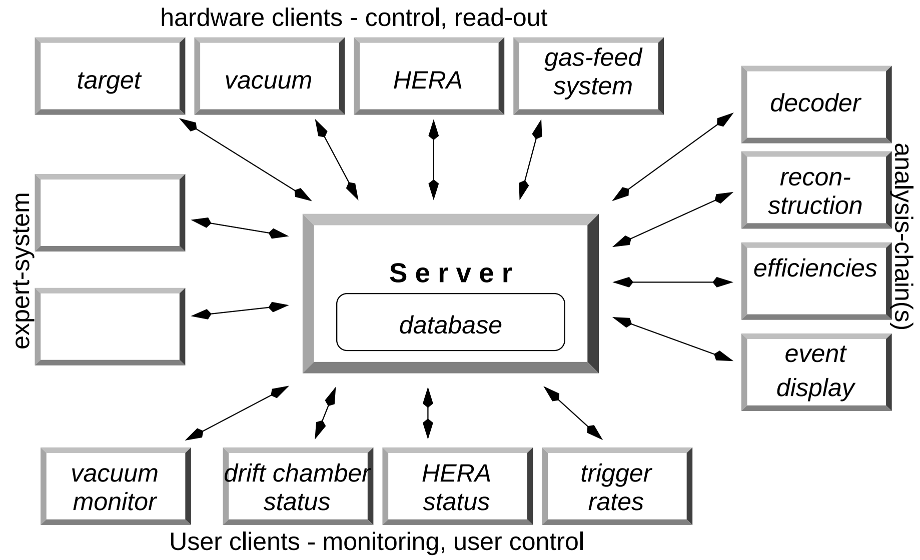

Figure A.1: The client-server concept of DAD in the HERMES experiment. Hardware clients send data to the server and receive control commands through the server from the user clients or the expert system (not yet implemented). The analysis chains use the data in the server for the interpretation and calibration of the measured data in the data stream of the events.

The server itself is based on a multi-threaded kernel, that is able to respond to the practically coincident requirements simultaneously.

The simplest form of communication is the exchange of complete data sets, in the ADAMO concept called DATAFLOWs. In doing so, a multitude of tables and data are transferred and either updated in the server or made available for the client.

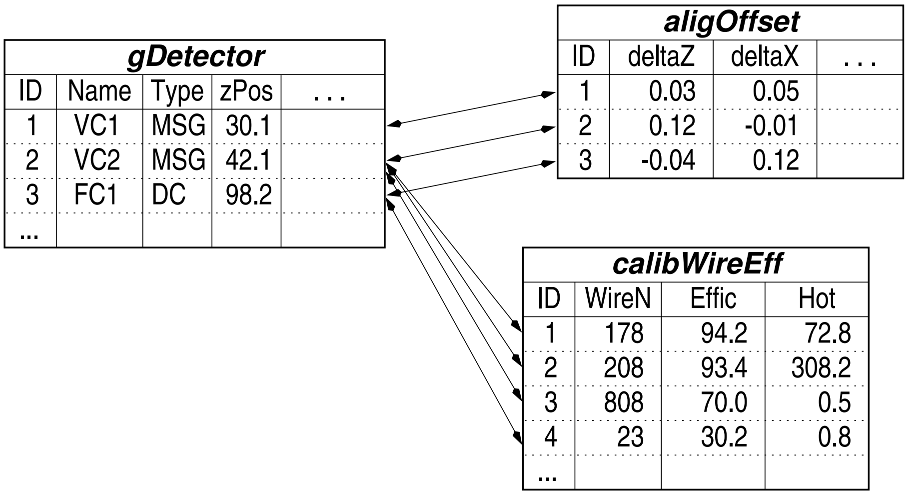

Figure A.2: Example of an ADAMO data set, called DATAFLOW. It consists of tables and relations that connect certain table entries to one another.

Semaphores that a server makes available to the clients control the access to the modified data.

As not always all the data of a data set are required, DAD offers two additional modes of data transfer with reduced bandwidth.

A.3 Time Dependent Information

Most data that have to be stored about the experiment control are time dependent. DAD takes this into account through a special mode that supports the storage as well as the access of time dependent data at a given time or time interval.

Examples for this kind of application are:

- the display of the detector status over a range of time in the past,
- the evaluation of the detector status for the quality control and
- the analysis of events, where the time dependent detector geometry and calibration constants are requested from the server.

The data transfer between client and server is exclusively limited to the changes in the data set. The costly transfer of the entire data can be avoided.

A.4 Booking News

While data arrive at the server, clients that are interested in changes in certain parameters can automatically request these from the server. Data are booked from the server by assigning a condition to a data set that is tested by the server when new data arrive. If the condition is fulfilled, the new data are transferred to the booking client.

For example monitoring programs receive their data in this way, that then are shown in *tcl/tk*[OUS94] based displays (see chapter A.6).

Also the clients for the experiment control exchange their information through the booking of news, by booking the news 'command table' under the condition that a command was addressed to them. Using the sender, which is also stored in the command table, they can answer to the command using the same mechanism.

In this way DAD has become and essential part of the HERMES experimental control.

A.5 Dad as Adamo IO Driver

Additional to the data bank properties, DAD relative to ADAMO offers improved I/O routines. These routines allow high data through-put and directly support the concept of the data stream for the analysis chain.

Data between decoder and reconstruction program are exchanged exclusively in this format to increase the speed of the production.

DAD provides additional support in the form of a data filter. Using the call

```
$ hexe hrc.output --output hexe.output \
       ++filter     'rcCluster:E > 1.5' \
       --expression 'rcTrack:2:rProbPion>0.8'
```

for example the output of the reconstructin program can be filtered for all events that contain at least two pions. Additionally, the calorimeter cluster are only kept in the data stream if their energy is larger than 1.5 GeV.

A.6 Pink – a graphical user interface for Dad

Based on *tcl/tk* and DAD K. Ackerstaff and M.-A. Funk have developed a user interface for DAD and ADAMO called PINK[ACK95].

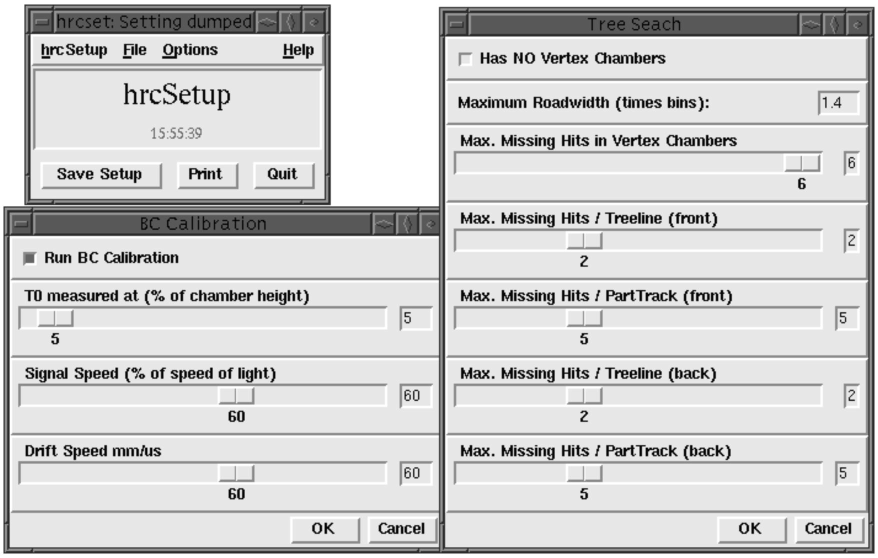

Figure A.3: An example for a PINK application. Here the parameters for the reconstruction can be selected interactively.

In PINK for example it is easy to use interfaces to the data bank or to the experiment as well as monitors for the status of detector and analysis and special interactive displays for events may be programmed.

An example for a PINK application is shown in figure A.3 . It allows the interactive control of the reconstruction program by setting various parameters.

Bibliography

[ACK95] K. Ackerstaff, M.A. Funk et al.: **PinK: A TCL/Tk based Database Interface to ADAMO and DAD,** Proc. of CHEP 95, Rio de Janeiro, 18.9.–22.9.1995.

[AGO94] G. Agostini: **A Multidimensional Unfolding Method Based on Bayes' Theorem,** DESY 94-009 (1994).

[ANS95] M. Anselmino, A. Efremov and E. Leader: **The Theorie and Phenomenology of Polarized Deep Inelastic Scattering,** Phys. Rept. 261 (1995), 1.

[AKU95I] I.V. Akushevich and N.M. Shumeiko: **Radiative Effects in Deep Inelastic Scattering of Polarized Leptons by Polarized Light Nuclei,** J. Phys. G20 (1994), 513.

[BAT90a] P. Battaiotto et al.: **The Tree-Search Processor for Real Time Track Pattern Recognition,** Nucl. Instr. and Meth. A287 (1990), 431.

[BAT90b] P. Battaiotto et al.: **A fast Track Finder for Triggering Applications,** Nucl. Instr. and Meth. A293 (1990), 531.

[BEN95] Th. Benisch: **Der Luminositätsmonitor für das HERMES Experiment,** Diplomarbeit, Universität Erlangen-Nürnberg (1995).

[BLO95] J. Blouw et al.: **Design and Performance of a large Microstrip Gas Tracker for HERMES,** In Vorbereitung zur Veröffentlichung in Nucl. Instr. and Meth..

[BJØ66] J.D. Bjørken: **Applications of the Chiral U(6) $\otimes$ U(6) Algebra of Current Densities,** Phys. Rev. 148 (1966), 1467;
J.D. Bjørken: **Inelastic Scattering of Polarized Leptons from Polarized Nucleons,** Phys. Rev. D1 (1970), 1376.

[BRA95a] B. Braun: **Spinrelaxation von Wasserstoff und Deuterium in Speicherzellen,** Doktorarbeit, Universität München (1995).

[BRA95I] B. Bray, Private Communication (1995).

[BRA92] S. Brand: **Datenanalyse mit statistischen Methoden und Computerprogrammen,** Bilbliographisches Insititut Mannheim/Wien/Zürich (1992), 170.

[BRO95] S.J. Brodsky et al.: **Perturbative QCD Constraints on the Shape of Polarized Quark and Gluon Distributions,** Nucl. Phys. B441 (1995), 197.

[CAL69] C.G. Callan Jr. and D.J. Gross: **High-Energy Electroproduction and the Constitution of the Electric Current,** Phys. Rev. Lett. 22 (1969), 156.

[CIO93] C.Ciofi degle Atti et al.: **Nuclear Effects in deep inelastic scattering of polarized electrons off polarized ^{3}He and the neutron spin functions,** Phys. Rev. Vol 48 (1993), R968.

[COR92] F. Corriveau: **The Calculation of the Magnetic Field and Forces in the ZEUS Detector,** Desy Internal Note 92-084 (1992); Private Communication (1993).

[DOR89] M. Dell'Orso, L. Ristori: **VLSI Structures for Track Finding,** Nucl. Instr. and Meth. A278 (1989), 446.

[DOR90] M. Dell'Orso, L. Ristori: **A Highly Parallel Algorithm for Track Finding,** Nucl. Instr. and Meth. A287 (1990), 436.

[DUE95] M. Düren: **Das HERMES Experiment: From the Design to the First Results,** Habilitationsarbeit, Universität Erlangen-Nürnberg (1995).

[ELL74] J. Ellis and R.L. Jaffe: **A Sum Rule For Deep Inelastic Electroproduction From Polarized Protons,** Phys. Rev. D9 (1974), 1444; Erratum, Phys. Rev. D10 (1974) , 1669.

[ELL88] J. Ellis and M. Karliner: **An Analysis of the Angular Momentum of the Proton,** Phys. Lett. B213 (1988), 73.

[ELL94] J. Ellis: **The Spin Structure of the Proton,** QCD at HERA, Desy (1994).

[EMC89] EMC, J. Ashman et al.: **An Investigation Of The Spin Structure Of The Proton In Deep Inelastic Scattering Of Polarized Muons On Polarized Protons,** Nucl. Phys. B328 (1989), 1.

[EME95] J. Emerson: **Modelling of the HERMES Transition Radiation Detector,** Diplomathesis, Triumf (1995).

[FER95I] Manfred Ferstl, Private Communication (1995).

[GAU91] H.-G. Gaul: **Ein Polarimeter höchster Auflösung für thermische Wasserstoff- und Deuterium Atomstrahlen,** Doktorarbeit, Universität Heidelberg (1991).

[GRE95] O. Grebeniuk: **Error of the Vertex Determination,** Hermes Internal Note (1996).

[GRO90] R.H. Böck, H. Grothe, D. Notz and M. Regler: **Data analysis techniques for high-energy physics experiments,** Cambridge University Press (1990).

[GUT95] A. Gute: **Ein Drahtvermessungssystem für die Driftkammern des HERMES-Experiments,** Diplomarbeit, Universität Erlangen-Nürnberg (1995).

[GUT95I] A. Gute, Private Communication (1995).

[HMC] M. Düren et al.: **Das Hermes Monte-Carlo-Programm,** Hermes internal Note (1995).

[HAS95] D. Hash: **Bestimmung der Parameter einer 6-Ebenen Driftkammer für das HERMES-Experiment,** Diplomarbeit, DESY-IFH Zeuthen (1995).

[HOO89] P. Hoodbhoy, R.L. Jaffe and Aneesh Manohar: **Novel Effects in Deep Inelastic Scattering from Spin 1 Hadrons,** Nucl. Phys. B312(1989)571

[IHS95I] H. Ihssen, Private Communication (1995).

[JAF89a] R.L. Jaffe and Aneesh Manohar: **Deep Inelastic Scattering from Arbitrary Spin Targets,** Nucl. Phys. B321(1989)343

[JAF89b] R.L. Jaffe and Aneesh Manohar: **Nuclear Gluonometry,** Phys. Lett. B223 (1989)218

[OEL95] Ph. Oelwein: **Messung der longitudinalen Elektronenpolarisation beim Speicherring HERA und Monte-Carlo-Studien zur Kalibration des HERA-Elektronen-Polarimeters,** Diplomarbeit, MPI-Heidelberg (1995).

[KOR95] W. Korsch et al.: **Temperature Dependence of ^{3}He Polarization in the HERMES Internal Target,** Proc. of Int. Workshop on Polarized Beams and Polarized Gas Targets (1995).

[LAR94] S.A. Larin: **The Next-To-Leading QCD Approximation to the Ellis-Jaffe Sum Rule,** Phys. Lett. B334 (1994), 192-198.

[LEE93] K. Lee: **A Laser Optically Pumped Polarized He-3 Target For Storage Rings,** Nucl. Instr. Meth. A333 (1993), 294.

[MEI95] F. Meißner: **Monitor der Driftkammern im HERMES-Experiment,** Diplomarbeit, DESY-IFH Zeuthen (1995).

[MEZ94] Z.-E. Meziani: **Spin Structure of the Neutron (^{3}He) and the Björken Sum Rule,** SLAC-PUB-6433, Invited Talk presented at the 21st Annual SLAC Summer Institute, 26.7.–6.8.1993.

[NMC92] New Muon Collaboration: **Proton and Deuteron F_2 Structure Functions In Deep Inelastic Muon Scattering,** Phys. Lett. B295 (1992), 159.

[OUS94] J.K. Ousterhout: **Tcl and the Tk Toolkit,** Addison-Wesley Massachusetts (1994)

[PAV95I] P. Galumian, Private Communication (1995).

[PDG94] The Particle Data Group: **Review of Particle Properties,** Phys. Rev. D, Vol 50 (1994).

[POV94] B. Povh, K. Rith, Ch. Scholz, F. Zetsche: **Teilchen und Kerne: Eine Einführung in die physikalischen Konzepte,** Springer Verlag Berlin (1994).

[PTG94] Programming Techniques Group: ***ADAMO – Entity-Relationship Programming System, Version 3.3,*** ECP Division, CERN, Geneva (1994).

[ROE94] G. Röper: **Messung der Feldverteilung des Hermes Spektormetermagneten.,** Diplomarbeit, DESY (1994).

[SJO94] T. Sjostrand: **High-Energy Physics Event Generation With Pythia 5.7 And Jetset 7.4,** Computer Physics Commun. 82 (1994), 74.

[SLA93] SLAC E142 Collaboration, P.L. Anthony et al.: **Determination of the Neutron Spin Structure Function,** Phys. Rev. Lett. 71 (1993), 959.

[SLA95a] SLAC E143 Collaboration, K. Abe, et al.: **Precision Measurement of the Proton Spin Structure Function g_1^p,** Phys. Rev. Lett. 74 (1995), 346.

[SLA95b] SLAC E143 Collaboration, K. Abe, et al.: **Measurements Of The Proton And Deuteron Spin Structure Function g_2 And Asymmetry A_2,** Submitted to Phys. Rev..

[SMC93] SMC, B. Adeva et al.: **Measurement of the Spin Dependent Structure Function $g_1(x)$ of the Deuteron,** Phys. Lett. B302 (1993), 533.

[SMC94a] SMC, B. Adeva et al.: **Combined Analysis of World Data on Nucleon Spin Structure Functions,** Phys. Lett. B320 (1994), 400.

[SMC94b] SMC, D. Adams et al.: **Measurement of the Spin Dependent Structure Function $g_1(x)$ of the Proton,** Phys. Lett. B329 (1994), 399.

[SMC94c] SMC, D. Adams et al.: **Spin Asymmetry in Muon-Proton Deep Inelastic Scattering on a Transversely Polarized Target,** Phys. Lett. B336 (1994), 125.

[STE95] J. Stenger: **Entwicklung und Aufbau einer lasergepumpten Quelle für polarisierte Wasserstoff - und Deuteriumatomstrahlen,** Doktorarbeit, Universität Erlangen-Nürnberg (1995).

[STO78] J. Stoer, R. Bulirsch: **Einführung in die Numerik II,** Springer Verlag Berlin (1978).

[STO94] F. Stock et al.: **The Filtex / Hermes Polarized Hydrogen Atomic Beam Source,** Nucl. Instr. Meth. A343 (1994), 334.

[VEL91] M. Veltri et al.: **Polarized Quark Distributions from Semi-Inclusive Leptoproduction,** Proc. of Physics at HERA, DESY (1991), 447.

[WAN92] W. Wander: **Rekonstruktionstechniken für das Hermes Experiment,** Diplomarbeit, MPI-Heidelberg (1992).

[WAN95] W. Wander et al.: **DAD – Distributed Adamo Database system at Hermes,** Proc. of CHEP 95, Rio de Janeiro, 18.9.–22.9.1995.

[WHI90] L.W. Whitlow: **Deep Inelastic Structure Functions from Electron Scattering on Hydrogen, Deuterium and Iron at 0.6 GeV^2 $\leq$ $Q^2 \leq$ 30 GeV^2,** Ph.D. Thesis, SLAC (1990).

Acknowledgments

At the conclusion of my work in the HERMES software group I should not forget to thank all my colleagues and friends for their professional and personal support in this time. First I would of course like to thank Prof. Dr. Klaus Rith for his good supervision as well as the entire Erlangen group for it's pleasant atmosphere and fruitful discussions. Here I would like to mention Thomas Benisch, Manfred Ferstl, Carsten Großhauser, Andreas Gute, Matthias Kirsch, Jörn Stenger, Frank Neuenreither, Wolfgang-Andreas Lachnit, Tom Wölfel, our secretary Mrs. Löhner and of course Michael Düren. As the leader of the HERMES software and analysis group he was an ideal and always competent contact for technical and physics questions. In an amicable way he has taught me a lot over the course of my thesis work and he has shown or had to show considerable patience with me.

In Hamburg I would like to especially thank the former 'software office', Klaus Ackerstaff, Marc-André Funk, Holger Ihssen and Philipp Oelwein, for being good co-workers and for some other thing that do not fit into the framework of these acknowledgments. In all organizational questions our secretaries Sabine Krohn and Ramona Matthes were always quick to help. I owe the personell of the computing center a great deal, especially Patrick Fuhrmann and Karsten Künne, for their support in technical problems with our 28 CPUs. For their good cooperation and support in technical detector questions I would like to thank Yorck Holler, Kirsten Zapfe-Düren, Bernd Grabowski, Johan Blouw, Machiel Kolstein, Alexander Kisselev, Peter Green, Naomi Makins, Wolf-Dieter Nowak, Helmut Böttcher, Alexander Borissov, Joseph Emerson, Bruce Bray and Kevin McIlhany. I want to especially mention Pat Welch for many helpful hints and explanations.

I particularly would like to thank my wife, Astrid, for her love and her understanding for my extensive overtime over the entire time of my thesis work. My son Lars often missed his father or 'his' computer, when I was keeping it occupied. Thanks to both of you !